Title
Pulse Sequence Development for In Vivo Hyperpolarized 13C MRI

Author
Shang, Hong

Publication Date
2016

Peer reviewed|Thesis/dissertation

Pulse Sequence Development for In Vivo Hyperpolarized ^{13}C MRI

By

Hong Shang

DISSERTATION

Submitted in partial satisfaction of the requirements for the degree of

DOCTOR OF PHILOSOPHY

in

Bioengineering

in the

GRADUATE DIVISION

of the

UNIVERSITY OF CALIFORNIA, SAN FRANCISCO

AND

UNIVERSITY OF CALIFORNIA, BERKELEY

Acknowledgements

There are so many people to thank for helping me get my dissertation done. First I would like to thank my advisor, Dan Vigneron, with my deepest gratitude. Dan taught me how to conduct scientific research, how to explore innovative research direction, how to prioritize work, and how to initiate collaboration. Dan creates an excellent environment for conducting hyperpolarized ^{13}C research at UCSF, which helps everyone in this lab to learn fast and make progress. From Dan, I learn the importance of teamwork and making progress with cross-campus collaboration.

I would also like to thank Peder Larson for teaching me MRI pulse sequence. I am lucky to have this MRI pulse sequence expert always available for me, answering all my questions, providing comments on my new ideas, and sharing his innovative ideas with me. Peder set a good model for us for not only making huge progress in research, but also achieve a good work-life balance, as well as being very approachable and helping others with their projects too.

I also want thank Miki Lustig for being on my qual committee, providing advice for my dissertation work. Any time I talked to Miki, his passion on MRI encourages me. My knowledge of MRI basics was also learnt in Miki's MRI class.

I am also lucky to have the opportunity to work with John Pauly and Adam Kerr. I learn RF pulse design from John's class, one of the best classes I have ever taken. John and Adam are always very patient to listent to my research update and provide me very useful comments.

I would like to thank John Kurhanewicz, my qual exam committee chair and graduate advisor, for guiding me and making sure I am on the right track to make progress and graduate. I want to thank Michael Ohliger for inspiring new research ideas and sharing with his clinical perspective. Steve at UC Berkeley and Duan at UCSF did not advise my

dissertation research directly, but they did provide me some very useful guidance for PhD study in general, which is really appreciated.

All the students in the Surbeck lab/Berkeley are so awesome and make me have a really good time here, such as Zi, Eugene, Jeremy G, Jon, Jeremy B, Irene, Jessie, Dave, Frank, Wenwen, Shuyu, Peter, Henry, Yesu, Peng, Adam. You guys make me want to come back to visit the lab sometime soon. Good luck with everyone's research!

I want to give a special thanks to Galen and Cornelius. You guys are the first one coming to my mind when I encounter problems in the lab. You helped me out during my hard times. Your extensive support lead me to this stage.

Also special thanks for Subramaniam Sukumar and Robert Bok for helping me on the 14T pulse sequence project. I would never have been able to finish this project and my dissertation without Sukumar's help on sequence programming and Bob's help on animal experiments.

Many thanks are due to my awesome friends from the Bioengineering cohort, particularly Matt, Amy, Elaine, Jessie, Jesus, Monica, Tuan, Kesshi, Kevin, Julea, Preeya, Daniel, Paul, Arunan, and many more. You guys are the first group of people I know when I came to this new country. You guys let me know how to enjoy life as American does. I learn so many new hobbies from you guys, like climbing, frisbee, skiing, kayaking, camping, windsurfing. That somehow changes who I am. I miss you guys, and hope to see you again soon.

Most of all, I want to thank my parents. Without their support, I would never get the chance to come all the way here.

Abstract

Pulse Sequence Development for In Vivo Hyperpolarized ^{13}C MRI

by

Hong Shang

Doctor of Philosophy in Bioengineering

University of California, San Francisco

Hyperpolarized (HP) ^{13}C MRI with dissolution Dynamic Nuclear Polarization (DNP), with its sensitivity enhancements of >10,000 fold over thermal equilibrium values, enables non-invasive, spatially localized measurements of the enzymatic conversions of endogenous, nontoxic ^{13}C-labeled probes. Unique challenges faced in HP ^{13}C metabolic imaging include the non-recoverable nature of HP magnetization and the complex pattern of resonances that must be spectrally resolved. Rapid and efficient MRI pulse sequences are required to acquire data within the limited temporal window dictated by the rapid irreversible T_1 decay of HP magnetization. Previous HP ^{13}C MR sequences have been limited either by low spatial resolution or being able to image only one metabolically inactive compound. This work presents pulse sequence design for fast imaging of multiple HP ^{13}C metabolites with high spatiotemporal resolution based on balanced steady state free precession (bSSFP) sequence. One key feature of this new pulse sequence is a novel optimized short duration spectrally selective RF pulses with multiband profile specification, solved by convex optimization. A new method was proposed and tested to avoid bSSFP banding artifact by carefully choosing TR. Compared to previous methods, this new method is more insensitive to off-resonance and more SNR efficient with simple and robust reconstruction. Since image acquisition occurs in a transient state instead of steady state, a constant flip angle is unnecessary and usually leads to decaying signal with suboptimal SNR. In this work variable flip angle schemes were

designed for bSSFP transient state HP ^{13}C MRI to achieve a uniform signal profile, reduce image blurring and increase SNR. A new optimization approach was developed with improved off-resonance insensitivity. Finally, a hardware design project is presented to further increase image SNR by maintaining a sufficient field during sample transfer to preserve polarization.

Table of Contents

List of Figures

List of Tables

Chapter 1

Introduction

Magnetic resonance imaging (MRI) is a very powerful and widely used imaging modality due to its flexibility, non-radioactivity, and tunable imaging contrast especially for soft tissue. MRI has been used for a variety of clinical applications, including anatomical imaging, angiography, diffusion mapping, functional brain imaging, guided intervention, spectroscopic imaging, and many more. Besides, it is also widely applied in scientific research for drug development, uncovering the mysteries of disease, and also preclinical studies for fundamental biology research.

While MRI is routinely used in clinics, there is also extensive technical development going on to make MRI faster, achieve better image quality, or create new type of contrast enabling new applications. In this dissertation, I present technical developments for a new imaging contrast agent, hyperpolarized (HP) Carbon-13 (^{13}C). HP ^{13}C MRI with dissolution Dynamic Nuclear Polarization (DNP) is an emerging technique which has recently been shown to provide biologic information on previously inaccessible aspects of metabolic processes by detecting endogenous, nontoxic ^{13}C-labeled probes to monitor enzymatic conversions through key biochemical pathways.

Typically, MRI images are acquired based on ^{1}H signals from water or lipid molecules in the body. High signal-to-noise ratio (SNR) is achieved for ^{1}H MRI due to the high concentration of water molecules in vivo and high natural abundance of the ^{1}H isotope. ^{13}C MR suffers from low natural abundance and low concentration of key metabolites in

vivo, however, SNR can be dramatically improved with a technique called dissolution DNP. HP ^{13}C is distinguished by the capability to simultaneously image both injected agents and their downstream metabolic products separately, based on their unique chemical shifts, which provides unique metabolic information. HP ^{13}C MRI has been successfully applied in numerous preclinical studies, and a recent clinical trial in prostate cancer patients at UCSF showed safety and feasibility of this approach for investigating human disease.

The work presented in this dissertation focuses on HP ^{13}C pulse sequence development for improving image quality with higher SNR, higher spatial resolution, faster acquisition, and improved robustness against system imperfection. My dissertation includes four main contributions in Chapters 3-6, each of which is an adaptation of either an already published, peer-reviewed manuscript or one in the process of being reviewed.

In Chapter 3, I showed that RF pulses, a key component of HP ^{13}C MRI pulse sequence, can have improved performance by designing an optimized multiband RF pulse via convex optimization, such as with shorter duration, sharper transition, or lower peak B_1 amplitude. Selective RF pulses are commonly designed with the desired profile as a low pass filter frequency response. However, for HP ^{13}C MRI applications, the spectrum is sparse with signals existing at a few discrete resonant frequencies. By specifying a multiband profile and releasing the constraint on "don't-care" regions, the RF pulse performance can be improved. In this research, a framework for designing multiband RF pulses with improved performance was developed based on the Shinnar-Le Roux (SLR) algorithm and convex optimization. The advantage of this framework with a convex optimization approach is the flexible trade-off of different pulse characteristics. Designs for specialized selective RF pulses will be used for balanced steady state free precession (bSSFP) HP ^{13}C MRI, as described later.

Chapter 4 describes a new HP ^{13}C pulse sequence for combined perfusion and metabolic imaging with high spatiotemporal resolution, based on bSSFP sequences. bSSFP can provide superior SNR efficiency for HP ^{13}C MRI by efficiently utilizing the non-recoverable magnetization, but managing their spectral response is challenging in the context of metabolic

imaging. A new spectrally selective bSSFP sequence was developed for fast imaging of multiple HP ^{13}C metabolites with high spatiotemporal resolution. This novel approach for bSSFP spectral selectivity incorporates optimized short duration spectrally selective RF pulses within a bSSFP pulse train and a carefully chosen TR to avoid banding artifacts. The sequence enabled sub-second 3D dynamic spectrally selective imaging of ^{13}C metabolites of co-polarized [1-^{13}C]pyruvate and [^{13}C]urea at 2mm isotropic resolution, with excellent spectral selectivity (≈100:1). The sequence was successfully tested in phantom studies and in vivo studies with normal mice. This sequence is expected to benefit applications requiring dynamic volumetric imaging of metabolically active ^{13}C compounds at high spatiotemporal resolution including preclinical studies at high field and potentially clinical studies.

In the next studies, as described in Chapter 5, I further improved image performance for bSSFP based HP ^{13}C pulse sequence by varying flip angles within the pulse train. For HP ^{13}C MRI, since image acquisition occurs in a transient state instead of steady state, a constant flip angle is unnecessary and usually leads to decaying signal with suboptimal SNR. In this work variable flip angle schemes were designed for bSSFP transient state HP ^{13}C MRI to achieve a uniform signal profile, reduce image blurring and increase SNR. A new optimization approach was developed with improved off-resonance insensitivity. A second analytical approach was also developed as a simpler near-optimal alternative to the proposed optimization approach. Bloch simulations were used to study the signal evolution for off-resonance spins. HP phantom and animal experiments were performed to evaluate the new flip angle schemes compared to constant flip angles. Improved SNR ($\approx 40\%$), observation of small structures and reduced banding artifacts were achieved with this variable flip angle bSSFP sequence.

Finally, Chapter 6 describes a hardware approach for improving imaging SNR. Some ^{13}C substrates relax rapidly in low ambient magnetic fields. A hand-held electromagnet carrier was designed and constructed to preserve polarization by maintaining a sufficient field during sample transfer. The device was constructed with a solenoidal electromagnet,

powered by a non-magnetic battery, holding the HP sample during transfer. A specially designed switch automates deactivation of the field once transfer is complete. Phantom and rat experiments were performed to compare MR signal enhancement with or without the device for HP [^{13}C]urea and [1-^{13}C]pyruvate. The magnetic field generated by this device was tested to be > 50 Gauss over a 6 cm central section. In phantom and rat experiments, [^{13}C]urea transported via the device showed an SNR improvement by a factor of 1.8-1.9 over samples transferred through the background field.

Chapter 7 gives a summary and potential future applications are explored.

Chapter 2

Background

This chapter focuses on Magnetic Resonance Imaging (MRI) fundamentals that are necessary for understanding the pulse sequence developments in this dissertation project. In particular the background on RF pulse design and balanced Steady State Free Precession (bSSFP) pulse sequences are introduced for understanding the pulse sequence development described in Chapters 3-5. Detailed explanation of other aspects of MRI, such as image reconstruction and image processing, will not be given. Following the background on MRI, a brief introduction will be given on dynamic nuclear polarization.

2.1 Fundamentals of Magnetic Resonance Imaging

2.1.1 Spin, Magnetic Moment, Magnetization Vector, and Polarization

Although nuclear magnetic resonance (NMR) and spin dynamics are fundamentally quantum mechanical phenomena, the classical description can be used to describe the fundamentals of MRI/NMR underlying all the work presented in this dissertation.

Nuclei with an odd number of protons and/or an odd number of neutrons have nonzero spin, and the associated magnetic dipole moment μ.

$$\mu = \gamma S \tag{2.1}$$

where S is the spin angular momentum, and γ is gyromagnetic ratio, which is a known constant unique for different nuclear species.

At thermal equilibrium, spins are oriented randomly and the net magnetization is zero. However, in the presence of a static magnetic field, B_0, a magnetization moment $M = \sum \mu$ will be produced in the direction of the applied field. The total equilibrium magnetization is equal to the net difference between the nuclei aligned and anti-aligned with the applied field.

The potential energy of a magnetic moment in the static magnetic field is given by

$$E = -\mu \cdot B \tag{2.2}$$

The energy difference between the two populations is

$$\Delta E = h\frac{\gamma}{2\pi}B_0 \tag{2.3}$$

where h is Plancks constant, and B_0 is the static magnetic field strength.

Given certain temperature, T, the ratio of the two populations can be described by the Boltzmann distribution

$$\frac{N_-}{N_+} = e^{-\frac{\Delta E}{kT}} \tag{2.4}$$

where k is tbe Boltzmanns constant.

The polarization, P, is defined as

$$P = \frac{N_+ - N_-}{N_+ + N_-} = \frac{e^{\frac{\Delta E}{kT}} - 1}{e^{\frac{\Delta E}{kT}} + 1} \tag{2.5}$$

which describes the fraction of the spins aligned with the static magnetic field.

with a magnetic field of 3T and at body temperature (310K), the polarization of ^{1}H is $9.88 \cdot 10^{-6}$, while polarization of ^{13}C is even lower, $2.49 \cdot 10^{-6}$, meaning that out of a

million spins only a few more are parallel to the magnetic field than antiparallel. This small magnetization is the basis of detected signal in MRI. However, high signal-to-noise ratio (SNR) is achieved for ^{1}H due to the high concentration of water molecules in vivo and high natural abundance of the ^{1}H isotope. ^{13}C has neither of these advantages. However, SNR can be dramatically improved with a technique called dissolution dynamic nuclear polarization (DNP), which will be described in Section 2.4.

2.1.2 Bloch equation

The NMR signal arises from precession of the net magnetization, M, which is originally aligned with a main magnetic field, B. When M is tipped away from B, recession of M about B occurs. This precession is described by

$$\frac{dM}{dt} = M \times \gamma B \tag{2.6}$$

The solution is that M process around B at an angular frequecy of

$$\omega = \gamma B_0 \tag{2.7}$$

which is called the Larmor frequency. Section 2.2 will describe how M can be tipped away from B by a RF pulse.

2.1.3 Magnetic Resonance Imaging

Magnetic resonance imaging (MRI) is a method utilizing spatially-varying fields to produce location dependent Larmor frequency, thus enabling image spatial encoding. The encoding field is usually a magnetic gradient field with B_z varying linearly along certain direction.

$$B_z = B_0 + \vec{G} \cdot \vec{r} \tag{2.8}$$

The detected signal is

$$s(t) = e^{-i\omega_0 t} \int M(\vec{r}) e^{-t/T_2(\vec{r})} e^{-i\gamma \vec{G}\cdot\vec{r}}\, d^3\vec{r} \tag{2.9}$$

$$\vec{k}(t) = \frac{\gamma}{2\pi} \int_0^t \vec{G}(\tau)\, d\tau. \tag{2.10}$$

Neglecting relaxation, this equation becomes a Fourier transform. Therefore, by applying gradient we can sample the k space in certain trajectory. The image reconstruction can be simply a Fourier transform .

2.2 RF pulses

To detect the magnetization, an oscillating magnetic field, $B_1(t)$ at the Larmor resonant frequency is applied to the aligned nuclei by transmitting with Radio Frequency (RF) coils. Because the magnetic field frequency matches the nucleis resonant frequency, the nuclei absorb the energy, their magnetic moment changes direction, and they are excited. This results in a change in their net magnetization. Once this RF pulse has been applied, the nuclei begin precession.

In this excitation process, the magnetic moment of the nuclei is tipped away from the direction of the static field, into the plane perpendicular to the main magnetic field, thus causing precession around the axis of the external main field. The duration of the RF pulse at the Larmor frequency affects the angle between the axis of the static field and the net magnetization direction of the spins, called Flip Angle. This is the angle through which the magnetic moment precesses.

2.2.1 Small Flip Angle Pulses

For design of small-tip angle excitation pulses, the relation between RF pulse and excitation profile can be described by Fourier Transform.

$$M_{xy}(t) = i\gamma \int_0^t M_z(\tau) B_1(\tau) e^{i\Delta\omega\tau}\, d\tau. \tag{2.11}$$

This is the linearized version of the Bloch equation. Typically a rectangular function could be the desired shape for selective excitation pulse profile. In that case, the RF pulse waveform is simply the Fourier transform of rect function, which is a sinc function (with some truncation and window).

2.2.2 SLR Algorithm

The relation between RF pulse and excitation profile is nonlinear for large tip angle. The SLR algorithm is widely used to design RF pulse with estimated profile, which converts the pulse design to design of two polynomials, and eventually to a problem of FIR filter design.

RF pulse is designed by first creating two polynomial $B_N(z)$ and $A_N(z)$, and then apply inverse SLR transform on them. $A_N(z)$ is chosen to be consistent with $B_N(z)$ and to minimize power. So once $B_N(z)$ is determined, the RF pulse is determined.

For a RF pulse with selective excitation along x direction, specified by $\theta(x)$, the final rotation state is

$$\beta_N(x) = -i(n_x + in_y)\sin(\theta(x)/2)$$

Spectral selectivity is the same as spatial selectivity when there is no gradient.

The two polynomials are defined as

$$A_N(z) = z^{-N/2}\alpha_N$$

$$B_N(z) = z^{-N/2}\beta_N$$

where $z = e^{i\gamma Gxdt}$

It has magnitude constraint

$$|B_N(z)| = |\beta_N(x)| = \sin(\theta(x)/2)$$

$$|A_N(z)|^2 + |B_N(z)|^2 = |\alpha_N|^2 + |\beta_N|^2 = 1$$

Assuming the initial magnetization is along the longitudinal direction, the excited magnetization is

$$M_{xy} = 2\alpha^*\beta = 2A_N(z)^*B_N(z) \tag{2.12}$$

2.3 Balanced Steady State Free Precession (bSSFP) sequences

Balanced steady-state free precession (bSSFP) sequence is a popular fast imaging sequence with high SNR efficiency. The current development of gradient hardware offers the feasibility of fast switching gradient and short TR. Balanced SSFP is also known as TrueFISP, FIESTA and balanced FFE.

bSSFP sequence has also gained interest recently for HP ^{13}C MRI. This provides a very efficient way to use the non-recoverable HP signal. TR is usually much shorter (around 10ms), thus the total acquisition time is reduced and a high spatial resolution image can be achieved.

The name of bSSFP for HP imaging is confusing because the steady state cannot be achieved for HP signal due to irreversible decay of the hyperpolarization. Only the transient stage is used for HP ^{13}C imaging. bSSFP sequence features zero gradient-induced dephasing within each TR becasue of refocused phase encoding and balanced readout gradient, which

preserves transverse magnetization. The overall magnetization can be represented by a single magnetization vector that is not spatially dephased. Therefore, when studying signal evolution with bSSFP sequence, the gradient during each TR can be neglected.

During the free precession part between excitations(no B_1 field), the magnetization undergoes a precession by off-resonance frequency about the z-axis and also experiences both T_1 and T_2 relaxation. The off-resonance effects may be from field inhomogeneity, susceptibility artifact, chemical shift or unbalanced gradients.

$$\frac{d}{dt}\begin{pmatrix} M_x \\ M_y \\ M_z \end{pmatrix} = \begin{pmatrix} -1/T_2 & \gamma\triangle B_z & 0 \\ -\gamma\triangle B_z & -1/T_2 & 0 \\ 0 & 0 & -1/T_1 \end{pmatrix}\begin{pmatrix} M_x \\ M_y \\ M_z \end{pmatrix} = P\begin{pmatrix} M_x \\ M_y \\ M_z \end{pmatrix} \tag{2.13}$$

where $\gamma\triangle B_z = 2\pi\triangle f$, $\triangle f$ is the off-resonance frequency.

This is a continuous-time autonomous linear dynamical system with dimension n = 3

The solution can be derived by matrix exponential.

$$M(t+t_0) = e^{tP}M(t_0) \tag{2.14}$$

During the excitation by RF pulse with flip angle α and phase φ, the motion of the magnetization is simply a rotation based on the assumptions.

$$M(t_+) = R_z(-\varphi)R_x(\alpha)R_z(\varphi)M(t_-) \tag{2.15}$$

where $R_z(\varphi) = \begin{pmatrix} \cos\varphi & \sin\varphi & 0 \\ -\sin\varphi & \cos\varphi & 0 \\ 0 & 0 & 1 \end{pmatrix}$, $R_x(\alpha) = \begin{pmatrix} 1 & 0 & 0 \\ 0 & \cos\alpha & \sin\alpha \\ 0 & -\sin\alpha & \cos\alpha \end{pmatrix}$

Define M_k to represent the magnetization at echo time ($t = TE$) after the kth RF pulse.

$$M_{k+1} = e^{TE\cdot P}R_z(-\varphi)R_x(\alpha)R_z(\varphi)e^{TE\cdot P}M_k \tag{2.16}$$

For spin on-resonance, during the free precession part

$$\frac{d}{dt}\begin{pmatrix} M_x \\ M_y \\ M_z \end{pmatrix} = \begin{pmatrix} -1/T_2 & 0 & 0 \\ 0 & -1/T_2 & 0 \\ 0 & 0 & -1/T_1 \end{pmatrix} \begin{pmatrix} M_x \\ M_y \\ M_z \end{pmatrix} = P \begin{pmatrix} M_x \\ M_y \\ M_z \end{pmatrix}$$

$$M(t+t_0) = e^{tP} M(t_0) = \begin{pmatrix} e^{-t/T_2} & 0 & 0 \\ 0 & e^{-t/T_2} & 0 \\ 0 & 0 & e^{-t/T_1} \end{pmatrix} M(t_0) \tag{2.17}$$

If further assuming B_1 field align with x axis ($\varphi = 0$ *or* π)

$$\begin{aligned} M_{k+1} &= e^{TE\cdot P} R_x(\alpha) e^{TE\cdot P} M_k \\ &= \begin{pmatrix} e^{-TE/T_2} & 0 & 0 \\ 0 & e^{-TE/T_2} & 0 \\ 0 & 0 & e^{-TE/T_1} \end{pmatrix} \begin{pmatrix} 1 & 0 & 0 \\ 0 & \cos\alpha & \sin\alpha \\ 0 & -\sin\alpha & \cos\alpha \end{pmatrix} \begin{pmatrix} e^{-TE/T_2} & 0 & 0 \\ 0 & e^{-TE/T_2} & 0 \\ 0 & 0 & e^{-TE/T_1} \end{pmatrix} M_k \\ &= \begin{pmatrix} E_2 & 0 & 0 \\ 0 & E_2 & 0 \\ 0 & 0 & E_1 \end{pmatrix} \begin{pmatrix} 1 & 0 & 0 \\ 0 & \cos\alpha & \sin\alpha \\ 0 & -\sin\alpha & \cos\alpha \end{pmatrix} \begin{pmatrix} E_2 & 0 & 0 \\ 0 & E_2 & 0 \\ 0 & 0 & E_1 \end{pmatrix} M_k \\ &= \begin{pmatrix} E_2^2 & 0 & 0 \\ 0 & \cos\alpha \cdot E_2^2 & \sin\alpha \cdot E_1 E_2 \\ 0 & -\sin\alpha \cdot E_1 E_2 & \cos\alpha \cdot E_1^2 \end{pmatrix} M_k \end{aligned}$$

where $E_2 = e^{-TE/T_2}$, $E_1 = e^{-TE/T_1}$,

2.4 Nuclear Polarization

Electronic polarization is a factor of 100 times greater than that of ^{13}C around 1 K. If using an oscillating field at the appropriate frequency, the polarization can be transferred from electron to ^{13}C, which is called dynamic nuclear polarization. The Overhauser effect (OE) was first performed in metals but can be performed in liquids as well. The OE is maximized when the irradiation frequency ω equals ω_e, the EPR resonance frequency. The solid effect (SE) occurs with isolated, non-interacting paramagnetic centers when the anisotropic part of the electron-nuclear interaction Hamiltonian ($\langle H_{aniso} \rangle$) is non-zero averaged over time. The maximal enhancement is achieved when $\omega = \omega_e \pm \omega_n$, where ω_n is the nuclear Larmor frequency.

In dissolution DNP, the polarized sample is rapidly dissolved to liquid state and heated to room temperature while retaining solid state polarization. For certain ^{13}C labeled probe, that the liquid state T_1 relaxation is sufficiently slow, the persistent polarization has opened the door to the use of polarized spins as in vivo contrast agents.

Chapter 3

Multiband RF Pulses with Improved Performance via Convex Optimization

3.1 Abstract

Selective RF pulses are commonly designed with the desired profile as a low pass filter frequency response. However, for many MRI and NMR applications, the spectrum is sparse with signals existing at a few discrete resonant frequencies. By specifying a multiband profile and releasing the constraint on "don't-care" regions, the RF pulse performance can be improved to enable a shorter duration, sharper transition, or lower peak B_1 amplitude. In this project, a framework for designing multiband RF pulses with improved performance was developed based on the Shinnar-Le Roux (SLR) algorithm and convex optimization. It can create several types of RF pulses with multiband magnitude profiles, arbitrary phase profiles and generalized flip angles. The advantage of this framework with a convex optimization approach is the flexible trade-off of different pulse characteristics. Designs for specialized selective RF pulses for balanced SSFP hyperpolarized (HP) ^{13}C MRI, a dualband saturation RF pulse for ^{1}H MR spectroscopy, and a pre-saturation pulse for HP ^{13}C study were developed and tested.

3.2 Introduction

Multiband RF pulse designs have been previously used in hyperpolarized (HP) ^{13}C MRI to yield different flip angles to substrates and metabolites [Schricker *et al.*, 2001; Larson *et al.*, 2008; Kerr *et al.*, 2008]. Combining multiband RF pulses with spectroscopic imaging readouts has been demonstrated successfully for improved observation of metabolic activity with higher SNR and slower signal decay [Larson *et al.*, 2008]. In HP ^{13}C MRI, the signal arises only from injected substrate and its metabolites. For many other applications in MRI and NMR, the spectrum is sparse as well. For example in ^{1}H MRI, the spectrum is dominated by water and lipid resonant peaks. The RF pulse profile is important only for frequencies where there are signals and thus there is substantial flexibility in terms of pulse design when there is sparsity in the spectral domain. Commonly, selective RF pulses are designed with profiles similar to a low-pass filter frequency response. In other words, the stopband and don't-care region are treated equally.

In this work, we introduce a multiband RF pulse design framework with the goal of optimizing pulse performance and enabling broader applications. It only specifies the desired profile around the specific resonance frequency of each compound, and releases the unnecessary constraints of don't-care regions. Pulse performance can be improved with this lesser constraint thus enabling shorter pulse duration, sharper profile transition, or lower peak B_1 amplitude.

RF pulse design is commonly performed with the Shinnar-Le Roux (SLR) algorithm [Pauly *et al.*, 1991] which addresses the nonlinearity of the Bloch equation at higher flip angles. The SLR algorithm reversibly transforms the RF pulse design problem to a finite impulse response (FIR) filter design problem that is well established and for which many methods exist. The SLR algorithm has been applied for designing single-band pulses with linear-phase or minimum-phase [Pauly *et al.*, 1991], for applications which require a spatially excited multiband profile [Cunningham and Wood, 1999], and for other non-linear

phase profiles such as quadratic phase pulse [Le Roux *et al.*, 1998; Schulte *et al.*, 2004]. In this work, the SLR algorithm has been further extended to pulse design with multiband magnitude profiles, arbitrary phase profiles, and generalized flip angles. Note that some common assumptions in SLR algorithm are inherited here, such as ignoring relaxation during RF pulse, which is a reasonable approximation for applications where RF pulse duration is much shorter than T_1 and T_2 including the hyperpolarized [1-^{13}C] pyruvate and ^{13}C-urea experiments conducted in this study.

Three different pulses were designed: (1) RF pulse with shorter duration for spectrally selective balanced Steady State Free Precession (bSSFP) sequence, (2) dual-band saturation pulse with sharper transition for ^{1}H MRS and (3) saturation pulse with significantly reduced stopband ripple for HP ^{13}C pre-saturation sequence. Bloch simulations were used to assess all of the pulses, and the first two pulses were further evaluated with phantom imaging experiments.

3.3 Methods

3.3.1 Pulse Design

The SLR algorithm casts the RF pulse design to a FIR filter design problem. Design of a multiband RF pulse has no additional difficulties for the inverse SLR transform itself; instead, it requires a more sophisticated FIR filter design as the beta polynomial. In this work, we further release the constraint on the phase profile to improve design flexibility. A RF pulse generating excitation profile with linear phase can be refocused. Non-linear phase pulse profiles, including minimum-phase, maximum-phase [Pauly *et al.*, 1991], and quadratic-phase [Schulte *et al.*, 2004], cannot be fully refocused. However, it is not a concern for applications such as saturation pulses, inversion pulses, spectrally selective ^{13}C excitation pulses, and slab-selective pulses in 3D imaging.

RF pulse design in general is not necessarily a convex problem, and a global optimal solution may not be found. However, if the SLR algorithm assumptions can be met, the RF pulse design is a convex problem. The beta polynomial with a multiband magnitude frequency response and an arbitrary phase frequency response can be designed and optimized using spectral factorization within the convex optimization framework [Kerr *et al.*, 2008; Wu *et al.*, 1996], followed by inverse SLR transform to achieve a RF pulse with optimized performance. The formulation of complex-coefficient filter design as a convex optimization problem is shown below, while the explanation of notation and more details can be found in Appendix A.

$$
\begin{array}{lll}
\textit{minimize} & y(1) + \lambda \cdot \delta_1 & \\
\textit{variable} & y \in R^{(2N-1)*1},\ \delta_1 \in R & \\
\textit{subject to} & B_{\omega_i}^T y \geq \epsilon & -\pi \leq \omega_i \leq \pi \\
& B_{\omega_i}^T y \leq 1 - \epsilon_2 & -\pi \leq \omega_i \leq \pi \\
& (L(e^{j\omega_i}))^2 \leq B_{\omega_i}^T y \leq (U(e^{j\omega_i}))^2 & -\pi \leq \omega_i \leq \pi \\
& B_{\omega_i}^T y \leq \delta_1 & \omega_i \in \Omega_{stopband} \subseteq [-\pi, \pi] \\
& ||Fy||_2 \leq \delta_2. &
\end{array}
\tag{3.1}
$$

To solve this problem we used CVX, a package for specifying and solving convex optimization [Grant *et al.*, 2008]. In the spirit of reproducible research and open-source research tools, we are providing the open source code, which can be downloaded from https://github.com/shanghong/Multiband-RF-pulse-Design.git

The design procedure is illustrated in Figure 3.1. We first specify the desired multiband excitation which includes the center frequency, bandwidth and flip angle for each band, all of which depend on the specific application and MR spectrum. Other parameters, including pulse duration, total energy, peak amplitude, profile ripple, and transition bandwidth can either be specified or left to be optimized. Then the specification of the RF pulse profile is converted to the specification of the beta polynomial, which is designed and optimized via

convex optimization. Lastly the RF pulse is created by inverse SLR transform.

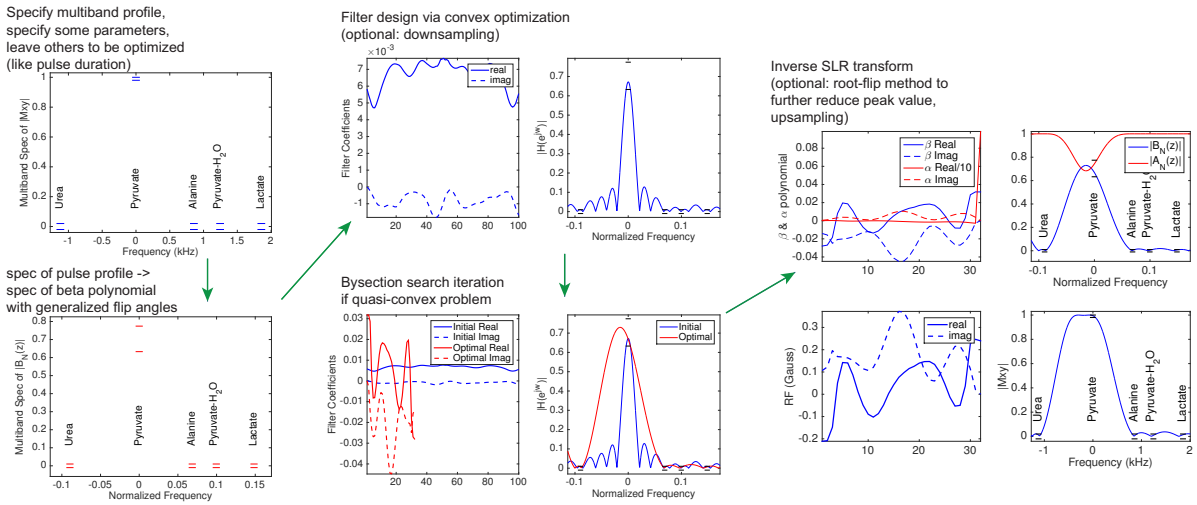

Figure 3.1: Diagram of the design procedure. The example is of a pulse design for application 1, to design a multiband RF pulse with shortest duration used in bSSFP sequence.

Compared to previous studies [Larson *et al.*, 2008; Kerr *et al.*, 2008], this work features a flexible trade-off among multiple RF pulse characteristics, such as pulse duration, peak amplitude, total energy, profile transition bandwidth, and profile ripple. The advantage of the convex optimization approach is to incorporate additional design criteria as long as they are also convex, such as total energy, peak amplitude, stopband ripple. Some characteristics are quasi-convex, such as transition bandwidth and pulse duration, which can be optimized by bisection search. Each iteration of the bisection search involves solving a convex optimization feasibility problem. Further details of incorporating convex constraints are in Appendix A.

To generalize this design framework for broad applicability, arbitrary flip angles were allowed to be specified for each band. Pauly et al. [Pauly *et al.*, 1991] derived the parameter relations for 5 types of pulses: small-tip-angle pulse, 90° excitation pulse, 180° inversion pulse, 180° crushed spin-echo pulse, and 90° saturation pulse. With arbitrary flip angles, the parameter relations need to be generalized, especially determining the relationship between

the beta polynomial FT ripple amplitudes and the pulse profile ripple amplitudes. Such SLR parameter relations with generalized flip angles have been studied before, however, previous work [Raddi and Klose, 1998] is limited in that the effect of ripple in the alpha polynomial FT is neglected, and the transverse and longitudinal magnetization ripples are mixed together, while only one is of concern for most applications. Another study [Lee, 2007] used numerical inversion followed by an iterative refinement which makes the pulse design cumbersome and computationally intensive. In this work, a new general parameter relation of the SLR algorithm is derived. It first calculates the range of flip angle given the range of magnetization (specified by the ripple), then figures out the range of beta polynomial FT based on flip angle. More details are given in Appendix B. This method is accurate, easy to calculate, and intuitive. Note that this method only achieves accurate profile amplitude ripple when B_1 field is calibrated correctly. In practice B_1 field is usually non-uniform, and pulse profile amplitude errors may be sensitive to B_1 deviation, which is a common problem for SLR pulse design, and will be discussed in more detail in the Results section.

3.3.2 Application 1: Selective RF pulses in balanced SSFP

When using a selective RF pulse in a bSSFP sequence, minimum RF pulse duration is desired to reduce TR, minimize banding artifacts, and reduce total scan time. The goal is to design selective RF pulses with the minimum duration for a HP ^{13}C bSSFP sequence at 14T to image ^{13}C-labeled pyruvate, lactate, and urea individually. HP ^{13}C MRI with dissolution Dynamic Nuclear Polarization (DNP) has been shown to provide metabolic information in vivo by detecting endogenous, nontoxic ^{13}C-labeled probes [Ardenkjær-Larsen *et al.*, 2003; Golman *et al.*, 2006; Nelson *et al.*, 2013]. Spectrally selective bSSFP sequences for multiple compound HP ^{13}C metabolic mapping have been developed with non-selective RF pulse [von Morze *et al.*, 2013; Månsson *et al.*, 2012; Leupold *et al.*, 2009]. However, it has numerous problems, such as narrow passband and suboptimal SNR. Integrating a selective RF pulse

can contribute to the overall spectral selectivity and allow optimizing other performance.

For the HP ^{13}C studies with copolarized [1-^{13}C]pyruvate and [^{13}C]urea as the injected substrate, the spectrum is sparse including resonance peaks of pyruvate, pyruvate hydrate, urea, and metabolic products (considering lactate and alanine in this case, bicarbonate is neglected). A multiband profile is specified for exciting one compound (flip angle = 60°) while not exciting others and releasing unnecessary constraints elsewhere, which is the key for minimizing pulse duration. The frequency range of each band is specified based on the experimental setup, especially the shimming capability (50Hz in this work). Excitation magnetization ripple was specified as 0.01 for the passband and 0.005 for the stopband. A standard minimum-phase SLR pulse and a linear-phase multiband pulse were also designed as comparison.

3.3.3 Application 2: Dualband saturation RF pulse

For some applications of ^{1}H MR spectroscopy (MRS), suppression of two or more compounds is desired. As a proof-of-concept, a saturation pulse was designed to suppress water (90°) and perform metabolite editing by suppressing glutamine/glutamate/NAA (120°) without perturbing peaks in between for 3T ^{1}H MRS. Saturation pulses with flip angles larger than 90° are often used to offset rapid T_1-dependent signal recovery [Tran *et al.*, 2000]. In this work, the flip angle was chosen arbitrarily as a feasibility demonstration. The goal was to design a dualband saturation pulse with the sharpest transition to minimize suppression of useful compounds, with other parameters fixed, including duration = 26ms, and in-slice / out-of-slice ripple = 0.05 / 0.001.

3.3.4 Application 3: Small ripple saturation RF pulse

A spectrally selective pre-saturation pulse sequence has been developed to suppress unwanted resonance in HP ^{13}C studies during the bolus infusion [von Morze *et al.*, 2016]. The sat-

uration pulse was repeated multiple times throughout the infusion to compensate for B_1 inhomogeneity and flow of ^{13}C-labeled agent. Therefore, the out-of-slice ripple needs to be very small to minimize the accumulated effect of perturbing desired HP signal. A saturation RF pulse with reduced out-of-slice ripple was designed within this new framework by releasing the constraint on the saturation profile at frequencies outside of the band around the desired resonance peak.

3.3.5 MR experiments

For the selective RF pulse in bSSFP (application 1), phantom tests were performed on a 14T vertical NMR system (Varian Inc, Palo Alto, CA). The excitation profile was measured by shifting the center frequency and measuring signal amplitude for a ^{13}C enriched urea phantom. Three RF pulses were used in a custom 3D bSSFP sequence for sequential acquisition of urea, lactate, and pyruvate images. The minimum duration of the lactate-only pulse is longer than the other two. To simplify the implementation, we set the lactate-only pulse duration for all three pulses. BSSFP sequence parameters included: FOV = 64x32x32mm; matrix size = 32x16x16; TR = 4ms; TE = 2ms; scan time = 1s/image; flip angle = 60°; readout bandwidth = 21 kHz. A HP phantom test was performed with HP [1-^{13}C]pyruvate syringe and HP [^{13}C]urea syringe separately.

For the dualband saturation pulse (application 2), experiments with a water syringe were performed on a 3T clinical MRI scanner (GE Healthcare, Waukesha, WI, USA) using a shimming gradient (0.04 G/cm) to create off-resonance along one spatial dimension. The saturation pulse was applied followed immediately by a 1D gradient echo sequence (with phase encoding turned off), to get the 1D spatial profile, which mimics the spectral profile. The water syringe, shimming gradient and readout gradient were all along z direction. Parameters include FOV = 12cm, resolution = 0.6mm, TE = 4ms, readout bandwidth = 50kHz. A windowed sinc excitation RF pulse was used (without slice selective gradient),

with duration = 0.8ms, Time-Bandwidth-Product = 4, flip angle = 90° to uniformly excite within [-1000 1000]Hz. The saturation pulse is very sensitive to B_1 transmit gain calibration, which was first calibrated automatically, then manually fine tuned.

3.4 Results

3.4.1 Application 1: RF pulses for balanced SSFP

Three RF pulses were designed for exciting urea, lactate, and pyruvate, respectively. The lactate-only pulse is shown in Figure 3.2(A) as an example, with the Bloch simulation of the excitation profile shown in Figure 3.2(B, D). The pulse duration is listed in Table 3.1, and compared to a standard single-band minimum-phase SLR pulse design, as shown in Figure 3.2(C). With this new optimized RF pulse, the total scan time of our 3D bSSFP acquisition with 2mm isotropic resolution is reduced by at least 430ms to be within 1s, to enable real-time within-breath preclinical imaging.

Table 3.1: For selective RF pulse used in bSSFP ^{13}C sequence at 14T, comparing pulse duration of optimal multiband design to standard minimum-phase SLR pulse design.

RF pulse	multiband pulse duration (ms)	minimum-phase pulse duration (ms)	Duration reduction
lactate-only	2.32	4.00	42 %
pyruvate-only	1.72	3.10	45%
urea-only	1.16	1.85	37%

Another feature of these pulses is the arbitrary phase profile. To illustrate the improvement by releasing the linear phase constraint, the Bloch simulation was carried out to compare multiband arbitrary-phase pulses and multiband linear-phase pulses. One example of a urea-only pulse is shown in Figure 3.3. To achieve similar multiband profile and similar pulse duration, the arbitrary-phase pulse has significantly reduced peak amplitude and pulse power.

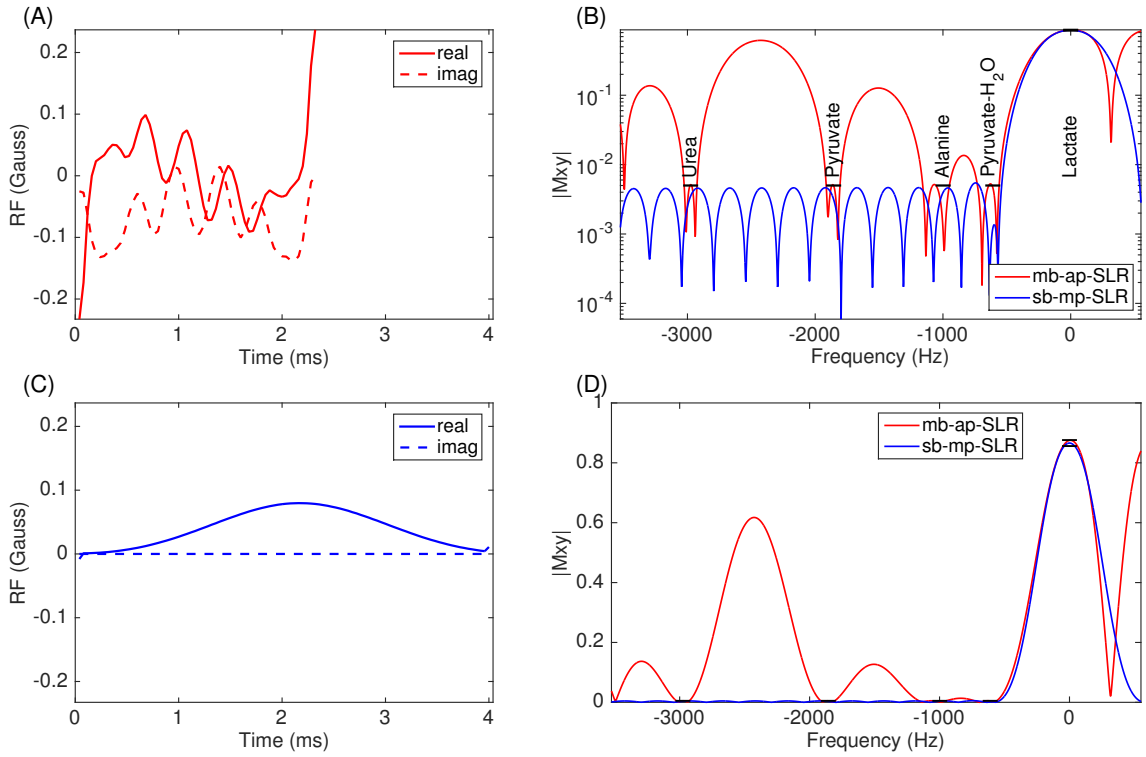

Figure 3.2: (A) Multiband arbitrary-phase lactate-only RF pulse (mb-ap-SLR) for bSSFP ^{13}C sequence at 14T with shortest duration is compared to a standard single-band minimum-phase SLR pulse (sb-mp-SLR) (C). For both pulses, Bloch simulations are shown for the magnitude excitation profile in logarithmic scale (B), and linear scale (D). The specification of multiband profile is highlighted in black in (B).

The measured excitation profile matched closely with simulation and design specifications. One example of a pyruvate-only pulse is shown in Figure 3.4(A). Using these RF pulses in the bSSFP sequence resulted in good selectivity with HP phantom test, as shown in Figure 3.4(B,C). More specifically, with the HP ^{13}C urea phantom, the bSSFP acquisition selecting lactate/pyruvate demonstrated a contaminant signal less than 3.7% / 6.1% of actual signal in the urea acquisition. With the HP ^{13}C pyruvate phantom, the bSSFP acquisition selecting lactate/urea showed a contaminant signal less than 4.9% / 2.8% of actual signal in the pyruvate acquisition.

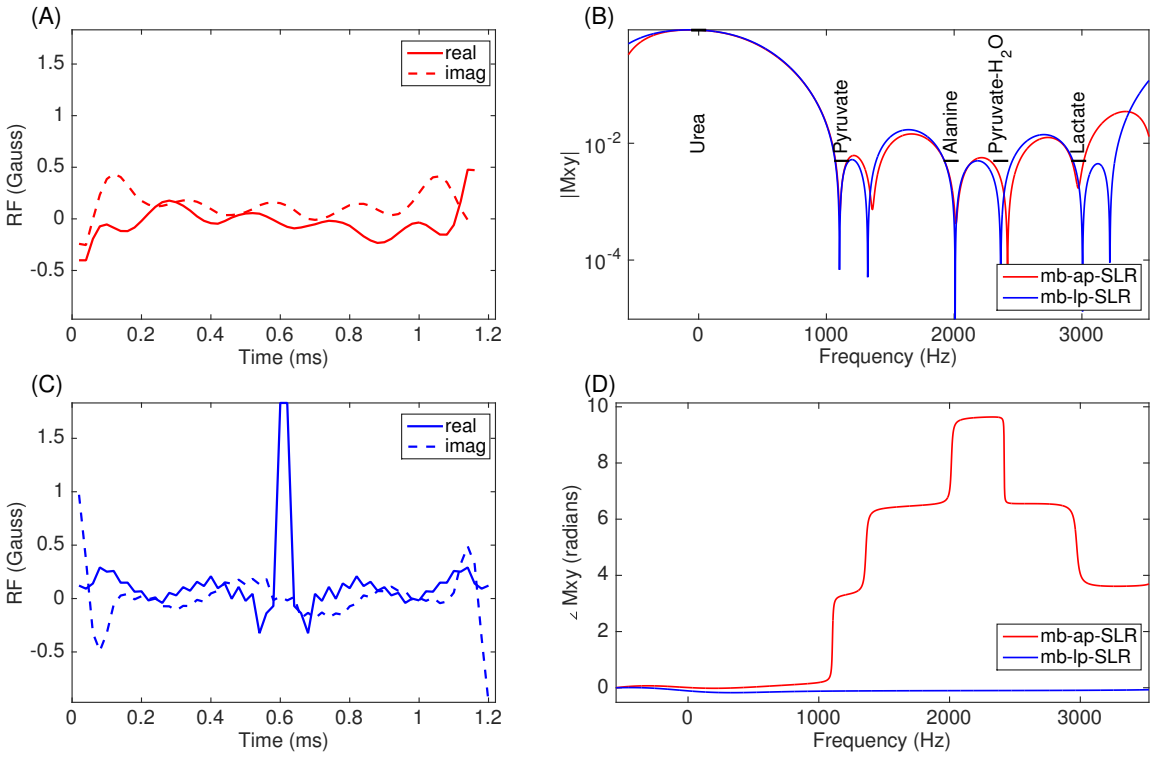

Figure 3.3: (A) A multiband arbitrary-phase urea-only RF pulse (mb-ap-SLR) for bSSFP ^{13}C sequence at 14 T with shortest duration, is compared to a multiband linear-phase SLR pulse (mb-lp-SLR) (C). For both pulses, Bloch simulations are shown for the magnitude excitation profile (B) and the phase profile adjusted for the linear phase component (D). The specification of the multiband profile is highlighted in black in (B). The arbitrary-phase pulse has peak B_1 value of 0.477 G (510 Hz), while the linear-phase pulse has peak B_1 value of 1.831 G (1961 Hz).

BSSFP RF pulses with minimum duration usually have higher peak amplitude. For example the optimal lactate-only pulse has peak amplitude of 0.237 Gauss (253.5 Hz), 3.0-fold higher compared to a standard minimum-phase SLR pulse. Also note that the first and last samples have the highest amplitudes. This peak amplitude is still within the MR system limits in our experimental setup, however, it could be a concern for other systems. One advantage of this RF pulse design framework is allowing an easy trade-off of pulse duration and peak amplitude by setting appropriate constraints on the end-spike as illustrated in Appendix A. As a demonstration, 3 RF pulses were designed with different constraints

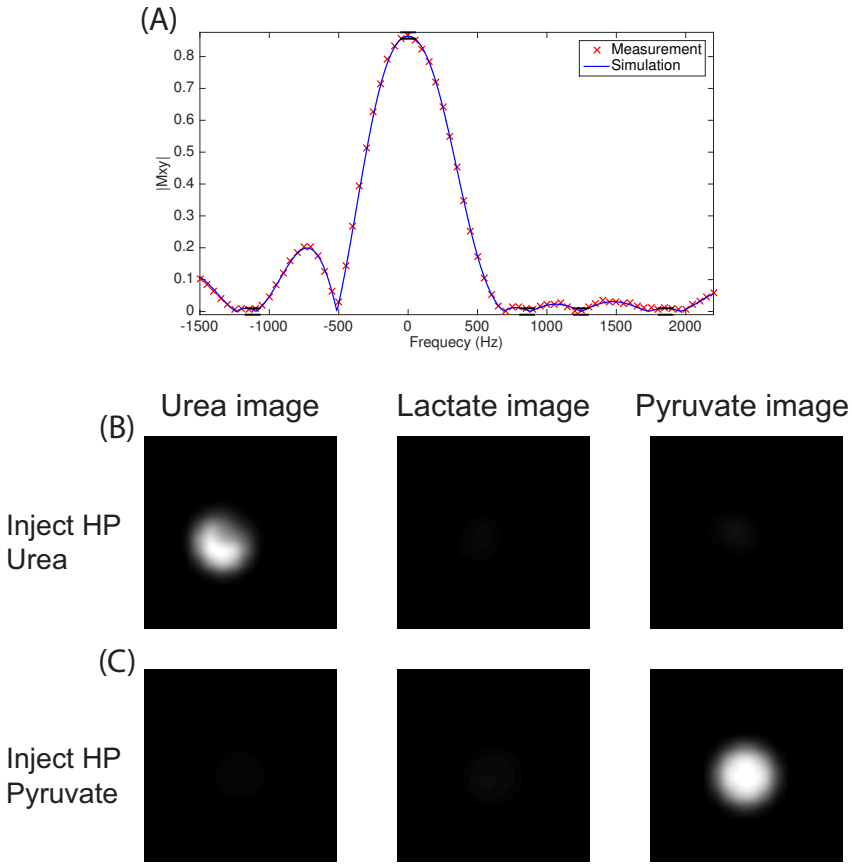

Figure 3.4: (A) Simulated and measured excitation profile of the pyruvate-only pulse plotted with the profile specifications (black lines). For the 3D bSSFP imaging with selective RF pulses on HP ^{13}C phantom at 14T, urea / lactate / pyruvate images are shown after injecting HP urea (B). The same sequence but injecting HP pyruvate are shown in C. One central axial slice of the 3D images is displayed in B and C.

on end-spike, which resulted in significantly reduced peak amplitude and slightly longer pulse duration, as shown in Figure 3.5. The limitation of this method for controlling peak amplitude is that it may not work for RF pulse designs with large time-bandwidth-products, where the peak amplitude may not be at the first or last sample.

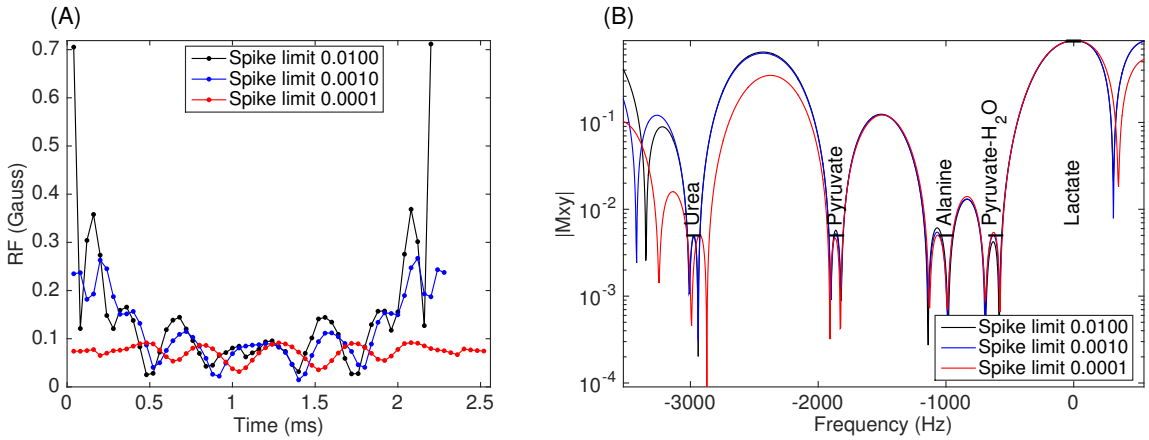

Figure 3.5: bSSFP lactate-only RF pulse design with different end-spike (peak amplitude) constraint (A), and the corresponding simulated profiles (B).

3.4.2 Application 2: Dualband saturation RF pulse

A dualband saturation RF pulse for ^{1}H MRS at 3T was designed with input specification shown in Figure 3.6(B). The resultant pulse (Figure 3.6(A)) has a pulse profile (Figure 3.6(B)) as determined with Bloch simulation. Zoomed-in regions for the response in each of the input specified bands are shown in Figure 3.6(D-F). The simulated profile meets the design specification exactly. Note that the profile of the band with 120° flip angle (Figure 3.6(D)) also meets the design specification accurately, which demonstrates the proposed SLR parameter relation with generalized flip angles, as illustrated in Appendix B. If simply using the parameter relation for 90° saturation pulse [Pauly *et al.*, 1991], the resulting profile will have a large deviation from the design specification.

The transition bandwidth of this pulse is 44 Hz. For comparison in terms of transition bandwidth, an alternative approach was implemented to design two single-band minimum-phase beta polynomials individually, then sum them and apply inverse SLR transforms to generate a dualband saturation RF pulse. This simpler approach results in a pulse with a transition of 62Hz, 41% larger than the optimal pulse. Measured saturation profile matches well with simulation and design specifications as shown in Figure 3.6(C). The measured

profile has some distortion for off-center spins due to the non-linearity of the shimming gradient.

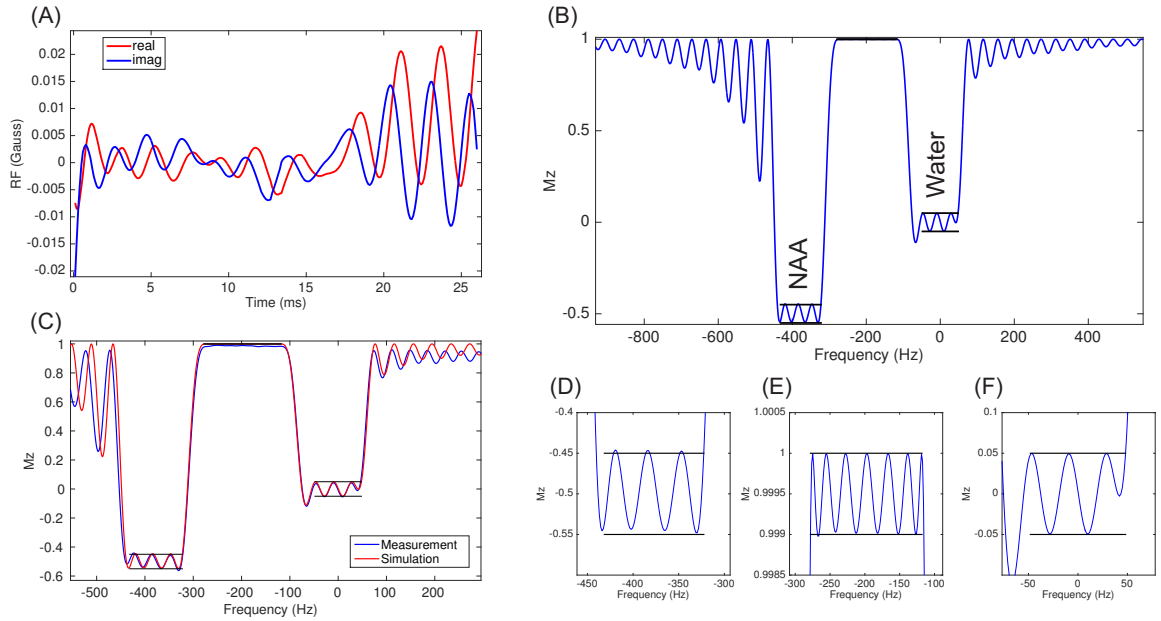

Figure 3.6: Dualband saturation pulse for suppression of both water (90°) and glutamine/glutamate/NAA (120°) for ^{1}H MRS at 3T. Pulse waveform (A). Bloch simulation of the saturation profile (B), with the predefined specification highlighted in black. Zoomed in plots of each band (D, E, F). The measured profile agrees well with the simulated result (C).

3.4.3 Application 3: Small ripple saturation RF pulse

The saturation pulse with reduced stopband ripple for suppression of undesired resonances in HP ^{13}C-lactate studies was designed and shown in Figure 3.7(A). The Bloch simulation of the pulse profile is shown in Figure 3.7(B, D), together with the specified bands. A standard maximum-phase SLR pulse was used for comparison, as shown in Figure 3.7(C). The standard SLR pulse meets the design spec of 0.001 stopband ripple, while the improved design has 10^{-6} stopband ripple, which is 3 orders of magnitude smaller. The 0.001 stopband ripple is adequately low for one single pulse performance, however it may still cause signal loss when the saturation pulse is repeated multiple times. If the RF pulse is repeated 32

times as a pre-saturation pulse, the standard maximum phase pulse will cause 3.151% loss of desired HP lactate signal, while the optimal pulse will only cause 0.003% loss.

Bloch simulation was also carried out with a non-ideal B_1 calibration (scaled RF pulse). As shown in Figure 3.8(A, B), the saturation profile is sensitive to B_1 field, especially for passband. This is also why this saturation pulse was repeated multiple times to compensate for B_1 sensitivity. The stopband ripple is still very low given the range of B_1 field. Also note that such B_1 sensitivity is a common problem for all SLR pulse design, as shown in Figure 3.8(C, D).

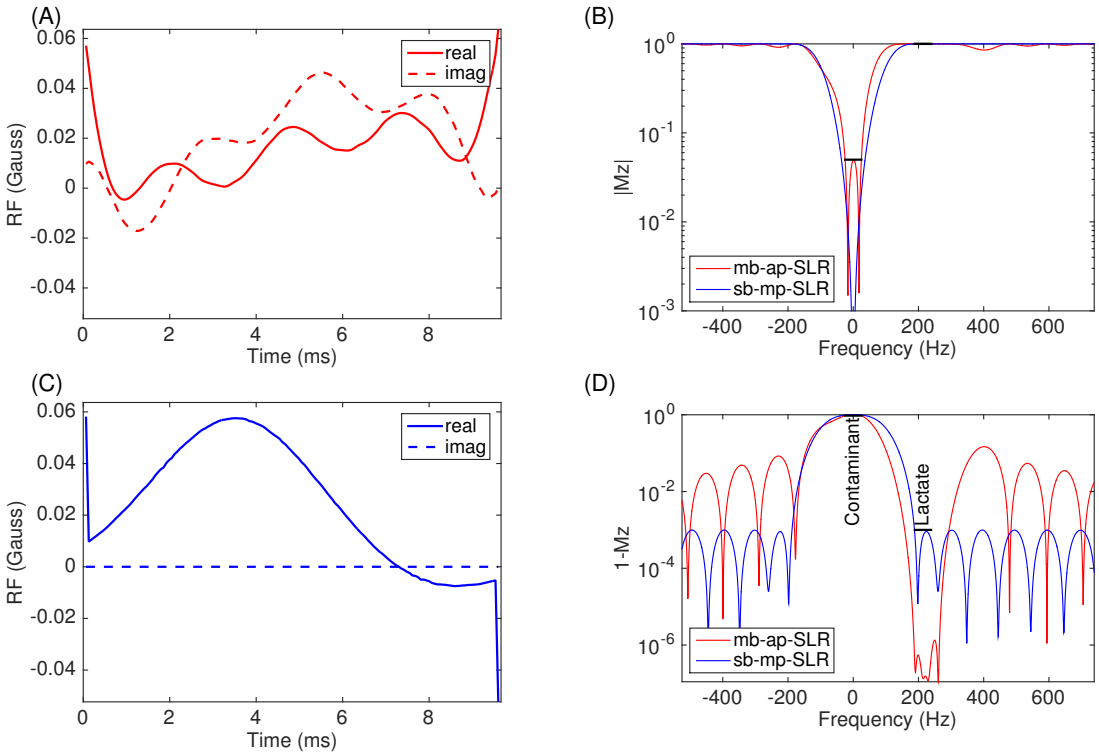

Figure 3.7: (A) Saturation RF pulse with extremely low stopband ripple (mb-ap-SLR) used in HP ^{13}C Lactate study with repetitive pre-saturation pulse, was compared to a standard maximum-phase SLR pulse (sb-mp-SLR) (C). For both pulses, Bloch simulations of the saturation profile are shown for passband (B) and stopband (D). The specification of the multiband profile is highlighted in black in (B, D).

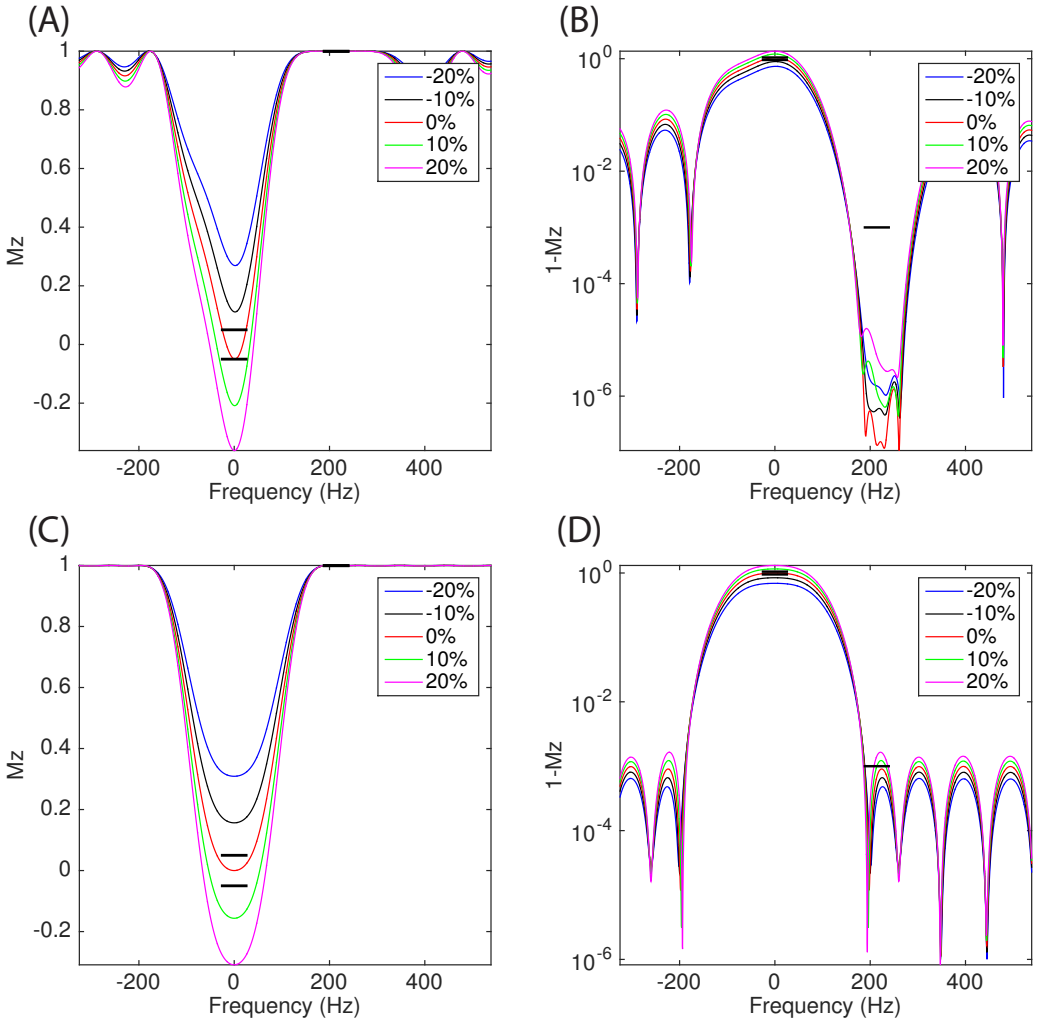

Figure 3.8: Bloch simulation of ^{13}C saturation RF pulse profile with non-ideal B_1 transmit field calibration. Each profile corresponds to a scaled RF pulse. The profile of optimized pulse with reduced stopband ripple is shown in (A, B), while the maximum-phase SLR pulse profile is shown in (C, D). The passband is visualized in (A, C) with linear scale while the stopband is visualized in (B, D) with log scale. The specification of the multiband profile is highlighted in black.

3.5 Discussion

In this work, we show that RF pulse performance can be improved beyond the limits of previous SLR pulse design methods [Pauly *et al.*, 1991] by exploiting the sparsity of spectrum and specifying a multiband profile. There is no longer an analytical relation for trade-off of

pulse performance as in [Pauly *et al.*, 1991] , but it still allows an easy trade-off of different characteristics via the convex optimization approach. Tighter constraints on one parameter will usually sacrifice other performance metrics.

One advantage of this framework is that minimal work is required of the pulse designer. The pulse designer only needs to specify which parameter should be optimized and this design framework will figure out the optimal solution automatically. By comparison, the conventional pulse design may need multiple iterations to fine tune some parameters to meet the design specifications. For example, in application 3, we specified to optimize the stopband ripple of the saturation pulse, and this framework created a pulse with global optimal solution in terms of stopband ripple. Previous SLR pulse design methods necessitated an explicit declaration of the value of stopband ripple. This value may need to be fine tuned manually multiple times to obtain a reasonably good result, but this does not guarantee we have found the global optimal solution. Although this framework using convex optimization requires longer computation time, we have found that the total time spent on pulse design is actually shorter compared to conventional approaches that manually iterate parameters.

A practical consideration is how many samples to use for the RF pulse and FIR filter design. The SLR algorithm assumes each hard subpulse is small (flip angle by each sample in the RF pulse), so the sampling rate of the RF pulse needs to be adequately large. But solving convex optimization problem with large number of filter coefficients may take too much time. In this work we solved this problem by designing the FIR filter after downsampling the design specifications. Once an optimal FIR filter is designed, we apply upsampling before the inverse SLR transform. Thus, the design process is faster, though the accuracy of the profile degrades slightly. Another reason underlying this downsampling-upsampling step is that we can apply the root-flip method to further reduce the peak amplitude [Pickup and Ding, 1995], which becomes numerically challenging and potentially ill-conditioned when computing high-degree polynomial roots. Note that factoring high-degree polynomials can be done accurately and fast in some special scenarios with real coefficient polynomials [Sitton

et al., 2003], and it has been applied for the root-flip method for RF pulse design to reduce peak amplitude [Lustig *et al.*, 2006]. This method may not work well for general polynomials such as the complex coefficient polynomials in this case. However the method proposed in [Sitton *et al.*, 2003] to construct a polynomial from its roots can still be applied here to significantly reduce computation error.

Though focused on spectrally selective RF pulses in this work, this method can also be applied for spatially selective RF pulses. For example, for outer volume suppression pulses we could release the constraint on the profile outside of the subject to reduce the transition bandwidth [Stikov *et al.*, 2007].

One limitation of this framework is that the computation time of an optimal FIR filter using the external convex optimization solver (CVX) is up to 1 minute, thus limiting use of this tool in real time during scan prescription. However, for those applications where an optimized RF pulse is desired with multiband profile, the RF pulse can be designed in advance off-line with a careful setting of parameters. For off-line RF pulse design, other design methods exist, such as optimal control algorithm, which offers increased flexibility and may achieve better performance such as increased B_1 insensitivity [Janich *et al.*, 2011].

3.6 Conclusion

A framework for general RF pulse design was developed using the SLR algorithm and convex optimization. This algorithm can create RF pulses with multiband magnitude profile, arbitrary phase profile, and generalized flip angle. Spectral sparsity was exploited to further improve pulse performance in terms of pulse duration, peak amplitude, total energy, transition width, or profile ripple, with flexible trade-offs. We present example designs for shorter duration pulses for a bSSFP ^{13}C sequence at 14T; a dualband saturation pulse with sharper transition widths for ^{1}H MRS at 3T; and a saturation pulse with extremely low stopband ripple for suppression of undesired resonances in HP ^{13}C studies.

3.7 Appendix A FIR Filter Design via Convex Optimization

3.7.1 Direct formulation

Using the following definition of a finite impulse response (FIR) filter with complex coefficients,

$$h = [a(0) + jb(0),\ a(1) + jb(1),\ \ \ldots,\ a(N-1) + jb(N-1)], \tag{3.2}$$

then the filter frequency response by Fourier Transform is

$$H(e^{j\omega}) = \sum_{n=-\infty}^{\infty} h(n)e^{-j\omega n} = H_R(e^{j\omega}) + j \cdot H_I(e^{j\omega}). \tag{3.3}$$

The real and imaginary components will be

$$H_R(e^{j\omega}) = \sum_{n=0}^{N-1}[a(n)\cos(\omega n) + b(n)\sin(\omega n)] = C_\omega^T \mathbf{a} + S_\omega^T \mathbf{b} = \begin{bmatrix} C_\omega^T & S_\omega^T \end{bmatrix} \begin{bmatrix} \mathbf{a} \\ \mathbf{b} \end{bmatrix} = R_\omega^T x \tag{3.4}$$

$$H_I(e^{j\omega}) = I_\omega^T x \tag{3.5}$$

where

$$\begin{aligned}
\mathbf{a} &= \begin{bmatrix} a(0) & a(1) & \dots & a(N-1) \end{bmatrix}^T \\
\mathbf{b} &= \begin{bmatrix} b(0) & b(1) & \dots & b(N-1) \end{bmatrix}^T \\
x &= \begin{bmatrix} \mathbf{a}^T & \mathbf{b}^T \end{bmatrix}^T \\
C_\omega &= \begin{bmatrix} 1 & \cos(\omega) & \dots & \cos(\omega(N-1)) \end{bmatrix}^T \\
S_\omega &= \begin{bmatrix} 0 & \sin(\omega) & \dots & \sin(\omega(N-1)) \end{bmatrix}^T \\
R_\omega &= \begin{bmatrix} C_\omega^T & S_\omega^T \end{bmatrix}^T \\
I_\omega &= \begin{bmatrix} -S_\omega^T & C_\omega^T \end{bmatrix}^T .
\end{aligned}$$

We can also define the square of magnitude of the frequency response as

$$|H(e^{j\omega})|^2 = (H_R(e^{j\omega}))^2 + (H_I(e^{j\omega}))^2 = (R_\omega^T x)^2 + (I_\omega^T x)^2 = x^T D x \tag{3.6}$$

where $D = R_\omega R_\omega^T + I_\omega I_\omega^T \in R^{2N*2N}, \quad D = D^T \succeq 0$

To setup the filter design problem with specification only of the magnitude of the frequency response, we can set upper and lower bounds over the frequency range Ω of interest.

$$(L(e^{j\omega}))^2 \leq |H(e^{j\omega})|^2 \leq (U(e^{j\omega}))^2, \qquad \omega \in \Omega \subseteq [-\pi, \pi] \tag{3.7}$$

For the upper bound, $|H(e^{j\omega})|^2 = x^T D x \leq (U(e^{j\omega}))^2$, which is a quadratic constraint.

However for the lower bound, $|H(e^{j\omega})|^2 = x^T D x \geq (L(e^{j\omega}))^2$, which is a **non-convex constraint** and makes this problem hard to solve.

3.7.2 Power spectrum and autocorrelation formulation

In the work by Wu and Boyd [Wu *et al.*, 1996], the power spectrum $R(e^{j\omega})$ $(= |H(e^{j\omega})|^2)$ is used instead of designing the frequency response directly, which is the Fourier transform of the autocorrelation coefficients, $r(n)$:

$$r(n) = \sum_{k=-\infty}^{\infty} h(k)\overline{h(k+n)} \tag{3.8}$$

where $\overline{h}$ represents the complex conjugate. Also note that

$$\begin{aligned} r(n) &= 0, \quad n \leq -N,\ n \geq N \\ r(0) &\geq 0 \\ r(-n) &= \overline{r(n)}. \end{aligned}$$

To express this filter design formulation in a matrix, we first define $y \in R^{(2N-1)*1}$ as

$$y = \begin{bmatrix} r(0) & \Re(r(1)) & \dots & \Re(r(N-1)) & \Im(r(1)) & \dots & \Im(r(N-1)) \end{bmatrix}^T \tag{3.9}$$

with which we can express the power spectrum as

$$R(e^{j\omega}) = \sum_{n=-\infty}^{\infty} r(n)e^{-j\omega n} = \sum_{n=1}^{N-1}(\overline{r(n)}e^{j\omega n} + r(n)e^{-j\omega n}) + r(0) = B_\omega^T y \tag{3.10}$$

where $B_\omega = \begin{bmatrix} 1 & 2\cos(\omega) & \dots & 2\cos(\omega(N-1)) & 2\sin(\omega) & \dots & 2\sin(\omega(N-1)) \end{bmatrix}^T \in R^{(2N-1)*1}$

Then the frequency response magnitude constraint becomes

$$(L(e^{j\omega}))^2 \leq B_\omega^T y \leq (U(e^{j\omega}))^2, \qquad \omega \in \Omega \subseteq [-\pi, \pi] \tag{3.11}$$

which is a linear constraint. Therefore, by changing variables to constrain the power spec-

trum, the original nonconvex problem is converted into a convex problem (8).

This problem has infinite number of constraints at each frequency. The constraints can be approximated by sampling the frequency to make a finite number of constraints. The frequency samples can be fixed as $-\pi \leq \omega_1 < \cdots < \omega_m \leq \pi$ (for example $\omega_k = (k-m/2)\pi/(m/2), k = 1, 2, \ldots, m$). Choosing $m \gg N$ yields a good approximation (common rule-of-thumb: $m = 15N$).

Once an optimal solution is found, the FIR filter can be obtained via spectral factorization. The frequency response magnitude is $|H(e^{j\omega})| = \sqrt{R(e^{j\omega})}$. As the phase of the frequency response is typically not a concern, we can choose the minimum-phase (mp) filter for simplicity. The log-magnitude and phase of a mp filter are a Hilbert transform pair, which can be used to calculate phase, thus design the complete filter.

For the spectral factorization, $R(e^{j\omega}) \geq 0, \omega \in [-\pi, \pi]$ is a necessary and sufficient condition for the existence of $h(n)$. If this does not hold for all $\omega \in [-\pi, \pi]$, especially between frequency samples, the spectral factorization will fail. As in reference [Wu *et al.*, 1996], failure can be prevented by adding a safety margin with an appropriately small $\epsilon > 0$:

$$R(e^{j\omega_i}) \geq \epsilon, \quad \omega_i \in [-\pi, \pi], i = 1, 2 \ldots m. \tag{3.12}$$

3.7.3 Incorporate other constraints

One advantage of convex optimization is that additional constraints can be added easily if they are also convex. We have included the following additional constraints:

1. **Peak amplitude**: A common problem for SLR RF pulse design is potential large spikes at first/last samples (so-called "Conolly wings"), especially for equal-ripple pulses. In some cases these end-spikes are the peak amplitude, which may go beyond the MRI system limits. In this work we added a constraint to limit end-spikes by empirically assuming that a beta polynomial with lower end-spike will generate a RF

pulse with lower end-spike. We also assumed that the last and first value of the filter are either large or small simultaneously. We have found that these assumptions work well for most applications. This constraint is formulated as:

$$|h(0)|\cdot|h(N-1)| = |h(0)\cdot\overline{h(N-1)}| = |r(N-1)| = || \begin{bmatrix} 0 & \dots & 1 & 0 & \dots & 0 \\ 0 & \dots & 0 & 0 & \dots & 1 \end{bmatrix} y||_2 = ||Fy||_2 \leq \delta_2 \tag{3.13}$$

2. **Total energy**: We also want to minimize the total energy, which can be useful for reducing the Specific Absorption Rate (SAR). Based on Parseval's theorem, this constraint can be expressed by

$$\frac{1}{2\pi}\int_{-\pi}^{\pi} |H(e^{j\omega})|^2 dw = \frac{1}{2\pi}\int_{-\pi}^{\pi} R(e^{j\omega})dw = r(0) \tag{3.14}$$

3. **Minimum stopband ripple**: For some applications we want to minimize the stopband ripple, for example saturation RF pulses with many repetitions. If we define $B_{\omega_i}^T y \leq \delta_1, \quad \omega_i \in \Omega_{stopband} \subseteq [-\pi, \pi]$, then we want to minimize δ_1.

4. **SLR magnitude constraint**: In SLR algorithm, the two polynomials must satisfy the frequency response amplitude constraint $|A_N(z)|^2 + |B_N(z)|^2 = 1$, to be a valid representation of a rotation, as in [Pauly *et al.*, 1991]. So the FIR filter, as the beta polynomial, must satisfy $|H(e^{j\omega})| \leq 1$ for all $\omega \in [-\pi, \pi]$. Similarly to adding a safety margin for the spectral factorization, we can also add a safety margin here to make sure this magnitude constraint holds for all frequencies, especially between frequency samples.

$$R(e^{j\omega_i}) \leq 1 - \epsilon_2, \quad \omega_i \in [-\pi, \pi], i = 1, 2 \dots m. \tag{3.15}$$

The entire filter design problem can be expressed as a convex optimization problem, including the additional constraints described above :

$$\begin{array}{lll} \textit{minimize} & y(1) + \lambda \cdot \delta_1 & \\ \textit{variable} & y \in R^{(2N-1)*1},\ \delta_1 \in R & \\ \textit{subject to} & B_{\omega_i}^T y \geq \epsilon & -\pi \leq \omega_i \leq \pi \\ & B_{\omega_i}^T y \leq 1 - \epsilon_2 & -\pi \leq \omega_i \leq \pi \\ & (L(e^{j\omega_i}))^2 \leq B_{\omega_i}^T y \leq (U(e^{j\omega_i}))^2 & -\pi \leq \omega_i \leq \pi \\ & B_{\omega_i}^T y \leq \delta_1 & \omega_i \in \Omega_{stopband} \subseteq [-\pi, \pi] \\ & ||Fy||_2 \leq \delta_2. & \end{array} \tag{3.16}$$

3.8 Appendix B SLR Parameter Relation with Generalized Flip Angles

When designing a RF pulse, we usually specify the desired pulse profile such as passband and stopband edges, flip angles, and passband and stopband ripples. Since the SLR algorithm reduces RF pulse design to a FIR filter design problem, then the corresponding specification on the FIR filter needs to be derived first. This is particularly important for the ripples specifications, in other words, the specifications of the range of the frequency response magnitude.

In this work the ripple is defined as the absolute value ($a \pm \delta$) instead of relative value ($a(1 \pm \delta)$) as previously used in [Pauly *et al.*, 1991], because scaling can be confusing for multiband pulses with different flip angles in different bands.

For a RF pulse with selective excitation along the x direction, specified by flip angle $\theta(x)$, the final rotation state is

$$\beta_N(x) = -i(n_x + in_y)\sin(\theta(x)/2) \tag{3.17}$$

where $\mathbf{n} = [n_x, n_y, n_z]^T$ is the rotation axis. The two SLR polynomials are defined as $A_N(z) = z^{-N/2}\alpha_N$ and $B_N(z) = z^{-N/2}\beta_N$, where $z = e^{i\gamma Gxdt}$, and so

$$|B_N(z)| = |\beta_N(x)| = \sin(\theta(x)/2). \tag{3.18}$$

For an excitation pulse, the initial magnetization lies along the longitudinal direction, and the profile of interest is transverse magnetization $M_{xy}(x)$:

$$|M_{xy}(x)| = |2\alpha^*\beta| = |2A_N(z)^*B_N(z)| = \sin(\theta(x)). \tag{3.19}$$

Given the range of magnetization profile amplitude, $[|M_{xy}|_{min},\ |M_{xy}|_{max}]$, we can calculate a range of flip angles, $[\theta_{min},\ \theta_{max}]$, by inverting equation 3.19. Then the range of $|B_N(z)|$ can be calculated easily by equation 3.18. Note that $|B_N(z)| = \sin(\theta/2)$ is an increasing function for $\theta \in [0 \quad \pi)$, while $|M_{xy}| = \sin(\theta)$ is not. So care must be taken for the first step. Also note that the ripple is usually non-symmetric about the desired value.

For saturation and inversion pulses, the initial magnetization is along the longitudinal direction, and the profile of interest is $M_z(x)$:

$$M_z(x) = 1 - 2\beta\beta^* = 1 - 2|B_N(z)|^2 = \cos(\theta(x)). \tag{3.20}$$

Similarly, given the range of magnetization profile, $[(M_z)_{min},\ (M_z)_{max}]$, we can calculate the range of flip angle, $[\theta_{min},\ \theta_{max}]$, by inverting equation 3.20, then figure out the range of $|B_N(z)|$ by equation 3.18.

No approximation is used in this approach, so the result ripple relation is precise, and it requires negligible computation time. A similar approach for refocusing pulses can be easily derived based on a similar formulation in reference [Pauly *et al.*, 1991], which is not shown here.

Chapter 4

Spectrally Selective 3D Dynamic Balanced SSFP for Hyperpolarized ^{13}C Metabolic Imaging

4.1 Abstract

Balanced steady state free precession (bSSFP) sequences can provide superior SNR efficiency for hyperpolarized ^{13}C MRI by efficiently utilizing the non-recoverable magnetization, but managing their spectral response is challenging in the context of metabolic imaging. A new spectrally selective bSSFP sequence was developed for fast imaging of multiple hyperpolarized ^{13}C metabolites with high spatiotemporal resolution. This novel approach for bSSFP spectral selectivity incorporates optimized short duration spectrally selective RF pulses within a bSSFP pulse train and a carefully chosen TR to avoid banding artifacts. The sequence enabled sub-second 3D dynamic spectrally selective imaging of ^{13}C metabolites of co-polarized [1-^{13}C]pyruvate and [^{13}C]urea at 2mm isotropic resolution, with excellent spectral selectivity (≈100:1). The sequence was successfully tested in phantom studies and in vivo studies with normal mice. This sequence is expected to benefit applications requiring dynamic volumetric imaging of metabolically active ^{13}C compounds at high spatiotemporal resolution including preclinical studies at high field and potentially clinical studies.

4.2 Introduction

Hyperpolarized (HP) ^{13}C MRI with dissolution Dynamic Nuclear Polarization (DNP), with its sensitivity enhancements of >10,000 fold over thermal equilibrium values, enables non-invasive, spatially localized measurements of the enzymatic conversions of endogenous, non-toxic ^{13}C-labeled probes through key biochemical pathways [Ardenkjær-Larsen *et al.*, 2003; Golman *et al.*, 2006]. This technology is distinguished by the capability to simultaneously image both injected agents and their downstream metabolic products separately, based on their unique chemical shifts. HP ^{13}C MRI has been successfully applied in numerous preclinical studies, and a recent clinical trial in prostate cancer patients showed safety and feasibility of this approach for investigating human disease [Nelson *et al.*, 2013; Kurhanewicz *et al.*, 2011].

Unique challenges faced in HP ^{13}C metabolic imaging include the non-recoverable nature of HP magnetization and the complex pattern of resonances that must be spectrally resolved. Rapid and efficient MRI pulse sequences are required to acquire data within the limited temporal window dictated by the rapid irreversible T_1 decay of HP magnetization. Various approaches for MR spectroscopic imaging (MRSI) have been applied for HP ^{13}C, including standard chemical shift imaging (CSI) [Golman *et al.*, 2006], echo-planar spectroscopic imaging (EPSI) [Larson *et al.*, 2008; Larson *et al.*, 2011; Cunningham *et al.*, 2007], and spiral CSI [Mayer *et al.*, 2009]. These MRSI sequences have high spectral resolution but are generally limited by low spatiotemporal resolution. Alternatively, by exploiting a priori knowledge of the spectral distribution of resonances, spatiotemporal resolution can be improved at the expense of spectral resolution. Examples of this approach include spectrally selective imaging with multi-echo chemical shift separation [Reeder *et al.*, 2007], and spectral-spatial excitation of individual metabolites followed by spiral [Lau *et al.*, 2010; Schulte *et al.*, 2013] or echo-planar imaging readouts [Cunningham *et al.*, 2008; Miller *et al.*, 2015].

A balanced steady state free precession (bSSFP) sequence offers substantial advantages for HP ^{13}C imaging with improved spatiotemporal resolution. Due to their high SNR efficiency, bSSFP sequences are routinely used for rapid morphological and cardiac ^{1}H MRI [Scheffler and Lehnhardt, 2003; Bieri and Scheffler, 2013]. A bSSFP approach has been previously applied for HP ^{13}C perfusion imaging and angiography using metabolically inactive agents with a single HP resonance [Svensson *et al.*, 2003; von Morze *et al.*, 2011a; Reed *et al.*, 2014; Reed *et al.*, 2015]. Compared to small flip angle spoiled gradient echo acquisitions [Reeder *et al.*, 2007; Lau *et al.*, 2010; Schulte *et al.*, 2013; Cunningham *et al.*, 2008; Miller *et al.*, 2015], the bSSFP sequence can more efficiently utilize the non-recoverable magnetization by preserving transverse magnetization across multiple TR's, which is especially valuable for ^{13}C nuclei with long T_2's [Reed *et al.*, 2014]. The bSSFP sequence incorporates the desirable refocusing performance of spin echo sequences [Scheffler and Hennig, 2003] with the flexibility to operate in the small flip angle regime to maximize the temporal window for dynamic data acquisition, with short TR and high sampling efficiency. The bSSFP sequence is also relatively insensitive to B_1 variation or miscalibration of transmitter gain [Cunningham *et al.*, 2007].

However, managing the spectral response of bSSFP sequences is difficult in the context of HP ^{13}C metabolic imaging, which has unique additional challenges as compared to spectrally selective ^{1}H bSSFP (i.e. water-fat separation), including: 1) Typically there are several resonances (>2) that need to be separated; 2) Quantitative measurement of each compound is required, hence reducing one component qualitatively is not an option (i.e. fat suppression); 3) HP magnetization decays irreversibly and cannot be recovered once saturated; 4) Fast acquisition is required due to rapid metabolic conversion and HP signal decay; and 5) HP signal necessarily evolves in a transient state, as there is no true steady state. These additional considerations limit the usage of some previous methods developed for ^{1}H bSSFP water-fat separation, such as insertion of a spectrally selective saturation pulse in steady state [Scheffler *et al.*, 2001], which will cause irreversible HP signal loss; phase detection [Hargreaves *et*

al., 2003], which is most suitable for separating only two compounds and suffers from the partial volume effect; fluctuating equilibrium [Vasanawala *et al.*, 1999] and other similar approaches taking advantage of banding artifact [Vasanawala *et al.*, 2000; Overall *et al.*, 2003; Absil *et al.*, 2006], which cannot provide enough suppression for quantitative measurement.

Several bSSFP approaches for spectrally selective HP ^{13}C metabolic imaging have been developed, including methods based on multi-echo Dixon-type separation [Leupold *et al.*, 2009], metabolite-specific imaging using the low flip angle frequency response [von Morze *et al.*, 2013; Månsson *et al.*, 2012], chemical shift separation with low readout bandwidth [von Morze *et al.*, 2011b; Morze *et al.*, 2014], and fitting of multiple acquisitions with variable phase advance [Varma *et al.*, 2015]. However, these methods have various respective limitations including: 1) long TR [Leupold *et al.*, 2009; Morze *et al.*, 2014], 2) narrow excitation bandwidth ($\approx \pm$10Hz) and suboptimal SNR [von Morze *et al.*, 2013; Månsson *et al.*, 2012], 3) low readout bandwidth and requirement for wide spectral separation [Morze *et al.*, 2014], and 4) several assumptions required including ignoring T_1 and T_2, knowledge of B_0 map and exact flip angle, and establishment of steady state [Varma *et al.*, 2015]. For methods simultaneously exciting all compounds [Leupold *et al.*, 2009; Varma *et al.*, 2015], a complicated spectroscopic reconstruction is required, which may be prone to error and could result in spurious local images in areas with imperfect shims. Off-resonance insensitivity is degraded by either narrow excitation bandwidth [von Morze *et al.*, 2013; Månsson *et al.*, 2012], long TR [Leupold *et al.*, 2009; Morze *et al.*, 2014], or less robust reconstruction [Leupold *et al.*, 2009; Varma *et al.*, 2015].

In this project, we developed a new method for spectrally selective bSSFP for fast imaging of multiple HP ^{13}C metabolites with high spatiotemporal resolution that, compared to previous methods, is more insensitive to off-resonance and more SNR efficient with simple and robust reconstruction. The key feature of this new pulse sequence is a combination of novel optimized short duration spectrally selective RF pulses [Shang *et al.*, 2016] and a bSSFP pulse train with a carefully chosen TR to avoid banding artifact. In this

study, we tested this new sequence in phantoms and then applied it for in vivo HP ^{13}C mouse imaging at 14T with 2mm isotropic spatial resolution and <1s temporal resolution. Co-polarized [1-^{13}C]pyruvate and [^{13}C]urea [Wilson *et al.*, 2010] were used as the injected substrates, which allows for combined perfusion and metabolic imaging. Several previous clinical studies have shown that a perfusion-metabolism mismatch is associated with adverse disease features in human cancers [Aronen *et al.*, 2000; Komar *et al.*, 2009; Mankoff *et al.*, 2002], and therefore combined imaging of perfusion and metabolism could provide improved classification of individual cancers.

4.3 Theory

The bSSFP pulse train has an intrinsic periodic frequency response with periodicity 1/TR, as shown in Figure 4.1 (A, B). With alternating 1/-1 RF modulation, spins around the center of each cycle (f= $\cdots$, -1/TR, 0, 1/TR, $\cdots$) behave as desired, in that a large flip angle excites magnetization while a small flip angle has little effect on spins. The opposite behavior exists at the edge of each cycle (f= $\cdots$, -1/(2TR), 1/(2TR), $\cdots$), where a large flip angle results in little longitudinal and transverse magnetization while a small flip angle produces significant excitation over a small frequency range.

Previous studies have employed excitation by a non-selective RF pulse with either large flip angles and metabolites placed near the center of each cycle [Leupold *et al.*, 2009; Morze *et al.*, 2014], or small flip angles with metabolites placed near the edge of each cycle [von Morze *et al.*, 2013; Månsson *et al.*, 2012; Varma *et al.*, 2015]. If spectrally selective RF pulses are used in a bSSFP pulse train, the overall spectral selectivity is a coupling of the frequency response of the RF pulse and the bSSFP pulse train. Assuming an ideal selective RF pulse is used (Figure 4.1(C)), the overall spectrally selective profile will have a passband at the same frequency as the RF pulse profile passband. However, there are also undesired narrow excitation bands at the edge of each cycle due to accumulated small flip angle excitations,

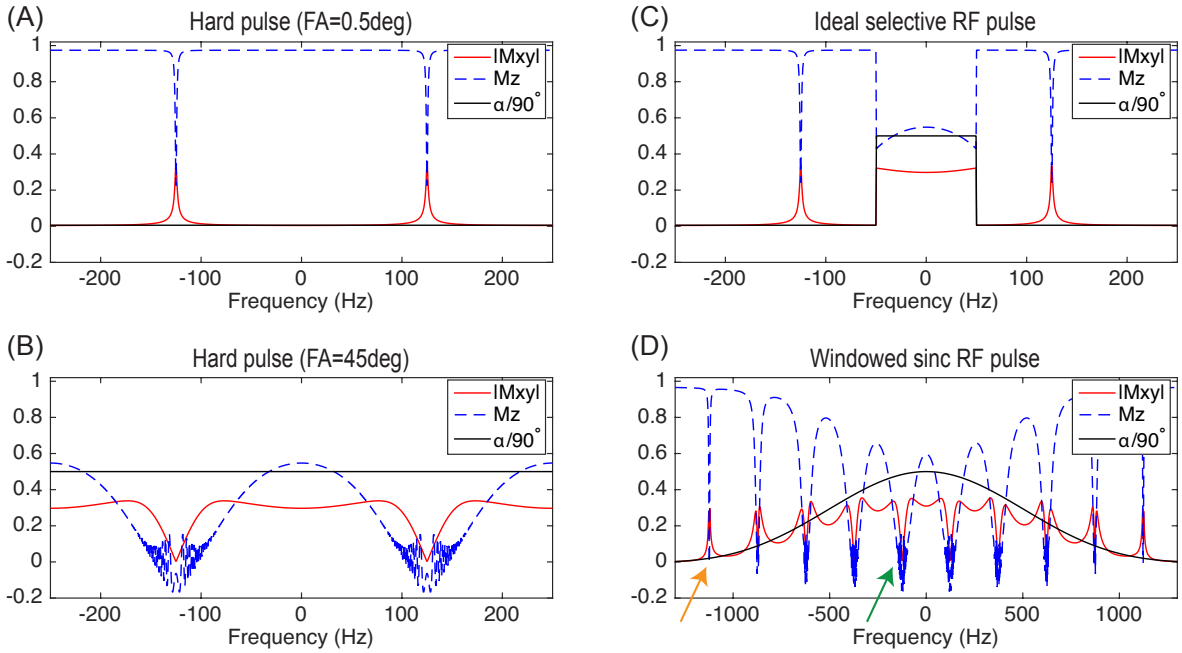

Figure 4.1: bSSFP frequency response with small flip angle (0.5°) hard pulse (A), large flip angle (45°) hard pulse (B), ideal selective RF pulse (passband/stopband flip angle = 45°/0.5°) (C), and a windowed sinc RF pulse (flip angle = 45°, duration = 2ms, bandwidth = 1kHz). $|Mxy|$ is the averaged transverse magnetization over all echoes during transient state, Mz is the longitudinal magnetization after the last echo, $\alpha/90°$ is RF pulse excitation flip angle divided by 90°. Simulation parameters included: number of echoes = 256, TR = 4ms, T_1 = 40s, T_2 = 300ms, and linear ramp preparation pulse (N = 5).

which will be termed "excitation banding artifact" (to distinguish from the more common notion of bSSFP banding artifact corresponding to image signal loss). The RF pulse in Figure 4.1(C) is infeasible since selective RF pulses have finite pulse duration and transition from passband to stopband in the pulse profile. The bSSFP frequency response with a spectrally selective windowed sinc RF pulse is shown in Figure 4.1(D), with RF pulse profile passband covering multiple cycles (1/TR). Excitation banding artifact occurs at RF pulse profile stopband (orange arrow in Figure 4.1(D)), while banding artifact corresponding to signal loss occurs at passband (green arrow in Figure 4.1(D)),

In this method, spectrally selective RF pulses are used to excite a single metabolite per acquisition. The undesired excitation banding artifacts are avoided by carefully choosing TR to place all resonance peaks close to center of each cycle. The resonance frequency of each compound is fixed, while the bSSFP frequency response can be widened or narrowed by decreasing or increasing TR. A different optimized RF pulse waveform and TR was designed for selective imaging of each metabolite. An implementation of this approach is shown in Figure 4.2, designed for selectively exciting pyruvate in experiments with co-polarized substrate [1-^{13}C]pyruvate and [^{13}C]urea. Resonance peaks of urea, pyruvate, pyruvate hydrate, and metabolic products (alanine, lactate) at 14T are considered (Figure 4.2(A)). To increase insensitivity to B_0 inhomogeneity, a finite bandwidth around each resonance frequency ($\pm$50Hz) is specified, within which a uniform spectrally selective profile is desired. Pyruvate is specified to be in the RF pulses passband while the other four resonances are specified as stopbands. Nevertheless, due to the bSSFP frequency response, there can be excitation even with the low flip angle produced in the RF pulse's stopbands (Figure 4.2(B)). For example, choosing a suboptimal TR of 4ms results in the urea, alanine and lactate stopbands being near the excitation banding artifact frequency (red arrow in Figure 4.2(C)), and the simulated urea stopband shows an undesired narrow excitation peak (Figure 4.2(E)). Thus, in this method, it is important to choose a proper TR. In this example, with an optimal TR of 3.8ms, all bands are located close to center of a cycle (Figure 4.2(D)), and the simulated

urea stopband shows negligible excitation (Figure 4.2(F)). The excitation passband is always placed around center (f = 0) for larger bandwidth and higher SNR efficiency, compared to being located at band edge with small flip angle [von Morze *et al.*, 2013; Månsson *et al.*, 2012; Varma *et al.*, 2015].

Spectrally selective RF pulses are usually not used in bSSFP due to long pulse duration. An optimized selective RF pulse with the shortest possible duration [Shang *et al.*, 2016] was used to keep TR and total scan time short. The minimum pulse duration was achieved by exploiting spectral sparsity, specifying a multiband profile and releasing the constraint on "don't-care" regions [Shang *et al.*, 2016]. The optimal pyruvate/lactate/urea excitation pulse had durations of 1.40ms/2.04ms/1.04ms, much shorter than a conventional RF pulse design with minimum-phase low-pass filter (≈5ms), with one example shown in Figure 4.3(C,D) and more detailed comparison in [Shang *et al.*, 2016].

A set of ramp-up preparation pulses was applied before acquisition (Figure 4.3 (A)), to reduce transient state signal oscillations and achieve pseudo steady-state (Figure 4.3 (B)) [Deshpande *et al.*, 2003; Le Roux, 2003; Paul and Hennig, 2004]. A set of ramp-down pulses was applied after the acquisition to flip magnetization back to Mz to increase signal in subsequent acquisitions. Similar to how the ramp up preparation pulse outperforms the $\alpha/2$ - TR/2 preparation pulse by working for a larger range of off-resonance frequencies [Paul and Hennig, 2004], this ramp-down flip back pulse is also more insensitive to off-resonance compared to the conventional driven equilibrium pulse [Svensson *et al.*, 2003]. Besides, a RF pulse with duration longer than TR/2 can be fit in the ramp down flip back pulse, but not in the driven equilibrium pulse with TR/2 interval. The flip angle modulation of preparation pulse and flip back pulse is achieved by linearly scaling RF pulse amplitude. However, the optimized RF pulse is designed based on the Shinnar-Le Roux algorithm [Shang *et al.*, 2016] so the pulse profile gets degraded after scaling [Pauly *et al.*, 1991]. This is not very problematic in our dynamic studies with primarily small flip angles ($< 50°$).

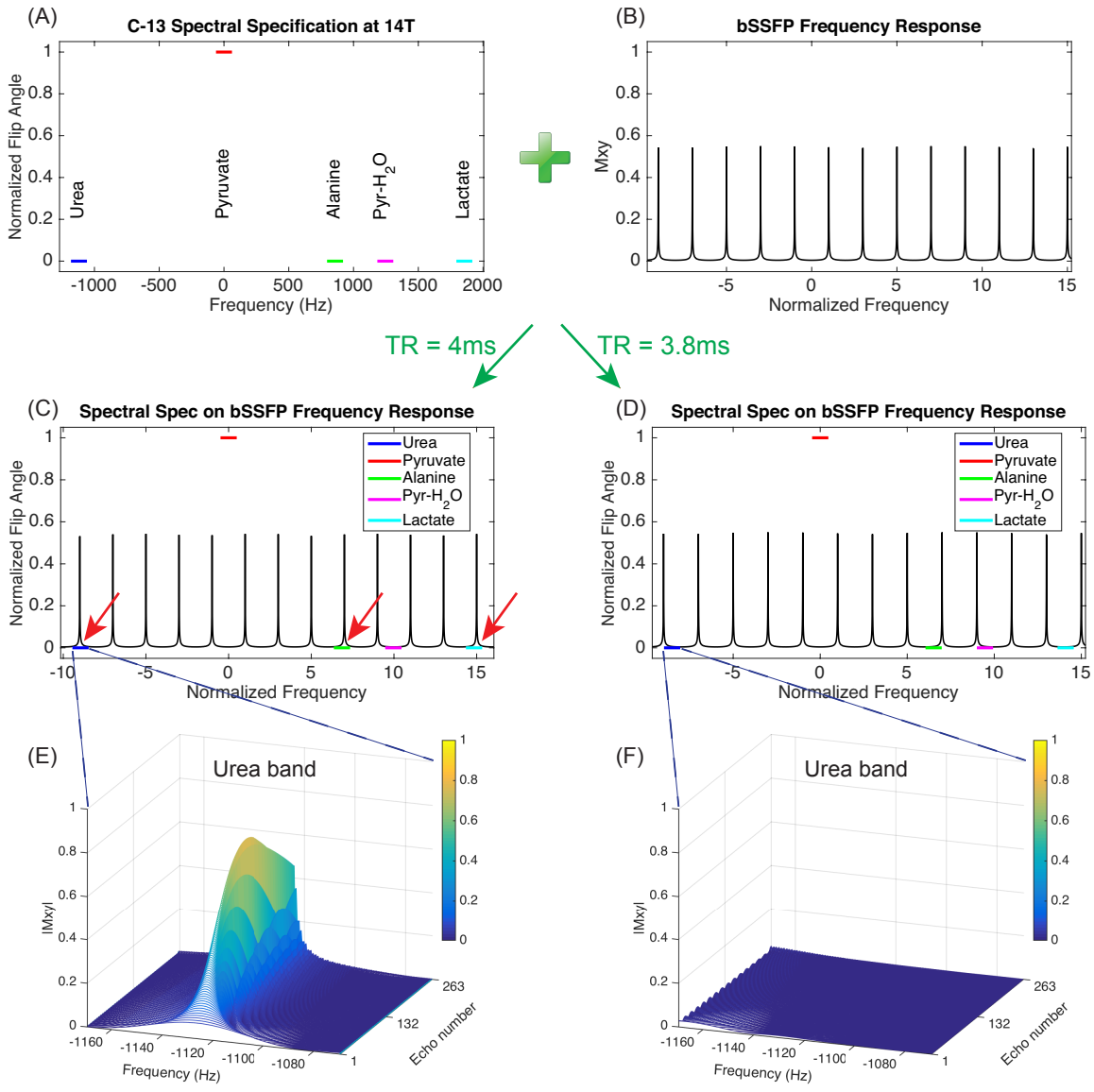

Figure 4.2: Diagram of TR selection process for avoiding excitation banding artifact. Multiband spectral specification of urea, pyruvate, pyruvate hydrate, alanine and lactate in this implementation (selective excitation of pyruvate), with height corresponding to the desired RF pulse excitation flip angle and with finite bandwidth ($\pm$50Hz) for improving B_0 insensitivity (A). bSSFP frequency response with low flip angle (0.5°) (B). Normalized frequency is frequency over $1/(2TR)$. Locate spectral specification on top of bSSFP frequency response with suboptimal TR of 4ms (C), and optimal TR of 3.8ms (D). Simulated transient state echo train within urea stopband with TR of 4ms (E), and TR of 3.8ms (F). Simulation parameters include: number of echoes = 256, T_1 = 30s, T_2 = 1s, $\alpha/2$ - TR/2 preparation pulse.

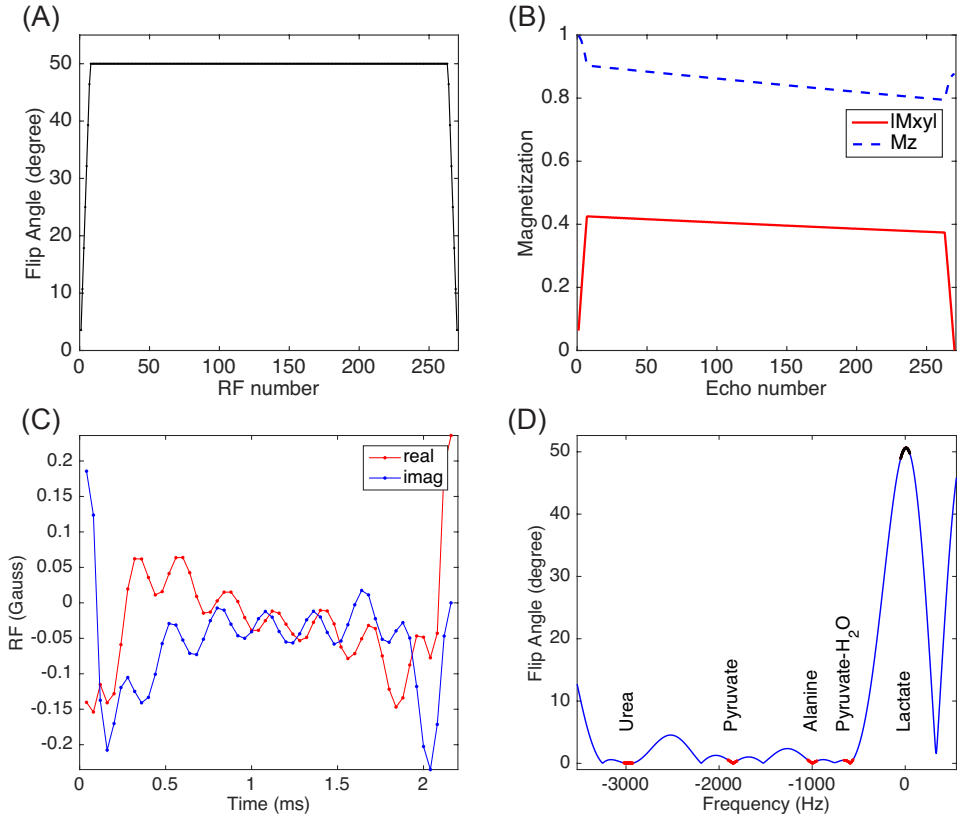

Figure 4.3: Flip angle scheme including a ramp-up preparation pulse and ramp-down flip back pulse (A). Simulated on-resonance magnetization evolution (B). Simulation parameters include: number of echoes = 256, T_1 = 40s, T_2 = 1s, TR = 3.785ms. Optimized lactate-only RF pulse with shortest duration (C), and its simulated spectral profile (D).

4.4 Methods

4.4.1 Bloch simulation

Though the RF pulses used in this study were optimized with shorter duration compared to conventional SLR pulses, the pulse durations (1∼2ms) still take a considerable fraction of TR (3∼4ms), thus violating the assumption of an instantaneous RF pulse, which is utilized in the common bSSFP theoretical framework. Therefore, T_1 and T_2 relaxation and off-resonance induced rotation can no longer be ignored during the RF pulse. The finite RF pulse effect has been studied previously and an analytical modification of bSSFP signal formulation was derived for steady-state signal [Bieri and Scheffler, 2009]. However, bSSFP transient state signal is used for HP ^{13}C imaging, and a general analytical correction for the finite RF pulse effect is difficult to obtain, given the time dependent signal and arbitrary RF pulse waveform. Therefore, a numerical Bloch simulation was performed to compare bSSFP transient state signal evolution with both an ideal instantaneous RF pulse and the actual RF pulse used in this study, using a matrix formulation of the Bloch equation [Jaynes, 1955; Freeman and Hill, 1971; Hargreaves *et al.*, 2001; Scheffler, 2003]. Both signal at echo time (TE=TR/2) and signal evolutions between two RF pulses were simulated. For the ideal instantaneous RF pulse, a constant flip angle at all frequencies was assumed. The ramp up preparation pulse and ramp down flip back pulse were also included in the simulation.

4.4.2 Hardware

The pulse sequence was implemented on a 14.1T vertical Varian NMR microimaging system (Agilent Technologies, Santa Clara, CA, USA) with a 38mm dual-tuned (^{13}C/^{1}H) volume RF coil. A custom 3D bSSFP sequence was implemented with optimized RF pulses. The sequence can run dynamically and cycle the transmit frequency among the Larmor frequencies of pyruvate, lactate and urea when images are acquired for each metabolite. The RF

transmit gain was calibrated with a ^{13}C-enriched urea phantom, placed near the center of the RF coil. Dissolution DNP was performed with a HyperSense polarizer (Oxford Instruments, Oxford, UK) operating at 1.3 K and 3.35 T.

4.4.3 Phantom Measurements

The spectral selectivity of the sequence was tested using a [1-^{13}C]lactate phantom (at thermal equilibrium instead of HP state). To test the spectral selectivity at the resonance frequency of each metabolite without preparing a separate phantom for each metabolite, the transmitter frequency was cycled through several values so that the relative frequency of the lactate phantom corresponded to the chemical shift difference of each ^{13}C compound at 14T, including urea, pyruvate, alanine, pyruvate hydrate, and lactate. Two values of TR were tested when exciting pyruvate only, as shown in Figure 4.2: an optimal TR of 3.8ms that avoids excitation banding artifact, and a suboptimal TR of 4ms. A pyruvate-only RF pulse was used with flip angle of 120° and pulse duration of 1.8ms. Other sequence parameters were the same as the in vivo experiments, which will be introduced later.

The sequence was also tested with phantoms containing HP [1-^{13}C]pyruvate, [1-^{13}C]lactate or [^{13}C]urea solution individually. For each of these three compounds, the compound was individually polarized and then spectrally selective images of all three resonances were acquired. The sequence parameters were the same as the in vivo study, except with 1s delay after one cycle of pyruvate-lactate-urea acquisitions (no delay within this cycle). Spectral selectivity was measured based on image intensity and normalized among images acquired with the same HP sample. For example, the spectral selectivity of pyruvate:urea was calculated by the image intensity of pyruvate acquisition with HP urea sample over the image intensity of urea acquisition with the same HP urea sample. The spectral selectivity calculated in this way depends on flip angle and ordering of acquisition. Since the same sequence was intended for the in vivo study, this spectral selectivity provided insight as to the capability

for resolving these resonances in vivo, and as to the extent of signal contamination from other metabolites in each metabolite-specific image.

4.4.4 In vivo Experiments

Five normal mice were imaged under a protocol approved by the UCSF Institutional Animal Care and Use Committee, as previously described [Albers *et al.*, 2008]. A 350 μL HP solution (80mM [1-^{13}C]pyruvate + 120mM [^{13}C, $^{15}N_2$]urea, pH $\sim$ 7.5, room temperature) was injected into the mouse tail vein catheter over 12s with image acquisition starting at 15s after the beginning of the injection. HP pyruvate, lactate and urea images were acquired sequentially with respiratory triggering ($\sim$1Hz) (one acquisition per respiratory cycle). Six time points were acquired (18 acquisitions in total, $\sim$18s). The sequence parameters for pyruvate/lactate/urea acquisition included: TR = 3.362ms/3.785ms/2.617ms; TE = TR/2; flip angle = 15°/40°/20°; RF pulse duration = 1.40ms/2.04ms/1.04ms; sequence duration = 0.861s/0.969s/0.670s; readout bandwidth = 35.7kHz; FOV = 64x32x32mm^3; nominal spatial resolution = 2x2x2mm^3; matrix size = 32x16x16; number of echoes = 256; number of ramp up preparation pulses = 7; number of ramp down flip back pulses = 7. T_2 weighted coronal multislice ^{1}H images were also acquired for anatomical reference and overlay of ^{13}C images. The B_0 map was measured from ^{1}H signal using a gradient echo sequence, repeated at two echo times (ΔTE = 1ms), and then converted to the off-resonance frequency distribution of ^{13}C.

4.5 Results

4.5.1 Bloch simulation

The qualitative study of the finite RF pulse effect on bSSFP transient state signal demonstrated close correspondence to the ideal case of an instantaneous RF pulse, in terms of both

echo signal amplitude and refocusing performance, as shown in Figure 4.4. For both cases, the echo is gradually formed during the ramp up preparation pulse and maintained during the acquisition. Therefore, previous bSSFP theory can be directly applied here. This insight also applies to ^{1}H bSSFP, which is also commonly performed at transient state to reduce waiting time required to reach the steady state, and also has RF pulses taking a considerable fraction of TR due to SAR or peak B_1 limitations.

4.5.2 Phantom Measurements

Pyruvate-only acquisitions with ^{13}C enriched phantom at the resonance frequency of multiple compounds are shown in Figure 4.5. With a properly chosen TR of 3.8ms, signal is only detected at the pyruvate frequency. Such selectivity was not achieved with a poor TR choice, such as the top row with TR of 4ms, which suffers from excitation banding artifacts. This failed selectivity at urea/alanine/lactate band agrees with the simulation results in Figure 4.2(C) where those bands touch the excitation banding artifact region when TR = 4ms.

bSSFP images of HP phantoms are shown in Figure 4.6, with measured spectral selectivity labeled on each image. One example of dynamic images with HP lactate phantom is shown in Figure 4.7. The data fit well to exponential decay curves with time constants of 26.9s (Pyruvate), 11.6s (Lactate) and 18.6s (Urea).

4.5.3 In vivo Experiments

In vivo 3D dynamic bSSFP images of one mouse are shown in Figure 4.8 (all coronal slices at the first time point) and Figure 4.9 (all time points at one coronal slice). Metabolite dynamic curves measured in kidney and aorta are shown in Figure 4.9(C,D). For injected pyruvate and urea, strong signal was observed in the aorta at early time points as expected. Urea and pyruvate also appeared in kidneys, concentrated in the cortex. Lactate, converted from pyruvate, was also observed, mostly in kidneys as expected.

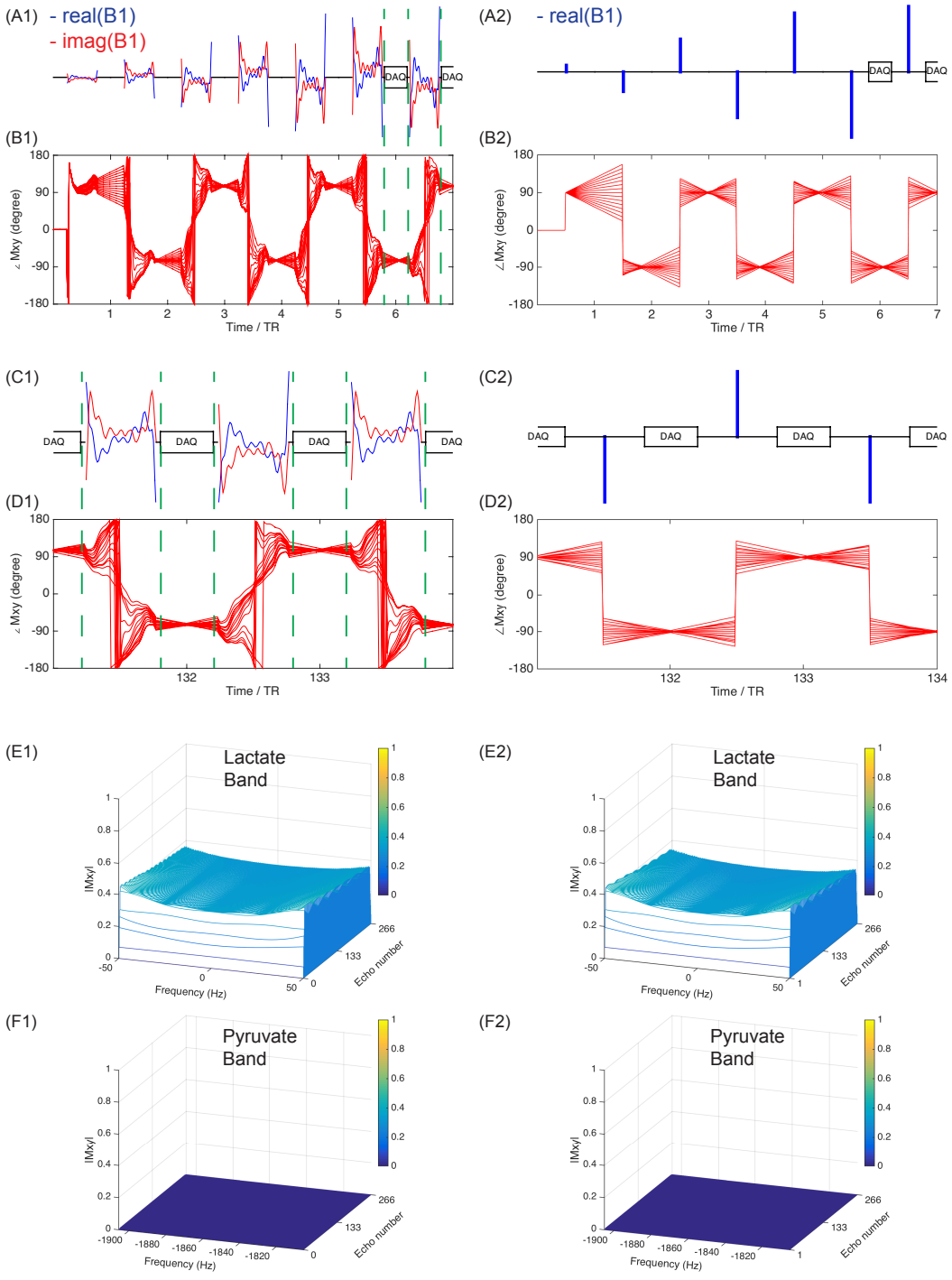

Figure 4.4: Bloch simulation of bSSFP signal evolution with finite RF pulse (left) and instantaneous RF pulse (right). RF pulse train at beginning including ramp up preparation pulses (A1,A2), and the corresponding Mxy phase evolution for spins within the specified passband ([-50Hz,50Hz]) (B1,B2). Three RF pulses in the middle of acquisition (C1,C2), and the corresponding Mxy phase evolution (D1,D2). Transient state echo signal within lactate passband (E1,E2) and pyruvate stopband (F1,F2). Simulations parameters included: number of echoes = 256, number of preparation pulses = 5, number of flip back pulses = 5, TR = 3.785 ms, T_1 = 40s, T_2 = 1s, RF pulse passband flip angle = 40°, duration = 2.04ms.

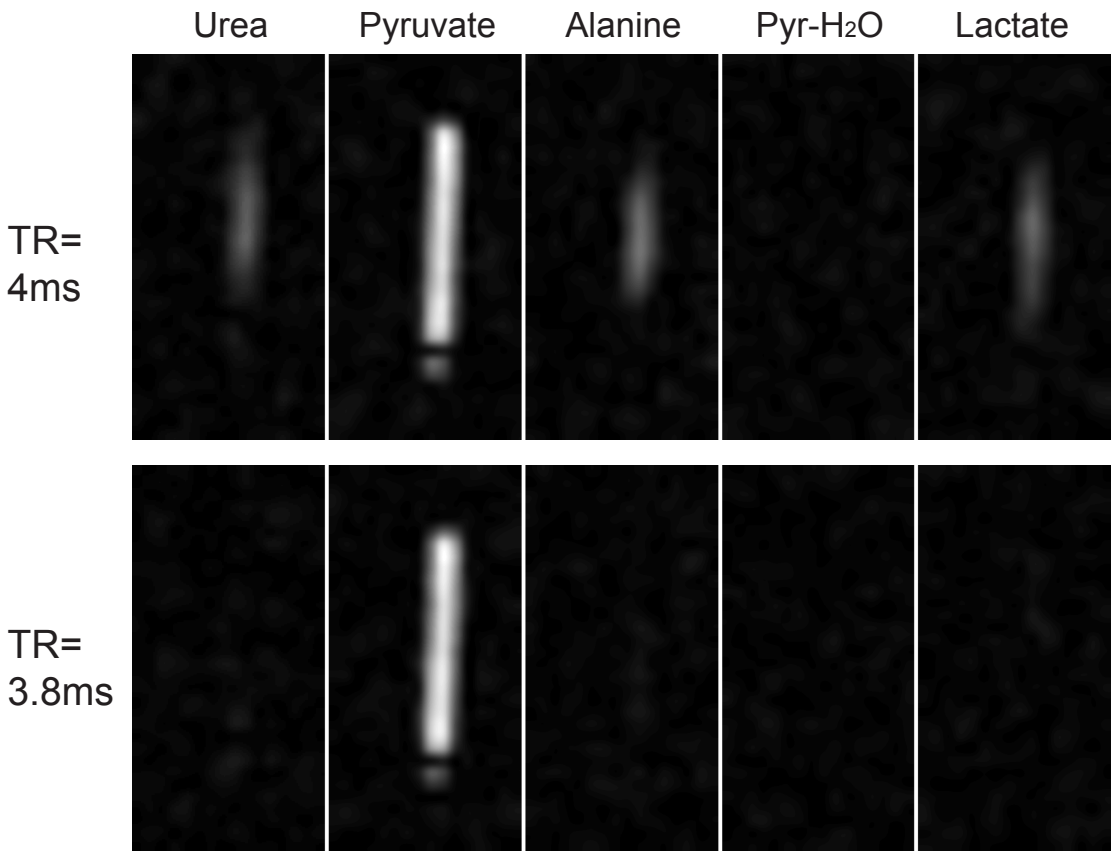

Figure 4.5: One coronal slice of 3D bSSFP pyruvate acquisition with ^{13}C enriched phantom at the resonance frequency of urea/pyruvate/alanine/pyruvate-hydrate/lactate, with TR of 4ms (top row) and 3.8ms (bottom row). All images in each row are displayed with the same window-level.

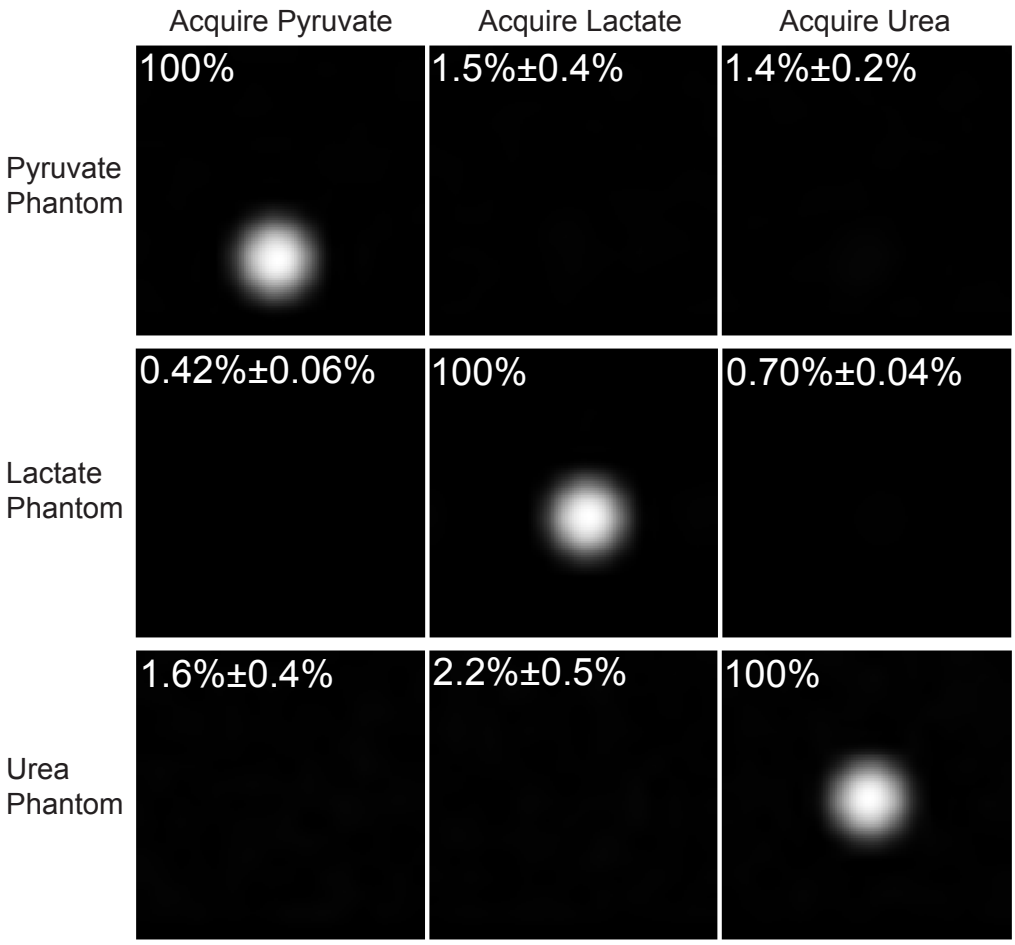

Figure 4.6: One axial slice of 3D dynamic bSSFP pyruvate/lactate/urea acquisition (at first time point) with HP pyruvate/lactate/urea phantoms individually. Measured spectral selectivity is indicated on each image. All images in each row are displayed with the same window-level.

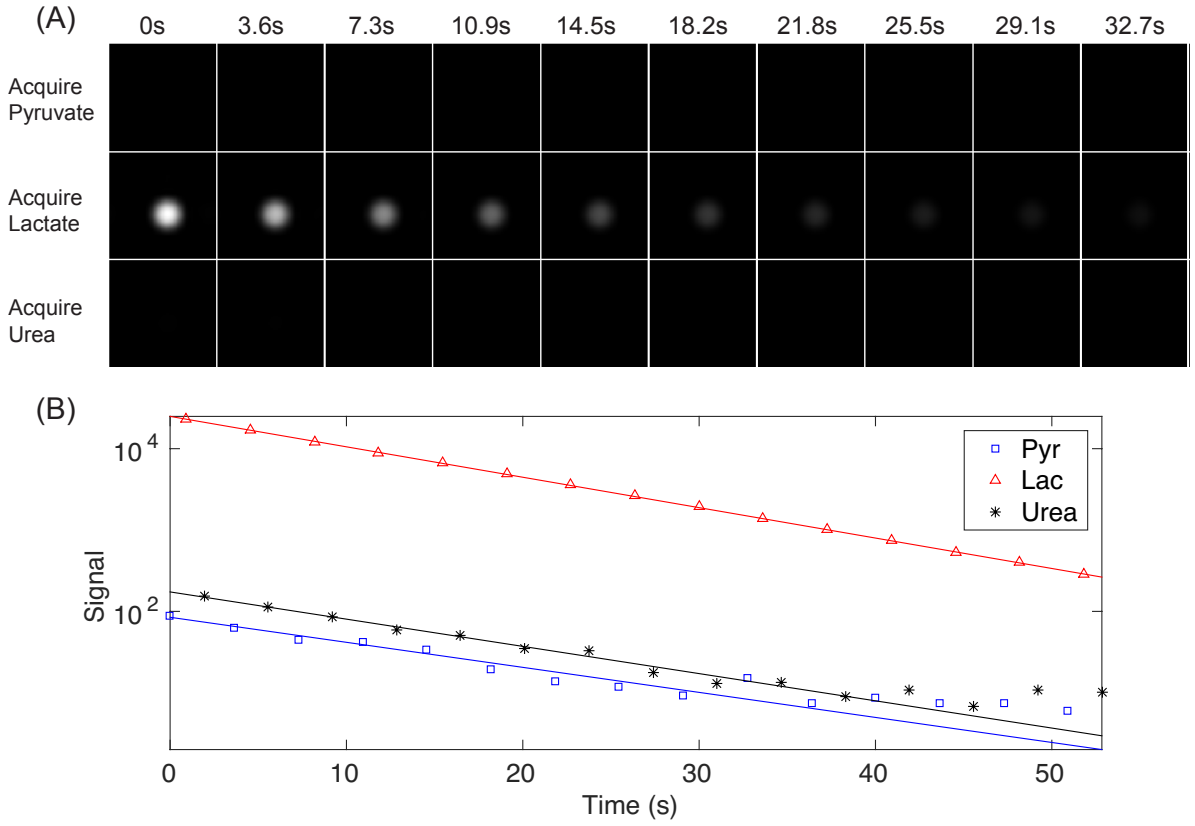

Figure 4.7: For the same data in Figure 4.6, pyruvate/lactate/urea dynamic acquisition with HP lactate phantom, displaying one axial slice at all time points with the same window-level (A). Measured signal plotted with a logarithmic scale (B).

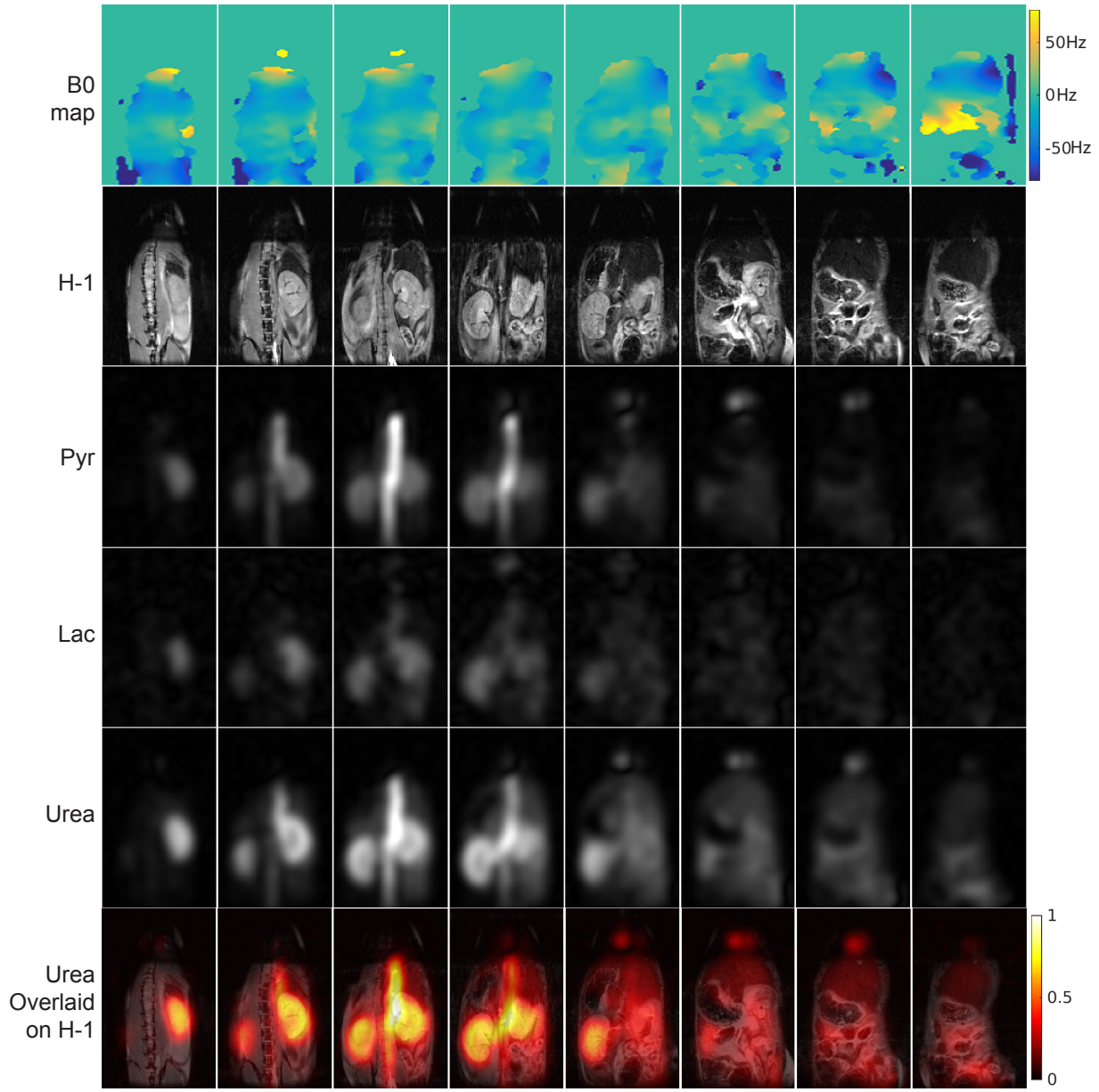

Figure 4.8: 3D dynamic bSSFP in vivo images of HP pyruvate/lactate/urea in a normal mouse with injected co-polarized [1-^{13}C]pyruvate and [^{13}C]urea. Coronal slices at the first time point are displayed (3rd - 5th row), together with corresponding off-resonance frequency distribution for ^{13}C (1st row), ^{1}H slices for anatomical reference (2nd row), and urea images overlaid on ^{1}H images (6th row). Slices are arranged in posterior to anterior direction from left to right. Lactate images are displayed with 2x scaling factor compared to pyruvate. Saturation bands were applied near the heart and below the kidneys in ^{1}H acquisition to minimize flow related artifacts.

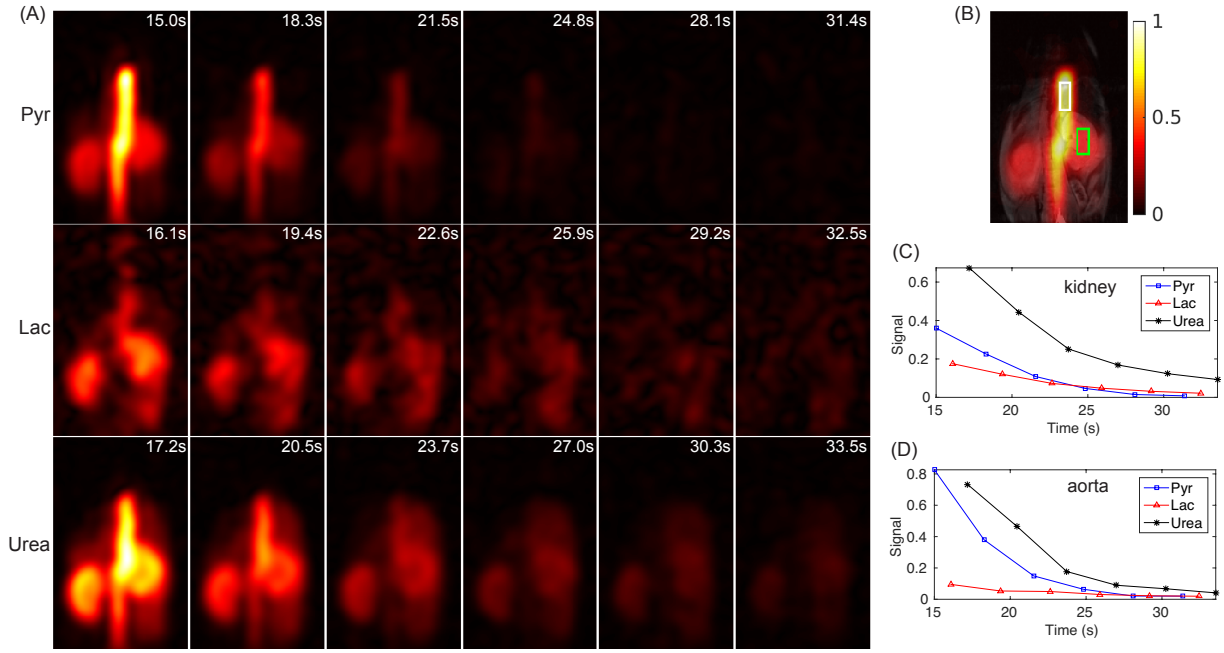

Figure 4.9: Same data as in Figure 4.8 but displaying all time points at one coronal slice containing kidney and aorta (third slice from left in Figure 4.8) (A). Lactate images are displayed with 3x scaling factor compared to pyruvate. The time stamps are relative to starting time of injection and estimated based on average respiratory rate of 55/min, labeled on each image. Pyruvate image at first time point overlaid on ^{1}H image with labeled ROI at kidney (green) and aorta (white) (B). Measured metabolites dynamic curves at kidney (C) and aorta (D).

4.6 Discussion

We have developed and tested a new bSSFP approach for spectrally selective imaging of multiple HP compounds. This sequence inherits the superior SNR efficiency and speed of bSSFP sequence, which is critical for HP ^{13}C studies due to the non-recoverable nature of HP magnetization and the short imaging window determined by T_1 decay. High spatial and/or temporal resolution can be achieved using this bSSFP sequence, since these parameters are fundamentally limited by SNR and speed. The challenge of managing the spectral selectivity of bSSFP sequence was successfully addressed in this work by utilizing novel optimized spectrally selective RF pulse with short duration and carefully chosen TR to avoid excitation banding artifact. This enabled 3D dynamic metabolic imaging in vivo with higher spatiotemporal resolution than prior approaches.

Spectrally selective RF pulses are usually not used in bSSFP due to long pulse durations, which limit the minimum achievable TR. However, the advantage it provides may compensate for this limitation, including improved off-resonance insensitivity, SNR efficiency, and the flexibility of choosing a different flip angle for each compound. A wide passband is achieved in this study (±50Hz) within which uniform spectral selectivity was achieved, as shown in Figure 4.4 (E1,F1). This can be improved further with slightly increased RF pulse duration. It enables separate excitation of individual metabolite with minimal effect on other metabolites, similar as [von Morze *et al.*, 2013; Månsson *et al.*, 2012], which simplifies the reconstruction and shortens the duration of each acquisition, compared to simultaneously exciting all compounds and separating them in reconstruction [Leupold *et al.*, 2009; Morze *et al.*, 2014; Varma *et al.*, 2015]. The total scan time of this method may exceed those methods for simultaneous excitation; however, keeping each individual acquisition short reduces sensitivity to motion, flow, metabolic conversion and relaxation decay.

4.6.1 Choice of flip angle

When HP ^{13}C pyruvate is used as a substrate, it is converted to ^{13}C lactate in vivo, providing metabolic information. But lactate signal is usually much lower and more difficult to observe. A relatively small flip angle on pyruvate can provide sufficient SNR while preserving more magnetization for continued conversion to lactate, thus enabling a longer imaging window [Larson *et al.*, 2008]. A relatively larger flip angle can be applied to lactate to provide higher SNR, as lactate signal is continuously replenished by metabolic conversion from pyruvate [Schulte *et al.*, 2013]. The specific values of flip angles were not optimized in this study. Optimizing these flip angles depends on specific aspects of the application, such as the duration of imaging window, and also knowledge of tissue parameters, such as T_1 and T_2. The choice of flip angle also affects the optimized RF pulse design, which may have different pulse duration, and further affects the choice of optimal TR. A constant flip angle was used for all dynamic time points in this study. A progressively increasing flip angle for subsequent dynamic acquisitions would be likely to extend the imaging window by allocating signal more equally over time [von Morze *et al.*, 2011a].

4.6.2 Spatial and temporal resolution

There are fundamental trade-offs between spectral, spatial and temporal resolution. The spectrally selective bSSFP sequence has the limit of spectral undersampling, as only one compound is imaged at a time. A high temporal resolution is important to capture the metabolite dynamics which provide additional metabolic information besides the spatial distribution of multiple metabolites, such as perfusion and uptake rate of the injected substrates, and the time to maximum signal for metabolic products [Larson *et al.*, 2011]. Our initial implementation with a conventional sinc pulse ($\sim$5ms) requires $\sim$2s per acquisition, within which the HP signal decay, metabolic conversion and respiratory motion will cause image blurring. By using the optimized RF pulse with shorter duration, the acquisition of

each compound takes <1s, which can be fit into one respiratory cycle, thus enabling respiratory triggering and reducing blurring. The temporal resolution of this sequence can be further modified by trading off spatial resolution. However, too fine a temporal resolution is not a good option because it expends the magnetization too rapidly. Although this bSSFP sequence can preserve and recycle transverse magnetization, HP magnetization still decays faster during each bSSFP pulse train because of mixed T_1 and T_2 decay compared to pure T_1 decay when no RF pulse is applied [Scheffler, 2003].

4.6.3 Future work

This method could be extended to other field strengths, like HP ^{13}C studies at 3T for potential clinical application. At lower field, the frequency separation between multiple compounds reduces, which will increase the minimal achievable RF pulse duration, and thus minimal achievable TR. In that case undersampling methods including parallel imaging, compressed sensing and partial Fourier acquisition can be applied for improving temporal resolution, spatial resolution or volumetric coverage [Larson *et al.*, 2011]. Sequential phase encoding is used in the current implementation, and the 3D k-space center is sampled around 0.5s, which is on the order of T_2 values of ^{13}C compounds and could result in suboptimal SNR. Center out encoding could be used to further improve SNR. This method can also be applied to water-fat separation in ^{1}H bSSFP. Previous studies have used spatial-spectral RF pulses [Yuan *et al.*, 2011; Jou *et al.*, 2015] or binomial pulses [Ribot *et al.*, 2015] in bSSFP for water-fat separation. The alternating TR bSSFP approach is essentially equivalent to the use of binomial pulses in bSSFP [Leupold *et al.*, 2006; Çukur, 2015]. The method of choosing TR developed in this work can be applied to improve stopband suppression and reduce requirements on RF pulse design.

4.6.4 Limitations

Though this method is more B_0 robust compared to other HP ^{13}C spectrally selective bSSFP sequences [Leupold *et al.*, 2009; von Morze *et al.*, 2013; Månsson *et al.*, 2012; Morze *et al.*, 2014; Varma *et al.*, 2015], it still requires careful B_0 calibration and shimming. A large B_0 deviation will dislocate both passband and stopband. However this problem occurs in any spectrally selective imaging sequence because either chemical shift or B_0 inhomogeneity contributes to the same off-resonance effect. Such B_0 sensitivity issues will be more likely to cause banding artifacts with larger animals and humans. However, the gyromagnetic ratio of ^{13}C is about 1/4 of ^{1}H and thus the off-resonance frequency distribution is also about 1/4 given the same B_0 inhomogeneity, which reduces the sensitivity to banding artifact to some extent. Another limitation is that without a spatially selective RF pulse, the current implementation excites the whole 3D volume within the sensitive region of the RF coil, and thus this entire volume must be spatially encoded in order to avoid wrap-around artifacts.

4.7 Conclusion

A spectrally selective 3D dynamic bSSFP sequence was developed for HP ^{13}C metabolite imaging with subsecond acquisition time and 2mm isotropic resolution. High spectral selectivity ($\sim$100:1) of the bSSFP sequence was achieved by using short-duration optimized spectrally selective RF pulses and carefully choosing TR to avoid excitation banding artifacts. This sequence is expected to be useful for preclinical HP ^{13}C studies at high field, and holds potential for clinical studies.

Chapter 5

Variable Flip Angle Design for Balanced SSFP Transient Imaging of Hyperpolarized ^{13}C

5.1 Abstract

Balanced SSFP imaging can provide superior SNR efficiency for hyperpolarized ^{13}C imaging by efficiently utilizing the non-recoverable magnetization and exploiting the long relaxation times of ^{13}C nuclei. Since image acquisition occurs in a transient state instead of steady state, a constant flip angle is unnecessary and usually leads to decaying signal with suboptimal SNR. In this work variable flip angle schemes were designed for balanced SSFP transient state hyperpolarized ^{13}C MRI to achieve a uniform signal profile, reduce image blurring and increase SNR. A new optimization approach was developed with improved off-resonance insensitivity. A second analytical approach was also developed as a simpler near-optimal alternative to the proposed optimization approach. Bloch simulations were used to study the signal evolution for off-resonance spins. Hyperpolarized phantom and animal experiments were performed to evaluate the new flip angle schemes compared to constant flip angles. Improved SNR ($\approx 40\%$), observation of small structures and reduced banding artifacts were achieved with our variable flip angle balanced SSFP sequence.

5.2 Introduction

Balanced steady-state free precession (bSSFP) sequences offer high SNR efficiency for rapid 2D and 3D ^{1}H MRI [Oppelt *et al.*, 1986; Scheffler and Lehnhardt, 2003]. They are routinely used for rapid morphological and cardiac imaging [Bieri and Scheffler, 2013]. bSSFP has also been applied to hyperpolarized (HP) ^{13}C imaging [Svensson *et al.*, 2003; von Morze *et al.*, 2011a; Reed *et al.*, 2014], since its higher SNR is desirable to efficiently capture the non-recoverable HP signal. It preserves transverse magnetization between TRs with zero gradient-induced signal dephasing, allowing for continued use of the transverse magnetization (e.g. for multiple phase encoding steps), which is especially valuable for ^{13}C nuclei with long T_2's [Reed *et al.*, 2014; Yen *et al.*, 2010].

Despite having steady-state in the name, in many applications signal acquisition occurs during a transient state. For some ^{1}H MR applications where physiological gating or contrast preparation is used, the transient state is utilized in order to reduce waiting time, while the steady state would only be established after about $5xT_1$ [Bieri and Scheffler, 2013], which is prohibitively long. For HP ^{13}C MRI, the magnetization approaches zero in the steady state, and thus a transient state must be used. This also applies for ^{1}H subtractive imaging [Smith *et al.*, 2010], where the differential magnetization is zero in the steady state. To make use of transient state signals for data collection, a catalyzation preparation scheme is usually applied to reduce signal oscillations and associated artifacts in the transient state. Commonly used catalyzation methods include the $\alpha/2 - TR/2$ pulse scheme [Deimling and Heid, 1994], or appending a few dummy cycles with progressively increased flip angles before image acquisition [Deshpande *et al.*, 2003; Le Roux, 2003; Paul and Hennig, 2004].

A constant flip angle (CFA) is required to maintain a steady state, but is not necessary for transient state imaging. A CFA scheme applied to transient state imaging can result in a rapidly decaying signal profile, causing image blurring and suboptimal SNR. By varying the flip angles, it is possible to achieve a uniform signal profile with higher signal strength,

which would increase SNR and reduce image blurring.

The concept of using variable flip angle (VFA) with spoiled gradient-echo sequences has been well established for HP MR [Zhao *et al.*, 1996; Xing *et al.*, 2013]. The flip angle can be progressively increased to account for losses due to RF excitation [Zhao *et al.*, 1996], T_1 relaxation, metabolic conversion [Xing *et al.*, 2013] and diffusion weighting [Koelsch *et al.*, 2014] in order to maintain a constant signal for each excitation. This VFA design has been integrated in multiple HP ^{13}C imaging sequences, such as echo-planar spectroscopic imaging (EPSI) [Larson *et al.*, 2008], EPI and Spiral CSI [Mayer *et al.*, 2009]. These sequences share one common feature in that the transverse magnetization is dephased at the end of each TR interval even though there may be substantial remaining Mxy for ^{13}C signals with long T_2's. This dephasing reduces sensitivity to off-resonance effects and complexity of VFA design, but also sacrifices SNR efficiency.

VFA schemes have also been developed for bSSFP sequences, though not commonly applied to HP ^{13}C MRI. Previously, VFA schemes have been applied to increase SNR while maintaining power deposition [Smith *et al.*, 2010; Paul and Zaitsev, 2009], and to achieve target signal profile to reduce image blurring [Worters and Hargreaves, 2010; Deppe and Wild, 2012]. Different approaches were used for VFA design, such as empirical trial-and-error [Paul and Zaitsev, 2009], forward calculation given desired echo amplitudes with analytical, closed-form expression [Worters and Hargreaves, 2010; Deppe and Wild, 2012], and numerical optimization of an objective function of the tissues simulated signal [Smith *et al.*, 2010].

In this work we developed a specialized VFA bSSFP approach for HP ^{13}C MRI to increase SNR and reduce image blurring. The analytical approach of VFA design in [Worters and Hargreaves, 2010] was extended for HP ^{13}C MRI. In addition, a new approach of VFA design was developed utilizing non-convex optimization to improve off-resonance insensitivity in order to reduce banding artifacts. Bloch simulations were used to study the signal evolution for off-resonance spins. Three VFA schemes were evaluated with HP ^{13}C phantom and animal studies, including CFA, VFA by analytical approach (VFA-ana), and VFA by optimization

approach (VFA-opt).

5.3 Theory

5.3.1 Signal Formulation

The matrix formulation was used for Bloch equation simulations of bSSFP signal evolution, which was first introduced in [Jaynes, 1955] and applied to bSSFP in [Freeman and Hill, 1971; Hargreaves *et al.*, 2001; Scheffler, 2003; Ganter, 2004]. The evolution of magnetization from one TR to the next can be expressed by

$$\mathbf{M_k} = e^{TE\cdot\mathbf{P}} R_z(-\varphi_k) R_x(\alpha_k) R_z(\varphi_k) e^{TE\cdot\mathbf{P}} \mathbf{M_{k-1}} \tag{5.1}$$

where $\mathbf{M_k} = [M_{xk}, M_{yk}, M_{zk}]^T$ is the magnetization vector of a spin isochromat at echo time ($t = TE = TR/2$) after the k^{th} RF pulse for $k = 1, 2 \ldots n$ where n is the total number of echoes. Note that there is no T_1 recovery term because we assume the thermal equilibrium magnetization can be neglected in HP MRI.

$$\mathbf{P} = \begin{pmatrix} -1/T_2 & \gamma\triangle B_z & 0 \\ -\gamma\triangle B_z & -1/T_2 & 0 \\ 0 & 0 & -1/T_1 \end{pmatrix} \tag{5.2}$$

and $A = e^{TE\cdot\mathbf{P}}$ (matrix exponential) depicts the magnetization evolution during free precession (between echo time and RF pulse), including relaxation and off resonance induced rotation about the z-axis, $\gamma\triangle B_z = 2\pi\triangle f$, where $\triangle f$ is the off-resonance frequency.

$$B = R_z(-\varphi_k) R_x(\alpha_k) R_z(\varphi_k) \tag{5.3}$$

depicts the RF nutation with flip angle α_k and phase φ_k, which is the angle between

excitation B_1 field and the x axis in the rotating frame ($\varphi = 0$ means a pulse along x axis). RF pulses are approximated to be quasi-instantaneous (RF pulse duration = 0). R_z and R_x are rotation matrices:

$$R_z(\varphi) = \begin{pmatrix} \cos\varphi & \sin\varphi & 0 \\ -\sin\varphi & \cos\varphi & 0 \\ 0 & 0 & 1 \end{pmatrix} \tag{5.4}$$

$$R_x(\alpha) = \begin{pmatrix} 1 & 0 & 0 \\ 0 & \cos\alpha & \sin\alpha \\ 0 & -\sin\alpha & \cos\alpha \end{pmatrix} \tag{5.5}$$

For a certain flip angle schemes, such as those presented in Figure 5.1(A), the echo signal can be simulated based on equation 5.1, as shown in Figure 5.1(B). Assuming sequential encoding is used, the signal profile becomes the k-space modulation function, whose Fourier transform is the point spread function, as shown in Figure 5.1(C). Note that the signal profile in Figure 5.1(B) is only for on-resonance spins, and will differ for off-resonance spins. Simulations with off-resonance frequencies are shown for each flip angle scheme individually in Figure 5.1(D,E,F). Off-resonance can arise from main field inhomogeneity, variation in magnetic susceptibility, and chemical shift. Single HP compounds that do not undergo metabolic conversion were used in this work, eliminating chemical shift as a potential source of off-resonance.

5.3.2 VFA Design by Analytical Approach

As first introduced in [Worters and Hargreaves, 2010], the forward calculation of flip angles based on the desired echo train signal can be solved analytically. An iterative approach can also be used to optimize the signal integral. A similar method has been developed for HP noble gas MRI [Deppe and Wild, 2012]. While it uses the same HP signal formulation, the

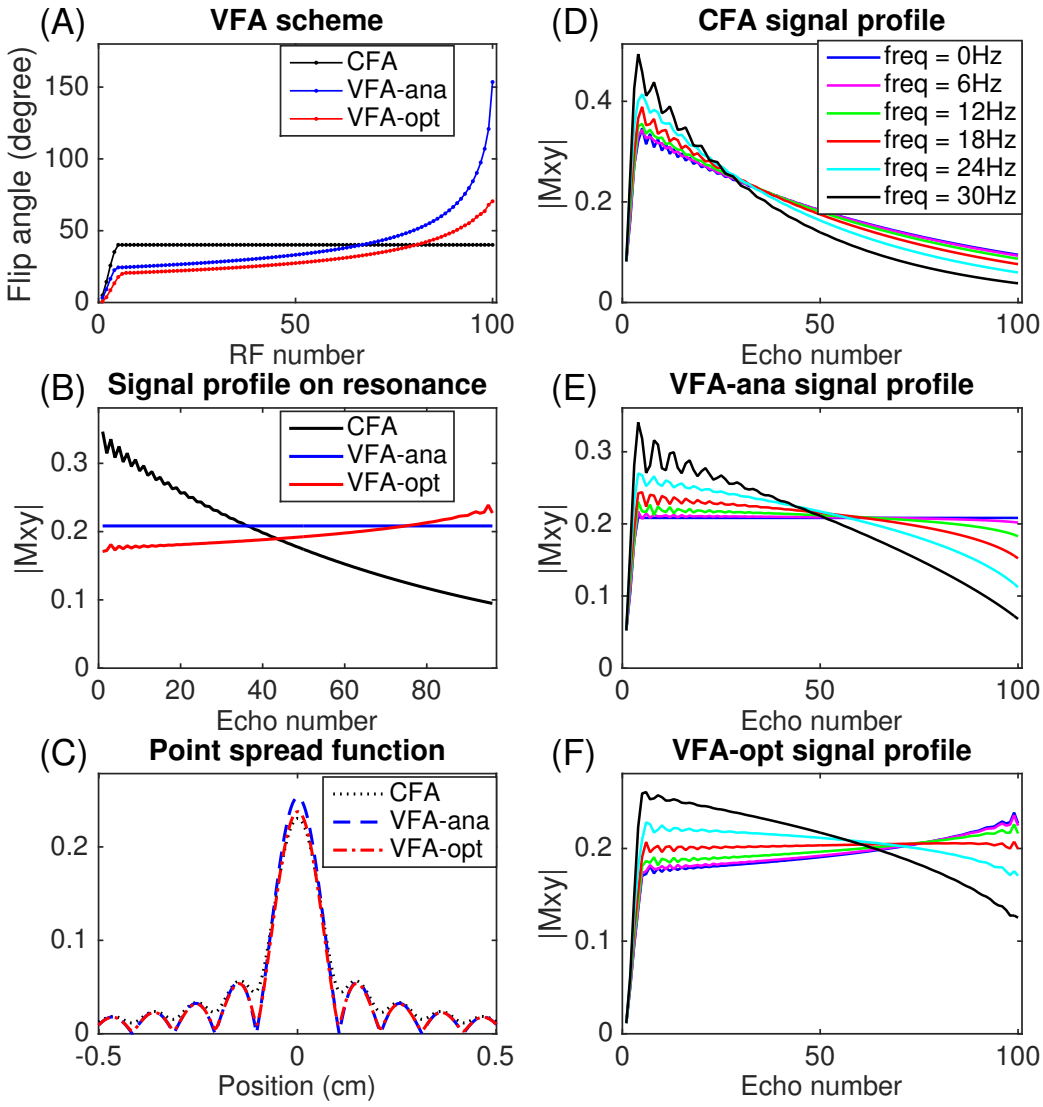

Figure 5.1: Example of three flip angle schemes (A), including constant flip angle (CFA), VFA by analytical approach (VFA-ana), and VFA by optimization approach (VFA-opt). Simulated transverse magnetization at each echo time (TE=TR/2) for on-resonance spins (B), and its corresponding point spread function for sequential phase encoding (C). Signal evolution variations for off-resonance spins is shown for CFA (D), VFA-ana (E), and VFA-opt (F). Design parameters include: TR = 9ms, number of echo = 96, T_1 = 47.5s, T_2 = 81ms.

method in [Deppe and Wild, 2012] was not adopted here because it does not optimize signal level iteratively, and is limited to the $\alpha/2 - TR/2$ preparation pulse. Instead, the analytical approach in [Worters and Hargreaves, 2010] was extended to HP MRI in this work, with the iterative approach for full usage of magnetization and integration with ramp-up preparation pulses. The main difference is removing the T_1 recovery term in the Bloch equation. For completeness, this design process was also covered here. More details can be referred to [Worters and Hargreaves, 2010].

5.3.2.1 Reverse Bloch Equation

Considering only on-resonance spins, equation 5.1 can be simplified as

$$R_x(-\alpha_k)\begin{pmatrix} E_2^{-1} & 0 & 0 \\ 0 & E_2^{-1} & 0 \\ 0 & 0 & E_1^{-1} \end{pmatrix}\begin{pmatrix} 0 \\ M_{y,k} \\ M_{z,k} \end{pmatrix} = \begin{pmatrix} E_2 & 0 & 0 \\ 0 & E_2 & 0 \\ 0 & 0 & E_1 \end{pmatrix}\begin{pmatrix} 0 \\ M_{y,k-1} \\ M_{z,k-1} \end{pmatrix}$$

where $E_1 = e^{-TE/T1}$ and $E_2 = e^{-TE/T2}$. This matrix form equation leads to two equations.

$$\cos(\alpha_k)E_2^{-1}M_{y,k} - \sin(\alpha_k)E_1^{-1}M_{z,k} = E_2 M_{y,k-1} \tag{5.6}$$

$$\sin(\alpha_k)E_2^{-1}M_{y,k} + \cos(\alpha_k)E_1^{-1}M_{z,k} = E_1 M_{z,k-1} \tag{5.7}$$

If α_k, $M_{z,k-1}$ are the variables, they can be solved by equation 5.6 and equation 5.7, given $M_{y,k}$, $M_{y,k-1}$, $M_{z,k}$, TR, T_1, T_2.

Define $\sin(\beta) = \frac{E_2^{-1}M_{y,k}}{((E_2^{-1}M_{y,k})^2+(E_1^{-1}M_{z,k})^2)^{1/2}}$,
$\cos(\beta) = \frac{E_1^{-1}M_{z,k}}{((E_2^{-1}M_{y,k})^2+(E_1^{-1}M_{z,k})^2)^{1/2}}$,

equation 5.6 becomes

$$\sin(\beta - \alpha_k) = \frac{E_2 M_{y,k-1}}{((E_2^{-1} M_{y,k})^2 + (E_1^{-1} M_{z,k})^2)^{1/2}}$$

The flip angle α_k is calculated by

$$\alpha_k = arcsin(\frac{E_2^{-1} M_{y,k}}{((E_2^{-1} M_{y,k})^2 + (E_1^{-1} M_{z,k})^2)^{1/2}}) - arcsin(\frac{E_2 M_{y,k-1}}{((E_2^{-1} M_{y,k})^2 + (E_1^{-1} M_{z,k})^2)^{1/2}}) \quad (5.8)$$

Once α_k is known, $M_{z,k-1}$ can be calculated as

$$M_{z,k-1} = \sin(\alpha_k)(E_1 E_2)^{-1} M_{y,k} + \cos(\alpha_k) E_1^{-2} M_{z,k} \quad (5.9)$$

If we specify no longitudinal magnetization at the end ($M_{z,n} = 0$) and the value of transverse magnetization at each echo time, the flip angles can be calculated from the last RF pulse backwards to the first RF pulse based on equation 5.8 and equation 5.9. When calculating the first flip angle given $M_{y,1}$, $M_{y,0} = 0$, and $M_{z,1}$, $M_{z,0}$ may not equal to the predefined $M_z(t = 0) = 1$. In this work, we focus on HP ^{13}C applications where the initial magnetization can take any arbitrary value. However, when applied to ^{1}H MRI, the initial magnetization cannot be arbitrarily scaled, therefore a bisection search can be used to solve the problem.

5.3.2.2 Integrate preparation pulse

Preparation pulses are widely used in bSSFP sequences to stabilize the transient state signal by manipulating the magnetization to the appropriate direction for all passband resonant frequencies simultaneously. The $\alpha/2 - TR/2$ preparation pulse [Deimling and Heid, 1994] is only effective for a narrow spectral band around on-resonance spins. Ramp-up preparation pulse schemes are simple, B_1 insensitive, and widely used [Deshpande *et al.*, 2003; Le Roux,

2003; Paul and Hennig, 2004]. They are able to reduce transient state oscillation for a larger range of off-resonance frequencies. A major limitation of the analytical VFA design is that it only applies to on-resonance spins. To mitigate this limitation, we show that the use of ramp up preparation pulses build some signal stability for off-resonance spins.

To design a ramp up preparation pulse, we specify the last flip angle, α, and the shape of the ramp from 0 to α. For CFA bSSFP, α is simply the flip angle of each RF pulse in the acquisition. When combined with VFA bSSFP, care must be taken to determine α. The result of analytical VFA design usually has the first flip angle α_1 close to half of the second, which is similar to the $\alpha/2 - TR/2$ pulse, but it is TR instead of TR/2 ahead. α can be set as the second flip angle, α_2 (or $2\alpha_1$). In order to maintain the predefined signal profile for on-resonance spins after adding the preparation pulse, we recalculate the first pulse in the VFA scheme to compensate for the accumulated effect of preparation pulses on on-resonance spins. Different ramp up shapes have been proposed [Deshpande *et al.*, 2003; Le Roux, 2003; Paul and Hennig, 2004]. The Kaiser-windowed preparation pulse is used, which has been shown to provide near optimal results for a wide parameter range [Le Roux, 2003]. We found it to be similar to other ramp up shapes in terms of stabilization performance, based on simulation results.

5.3.2.3 Practical Considerations

The analytical approach assumes that certain parameters are known, such as T_1, T_2, B_1, and resonance frequency (perfect on-resonance condition). However, in practice all of these parameters vary among different tissues, and thus the signal profile will no longer have the predefined shape, as indicated by Figure 5.2. Notably, the transient response is relatively insensitive to T_1, which is consistent with results in Fig. 3 and Fig. 4 in reference [Worters and Hargreaves, 2010]. Varying T_2 or B_1 usually leads to smoothly decaying or increasing signal curves. The off-resonance effect may cause both signal oscillation and signal decay, and the former will likely be more problematic in terms of generating image artifacts. Such

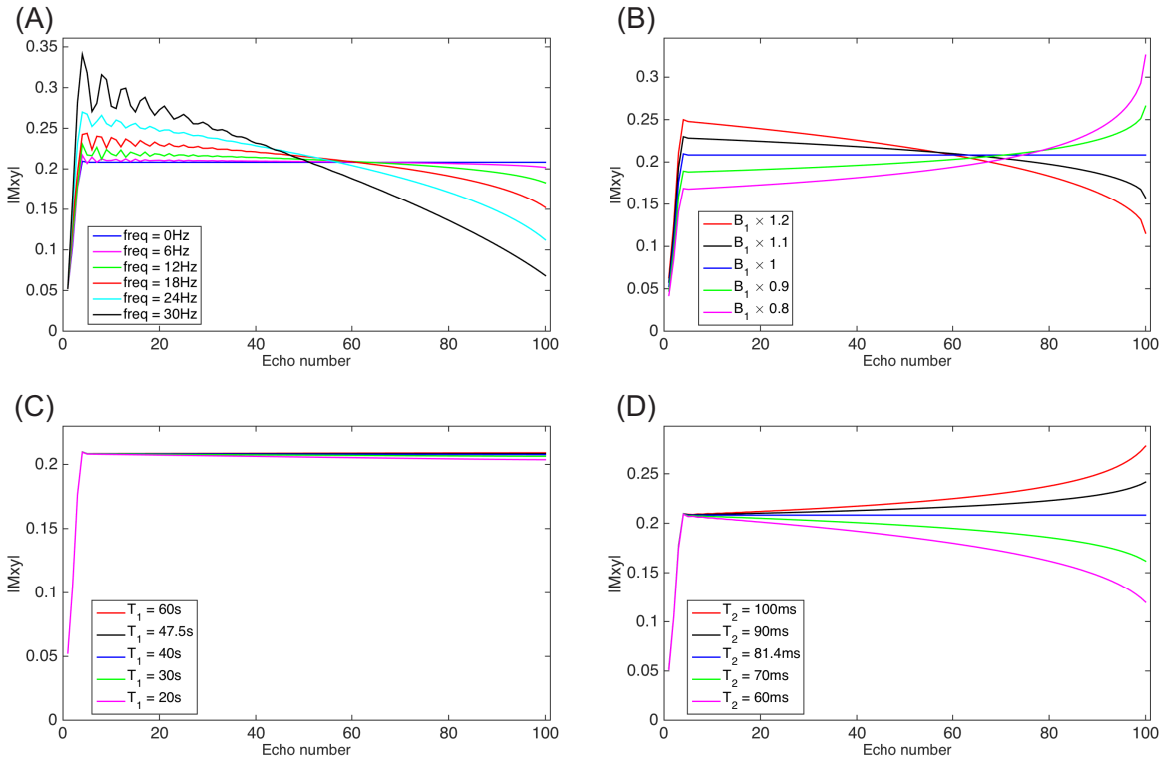

Figure 5.2: For VFA design by the analytical approach (VFA-ana in Figure 5.1(A)), Bloch simulation of echo signal with parameter deviations, including off-resonance frequency (A), B_1 field transmit gain (B), T_1 (C), T_2 (D).

signal oscillation also occurs in CFA bSSFP if the preparation pulse is not applied properly [Hargreaves *et al.*, 2001; Ganter, 2004].

5.3.3 VFA Design by Optimization Approach

To overcome the sensitivity to off-resonance effects, a new VFA design method is proposed to improve off-resonance robustness by targeting the desired signal profile over a range of off-resonance frequencies. As comparison, the analytical approach is designed for on-resonance spins only. In that case, the number of equations for predefined echo amplitudes equals the number of variables of flip angles. However, when extending the desired signal profile

over multiple frequencies, the problem becomes over-determined and can no longer be solved analytically. Therefore, an optimization approach was developed to attempt to achieve a predefined signal profile over a range of frequencies with flip angle and RF phase as the optimization variables. A uniform signal profile was defined to aim to reduce image blurring.

We sampled the continuous off-resonance frequency space to make a finite number of constraints, similarly to finite impulse response filter design. The frequency was sampled at $-\frac{BW}{2} \leq f_1 \leq f_2 \ldots f_m \leq \frac{BW}{2}$ (where BW is the predefined passband bandwidth), and signal profiles were evaluated only at those discrete frequencies.

The cost function is defined as

$$f(\alpha, \varphi) = \sum_{j=1}^{m} (\sum_{k=k_0}^{n} (|M_{xy,k}(\alpha, \varphi, f_j)| - M_{d,k})^{p1})^{p2/p1} \tag{5.10}$$

where $M_{xy,k}$ is the transverse magnetization at the k^{th} echo, as a function of RF pulse flip angles α_i, and phases φ_i, $i = 1, 2 \ldots k$, and off-resonance frequency f_j. $M_{d,k}$ is the desired signal at the k^{th} echo. The cost function is essentially a norm of residual error with two levels, first a norm-p1 of error over time (p1 is an even number), and then norm-p2 across each frequency. Notice that the signal is a complex number, and both magnitude and phase are required to meet predefined profile, however only magnitude is specified in the cost function. The detail of why phase does not have to be specified will be discussed later.

The cost function in equation 5.10 is differentiable, and allows approximating either a least-squares measure, or an equal ripple measure. The equal ripple measure, also called the Chebyshev error or mini-max error [Burrus and UniqU,], is often used to minimize worst case possibilities, while the least-squares measure minimizes the overall error. The ℓ_∞ norm is not differentiable, but can be approximated by minimizing the norm p of error when p is large. The least-squares measure is simply choosing p1=2, p2=2. The details of how to determine these hyperparameters can be found in Appendix B.

If k starts from $k_0 \geq 2$, the RF pulses before k_0 are equivalent to a preparation pulse. In

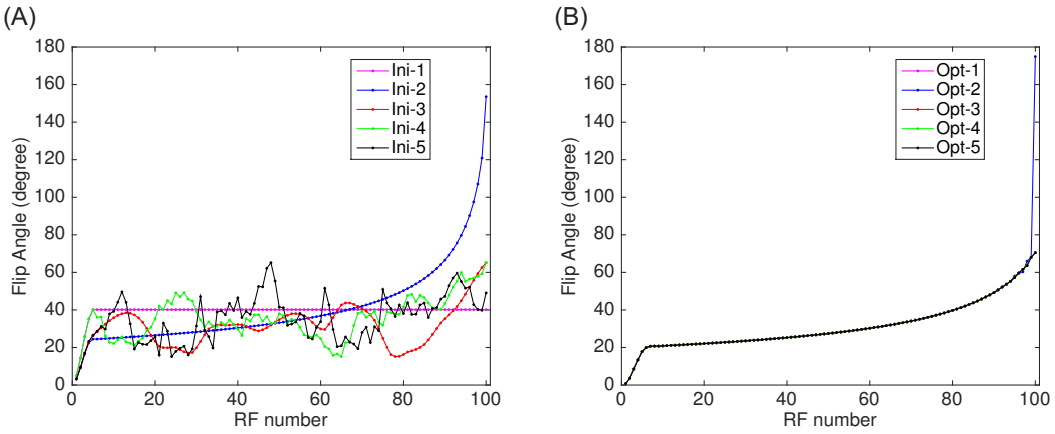

Figure 5.3: Local optimal solutions (B) of VFA design given different initial guess (A). Initial guess 1 (Ini-1) has constant flip angle of 40°; Ini-2 used the VFA by analytical approach; Ini-3 to Ini-5 are some random VFA schemes. Optimal results 1,3,4,5 are very close and overlap with each other, while Opt-2 has different flip angles at the end, indicating that some solutions are locally optimal. Design parameters include: TR = 9ms, number of echo = 96, T_1 = 47.5s, T_2 = 81ms, number of preparation pulse = 4, passband bandwidth = 60Hz.

this way, the preparation pulse is optimized together with the acquisition pulse flip angles, without adding too much computation cost.

This is a non-convex problem and the optimization result may therefore reflect a local optimal solution instead of a global optimal solution [Boyd and Vandenberghe, 2004]. A different initial guess of optimization variables may lead to a different local optimum. We used an unconstrained nonlinear programming solver (fminunc) in MATLAB (Mathworks, Inc, South Natick, MA) to perform the optimization with trust-region algorithm [Nocedal and Wright, 2006] on a 2.4-GHz CPU with four cores (the same computer architecture was also used for VFA generation with analytical approach). Several different initial variables were tested and the corresponding optimal VFA results are shown in Figure 5.3, including constant initial flip angles (Ini-1), a VFA by analytical approach (Ini-2), and three random VFAs (Ini-3, Ini-4, Ini-5). An alternating RF phase is specified for all these five initializations. Surprisingly, most initial points we tested lead to the same local optimal solution,

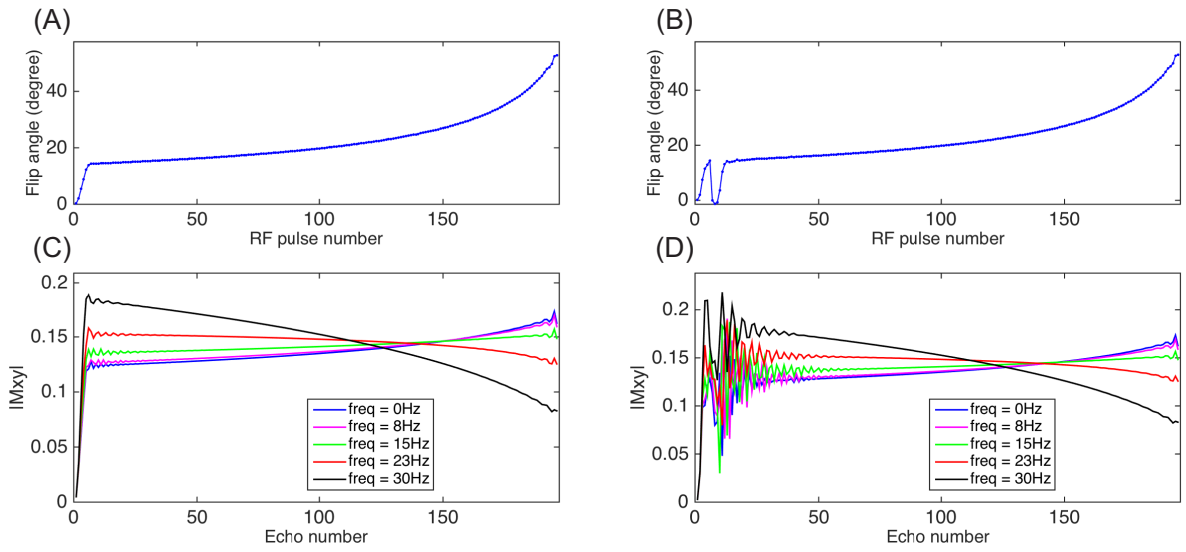

Figure 5.4: Local optimal results of VFA design with analytic gradient (A, C), and approximated gradient (B, D). Simulation of signal profile at a few off-resonance frequencies shown in (C, D). Computation time is 163s (A) and 439s (B) respectively. Design parameters include TR = 9ms, number of echoes = 192, T_1 = 47.5s, T_2 = 81ms, number of preparation pulse = 4, passband bandwidth = 60Hz.

which is likely to be the global optimal solution. Only Ini-2 corresponds to a local optimal solution with a jump at the end, which causes higher RF peak amplitude and potential signal oscillation. Therefore we chose the constant flip angle as the initial guess for our designs.

The optimization problem can be efficiently solved by deriving gradient values, compared to approximating the gradient with finite differences. The details of deriving the gradient can be found in Appendix A. The optimization VFA design shown in Figure 5.1 takes about 36.1s / 127.8s to compute with / without the analytic gradient, and both converge to the same result. However, if the number of variables is higher, like n=192, the optimization without derived gradient may fail, as shown in Figure 5.4(B), probably due to approximation error of the gradient when using finite differences.

5.4 Methods

5.4.1 Bloch Simulation

Bloch simulation of bSSFP signals was used to evaluate different flip angle schemes. The parameters for VFA design, such a T_1, T_2, TR, and number of echoes are consistent with the HP [^{13}C]urea phantom study presented later, so that the simulation results could be compared to the measured HP phantom results.

Signal at echo time was simulated based on equation 5.1, with a range of off-resonance frequency, $[-\frac{1}{2TR}, \frac{3}{2TR}]$, which is two periodic cycles of the bSSFP frequency response.

Signal evolution between two RF pulses was also simulated with a similar equation as 5.1, but with a finer sampling rate. As first introduced in [Scheffler and Hennig, 2003], bSSFP has a refocusing property similar to a spin echo sequence. The refocusing property for transient state bSSFP with VFA was studied qualitatively with this simulation.

5.4.2 Hardware

MR experiments were performed on a 3T clinical MRI scanner (GE Healthcare, Waukesha, WI, USA). A dual-tuned rat birdcage coil was used for radiofrequency excitation and signal reception. The radiofrequency transmit gain was calibrated with a ^{13}C-enriched urea phantom with similar size and location as the HP phantom. Varying flip angles were achieved by scaling the amplitude of RF pulses. Dissolution DNP was performed with a HyperSense polarizer (Oxford Instruments, Oxford, UK) operating at 1.3 K and 3.35 T.

5.4.3 Phantom Measurements

HP [^{13}C]urea phantom experiments were performed to measure the VFA bSSFP transient state signal and to verify the simulation results. The transient state signal profile as a function of both time and off-resonance frequency was measured using a bSSFP sequence

with phase encoding turned off. A small constant gradient field was applied to create a distribution of off-resonance frequencies along the readout direction.

Three flip angle schemes were evaluated, including CFA, VFA-ana, and VFA-opt, as shown in Figure 5.1(A). Parameters for VFA design include T_1 = 45s, T_2 = 81ms, TR = 9ms, number of echoes = 96, number of preparation pulses = 4. Constant flip angle was specified as 40° for maximum integral of signal. For VFA-opt, the passband was specified as 60Hz. The T_1 of HP urea in aqueous solution was measured to be approximately 45s with a small flip angle (5°) spoiled gradient echo sequence (TR = 2s, number of scans = 64). T_2 was measured to be 81.9 ± 0.8ms with a CPMG sequence with phase encoding turned off (TR = 10ms, number of echoes = 200).

To compare the performance of different VFA schemes, all other experimental details were kept the same, such as amount of HP sample, duration of polarization buildup, and sample transfer time. HP urea samples were transported to the scanner with an electromagnet carrier to avoid signal loss at low field and to increase consistency [Shang *et al.*, 2015]. Sequence parameters included: TR = 9ms, TE = 4.5ms, FOV = 100mm, spatial resolution = 0.77 mm, readout bandwidth = 25kHz, additional constant gradient = 0.065 G/cm. A windowed sinc excitation RF pulse was used, with duration = 0.8ms, time-bandwidth-product = 4.

With the same experimental setup, but phase encoding turned on, 2D bSSFP images of the HP urea phantom were acquired (projection along the third direction). Sequence parameters included: matrix size = 110x96, TR = 9ms, TE = 4.5ms, FOV = 110x55mm, readout bandwidth = 27.8kHz, additional constant gradient = 0.052 G/cm, and the same RF pulse as above.

5.4.4 In vivo Experiments

5.4.4.1 2D bSSFP

In vivo HP [^{13}C]urea 2D bSSFP MRI was performed using normal rats following a protocol approved by UCSF Institutional Animal Care and Use Committee. Coronal images with a projection along the anterior-posterior direction were acquired. The bSSFP sequence with CFA has been applied for HP ^{13}C perfusion imaging and angiography [Reed *et al.*, 2014]. A 2.5 mL 125 mM solution was injected into the rat tail vein catheter over 12 s with image acquisition starting at 25 s after the beginning of the injection. Experiments were repeated on three rats. For each rat, the three flip angle schemes were evaluated, while keeping all the other parameters the same.

The measured results of T_1/T_2 = 45s/280ms in rat aorta from [Reed *et al.*, 2014] were used in the design of VFA, although T_1 and T_2 of HP urea varies for different tissues in vivo. The constant flip angle was specified as 79° for maximum integral of signal, as demonstrated in [Reed *et al.*, 2014]. Sequence parameters included: matrix size = 192x96, number of echoes = 96, number of preparation pulse = 5, TR = 9ms, TE = 4.5ms, FOV = 180x90mm, readout bandwidth = 41.7kHz, sequential phase encoding, windowed sinc RF pulse duration = 1.6ms, time-bandwidth-product = 4.

5.4.4.2 3D bSSFP

Another HP [1-^{13}C]lactate rat experiment was performed with a 3D bSSFP sequence. Since little metabolic product ($\approx 1\%$) is generated as compared to the amount of injected lactate, this can be potentially applied for lactate uptake mapping [von Morze *et al.*, 2014]. A 2.5 mL 160 mM solution of HP lactate was injected in the same way as above, with image acquisition starting at 25 s. T_1/T_2 of HP lactate was estimated as 45s/2.15s from [Milshteyn *et al.*, 2015]. The experiments were repeated twice, one with CFA (110° for maximum signal integral), the other with VFA-ana. VFA-opt was not used due to long computation time at

higher dimensions (n=480). Sequence parameters included: matrix size = 80x40x12, 1.5mm isotropic resolution, number of echoes = 480, number of preparation pulse = 7, TR = 9ms, TE = 4.5ms, readout bandwidth = 31.3 kHz, sequential phase encoding ordering, windowed sinc RF pulse duration = 1.6ms, time-bandwidth-product = 4.

5.4.4.3 B_0 map

The B_0 map was measured from proton signal and then converted to the off resonance frequency distribution of ^{13}C in vivo. A SPGR sequence was used, repeated at two echo times (4.3ms and 6.3ms), and the phase difference of the two acquisitions was used to calculate off resonance frequency. FSL, a library of analysis tools for MRI, was used for 2D phase unwrapping [Jenkinson *et al.*, 2012].

5.5 Results

5.5.1 VFA Design and Simulation

Two VFA schemes were designed, one with the analytical approach (VFA-ana), the other with the optimization approach (VFA-opt), as shown in Figure 5.1(A) together with a constant flip angle scheme (CFA). Simulation of on-resonance signals is shown in Figure 5.1(B) and its point spread function for sequential phase encoding in Figure 5.1(C). The signal profiles for off-resonance spins were simulated at a few frequencies as in Figure 5.1 (0-30Hz, D,E,F), and also with a finer sampling in a range of two cycles as in Figure 5.5. For on-resonance spins, VFA-ana demonstrated the best performance with completely flat signal and higher signal integral (as indicated by peak height in point spread function), while VFA-opt showed a slightly increasing signal profile and lower total signal. However for off-resonance spins, VFA-opt outperformed VFA-ana with a more uniform signal profile and smaller oscillations. Above all, both VFA designs outperformed CFA in terms of signal flatness, total

signal strength and off-resonance insensitivity.

From Figure 5.5(B, D, F), it is observed that the magnetization phase profile is uniform for either CFA or VFA, with opposite sign for two consecutive cycles, which matches the behavior of bSSFP with CFA [Hargreaves *et al.*, 2003].

The simulation of signal evolution between RF pulses was performed (results not shown here) and demonstrated that the refocusing property still exists for transient state bSSFP with VFA, when flip angles change slowly and an alternating phase is used. This refocusing property keeps the central passband insensitive to off-resonance. This is why only magnetization magnitude is specified in the cost function, but the result has a uniform phase profile as well.

5.5.2 Phantom Measurement

The measured bSSFP transient state signal profiles with the three flip angle schemes are shown in Figure 5.6(A-F), which match well with Bloch simulation results in Figure 5.5. Note that the cycle on the right is slightly compressed due to additional off-resonance. The signal profiles at a few locations are shown in Figure 5.6(G, H, I), which match well with the simulation results in Figure 5.1(D,E,F).

2D bSSFP images of the HP urea phantom are shown in Figure 5.7. A few line profiles are drawn vertically (readout direction, additional gradient direction), and horizontally (phase encoding direction). Images acquired with VFA-opt had a broader and more uniform passband (Figure 5.7(D)). Images acquired with VFA-ana had higher signal in the center (on-resonance location) (Figure 5.7 (E)), but decreased quicker for off-resonance locations compared to VFA-opt (Figure 5.7(G)).

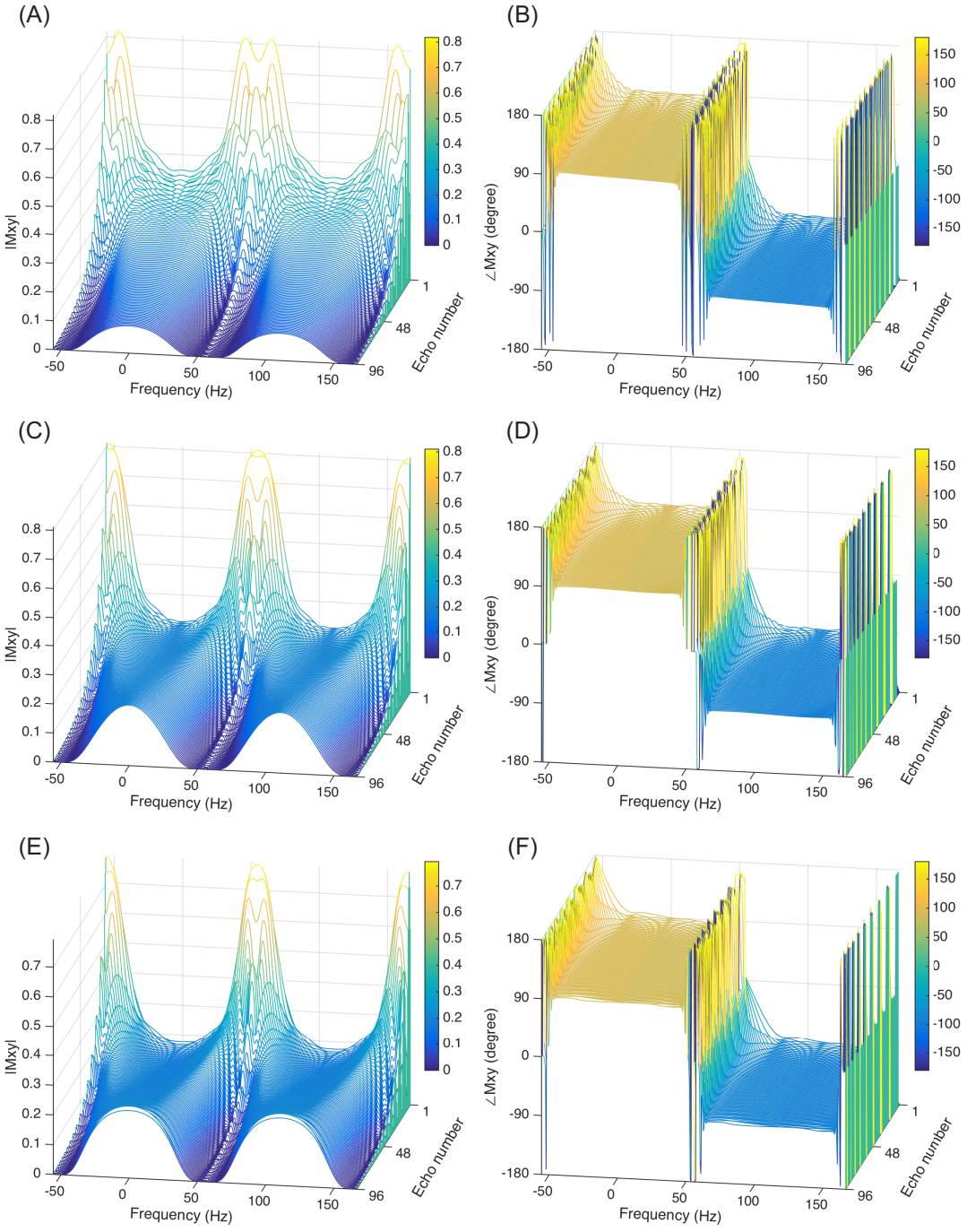

Figure 5.5: Bloch simulation of echo signal over n=96 echoes and off-resonance frequency within $[-\frac{1}{2 \cdot TR}, \frac{3}{2 \cdot TR}]$ for CFA (A,B), VFA-ana (C,D), and VFA-opt (E,F). Magnetization magnitude is shown in (A, C, E), while phase is shown in (B, D, F).

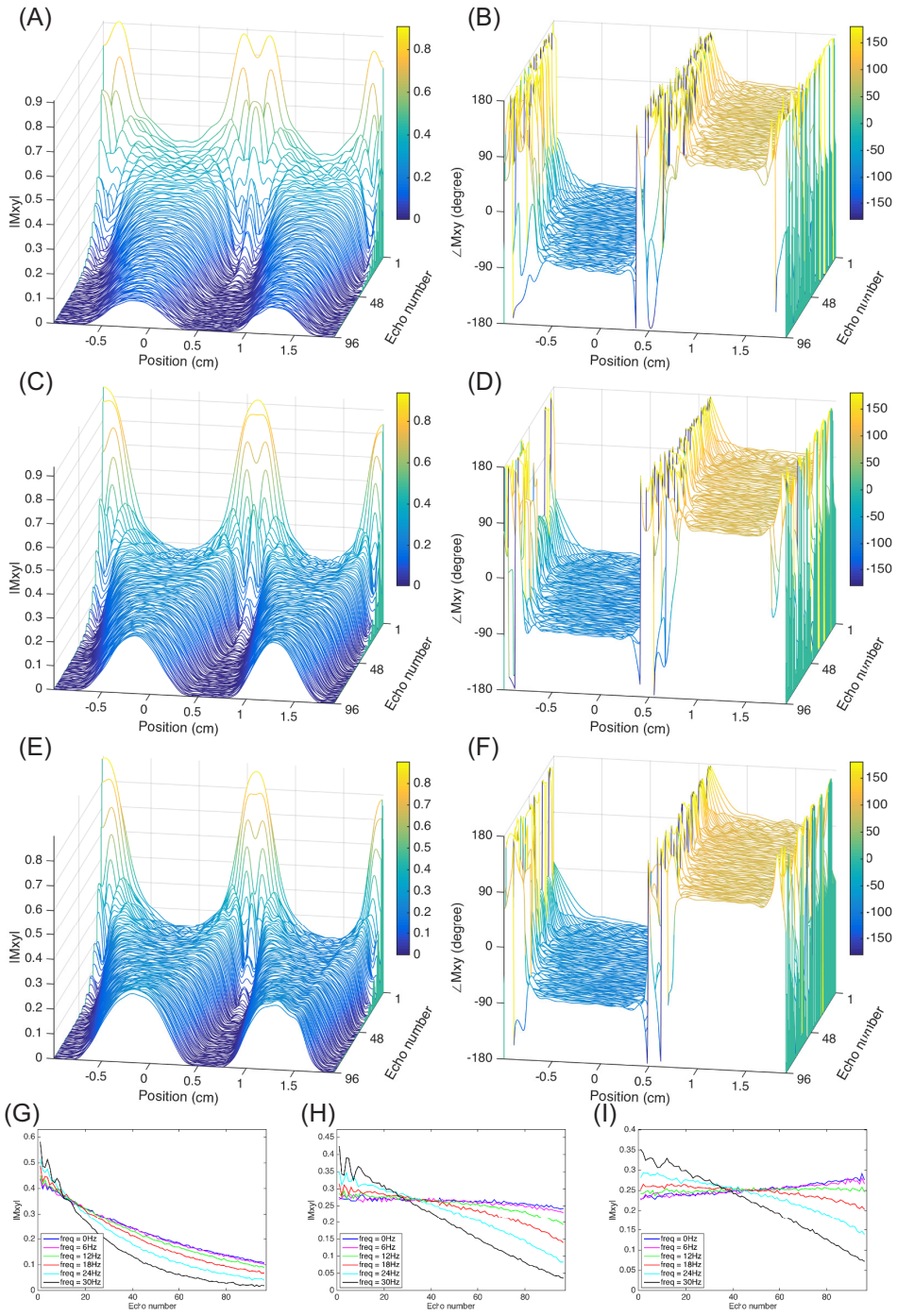

Figure 5.6: bSSFP transient state signal profile measurements with HP urea phantom. An additional constant gradient (0.065 G/cm) was applied to generate off-resonance along readout direction. Signal profile over two bSSFP frequency response cycles with CFA (A, B), VFA-ana (C, D), and VFA-opt (E, F), corresponding to the simulation results in Figure 5.5 (A-F) respectively. Signal profiles at a few off-resonance locations for CFA (G), VFA-ana (H), and VFA-opt (I), corresponding to simulation results in Figure 5.1 (D, E, F) respectively.

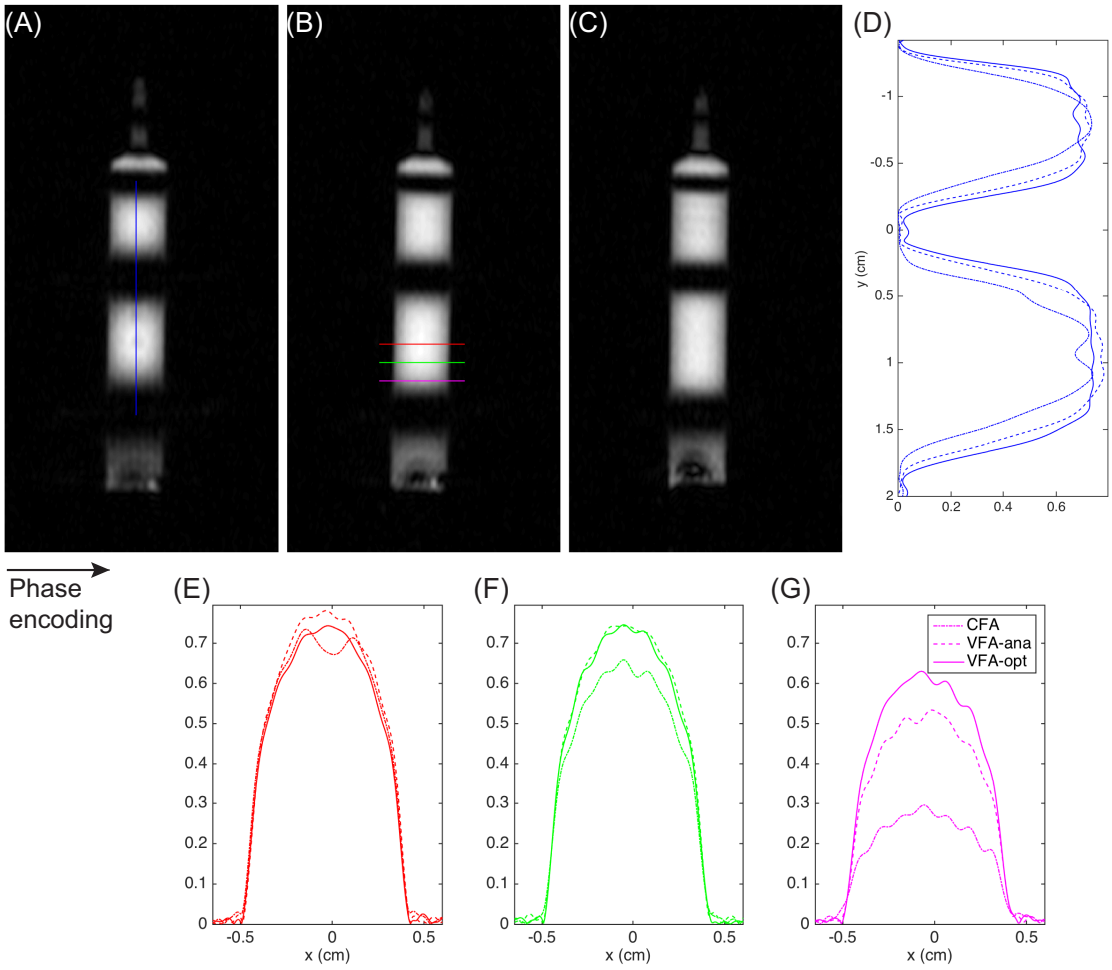

Figure 5.7: HP [^{13}C]urea 2D bSSFP phantom images with CFA (A), VFA-ana (B), and VFA-opt (C). A 1D vertical profile (D) and three horizontal profiles (E, F, G) are marked with the same color in (A) and (B).

5.5.3 In vivo Acquisition

HP ^{13}C urea 2D bSSFP in vivo results are shown in Figure 5.8 with CFA (B), VFA-ana (C) and VFA-opt (D), together with one coronal slice of anatomic bSSFP proton images (A). SNR measured in the aorta with three repetitions showed 1.32 $\pm$ 0.08 and 1.4 $\pm$ 0.1 fold SNR improvement with VFA-ana and VFA-opt respectively, compared to CFA. Note that one horizontal vessel can be seen clearly in (D) with VFA-opt, but was not observed in (C) with VFA-ana. Also note that the boundary between kidney and liver was clearest with VFA-opt, compared to the other two.

HP ^{13}C lactate 3D bSSFP in vivo results are shown in Figure 5.9, together with one coronal proton imaging slice for anatomical reference (A), which corresponds to the HP ^{13}C coronal slice in the orange box, and a measured distribution of off-resonance frequency (B). Some detailed structures are shown more clearly in (D) with VFA. The measured off-resonance frequency map demonstrated the predefined passband of 60Hz used in VFA design should cover most of the rat torso where the HP signal was concentrated.

5.6 Discussion

5.6.1 Image Performance with VFA

In HP ^{13}C phantom and animal experiments we demonstrated reduced image blurring (improved detection of small structures), improved SNR and improved off-resonance insensitivity with the new VFA scheme. Each of these three characteristics will be discussed in detail below. Image blurring is reduced due to the uniform k-space modulation function, which is demonstrated in the 2D bSSFP phantom study (Figure 5.7), where the edge along the phase encoding direction is sharper with VFA schemes compared to CFA. In the 2D and 3D bSSFP in vivo studies, some small structures can only be detected with VFA, as shown in Figure 5.8 and Figure 5.9.

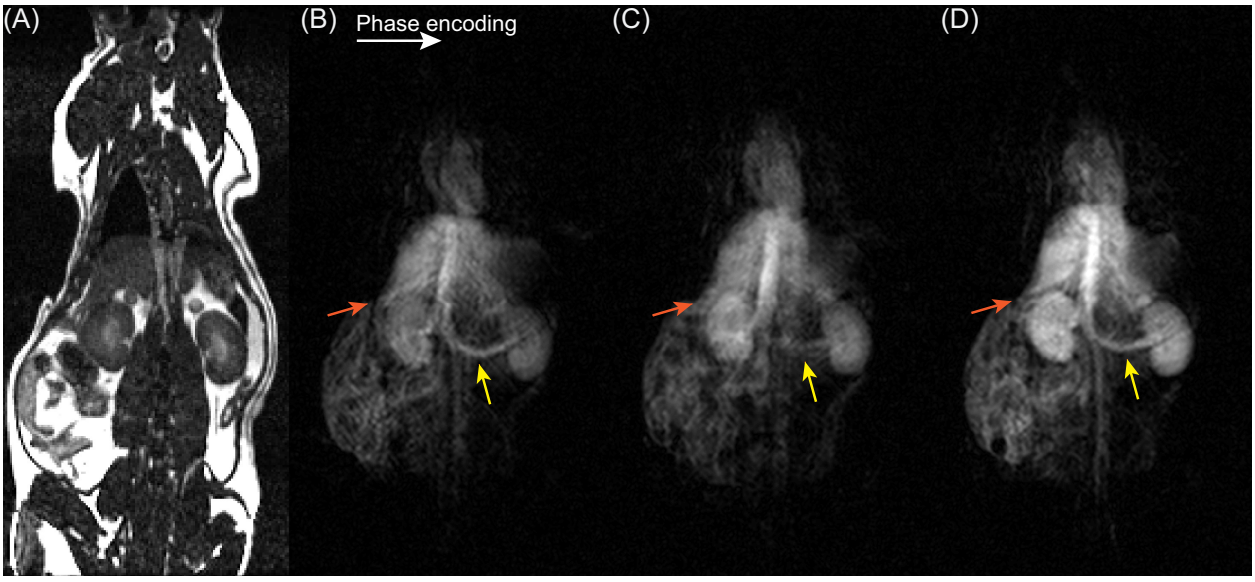

Figure 5.8: HP [^{13}C]urea 2D bSSFP in vivo images with CFA (B), VFA-ana (C) and VFA-opt (D) (displayed with the same window). A coronal ^{1}H anatomical reference image (A). Notice the improved observation of boundary between kidney and liver (orange arrow) in (D). SNR measured in the aorta was 113 (B), 140 (C), and 163 (D).

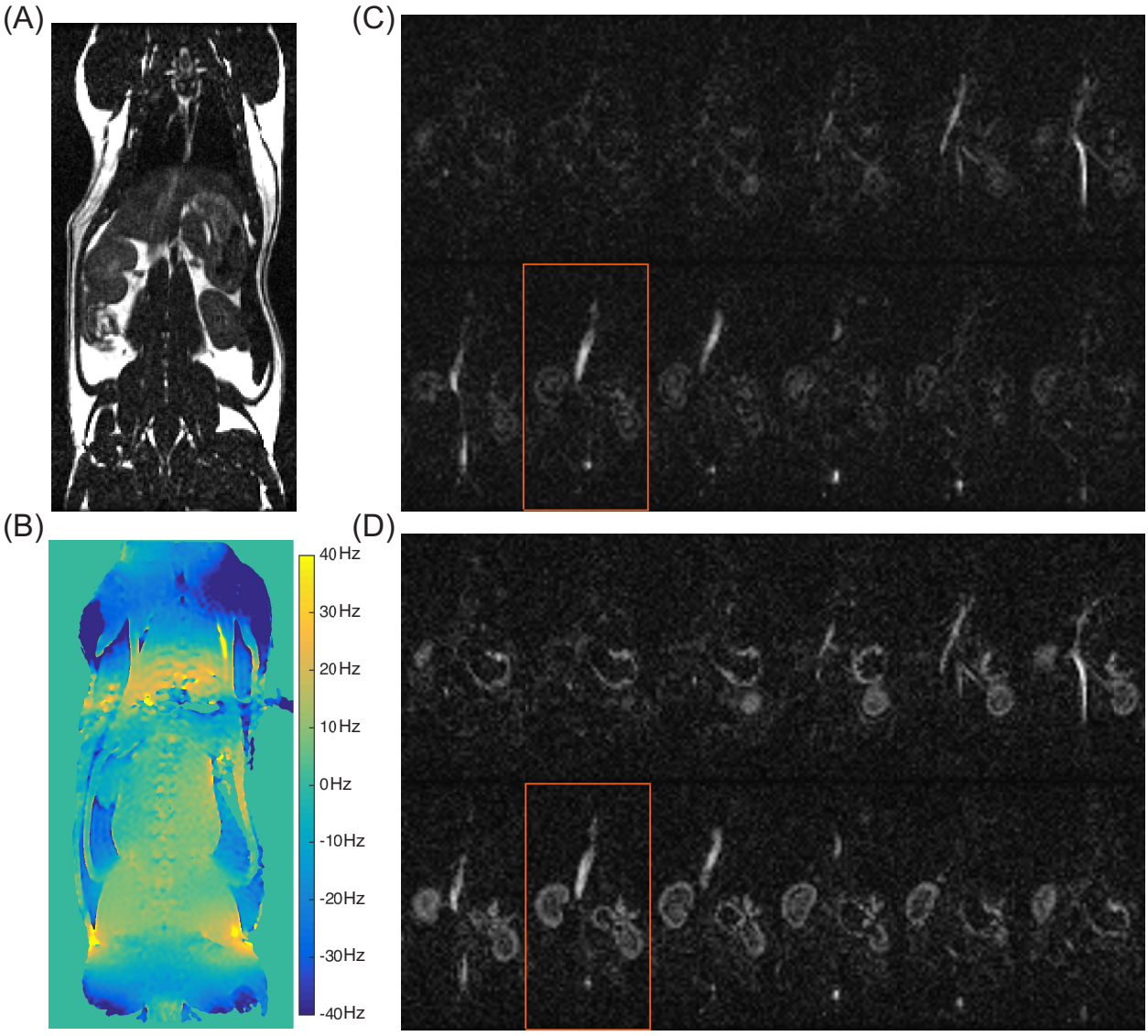

Figure 5.9: HP ^{13}C-lactate 3D bSSFP in vivo images. All 12 coronal slices are displayed together for CFA (C), and VFA-ana (D). A coronal slice of ^{1}H anatomical imaging (A) which corresponds to the HP ^{13}C coronal slice in the orange box. Measured off-resonance map for ^{13}C with unit of Hz (B).

Image SNR can be estimated by the height of point spread function (PSF), FT of the k-space modulation function. However, since the actual image is not a point and usually has much higher signal at k-space center, a higher signal level at k-space center is typically desired to increase SNR. A uniform k-space modulation function was used in this study to reduce blurring but it may not be SNR optimal. However, both PSF height and k-space center value with VFA are still higher than what can be achieved by CFA. A more in-depth study of trade-offs between SNR and spatial resolution with non-sequential phase encoding ordering is planned for future work.

VFA design using the optimization approach was more B_0 robust than VFA by the analytical approach, which explains the banding artifact shown in Figure 5.8 (C) with VFA-ana, but not in Figure 5.8 (D) with VFA-opt at the same location. This was also demonstrated in the 2D bSSFP phantom images (Figure 5.7), where VFA-opt showed a broader passband. However, VFA-ana was close to optimal.

The improvement of VFA compared to CFA is significant when T_2 is short compared to scan time, for example HP [^{14}N, ^{13}C]urea (T_2 = 280ms) 2D imaging (scan time = 864ms), or HP lactate (T_2 around 2s) 3D imaging (scan time = 4.32s). On the other hand, some other HP ^{13}C labeled compounds have longer T_2, such as [^{15}N, ^{13}C]Urea (T_2 around 1-10s). In the case when T_2 is close to or even longer than scan time, the optimal flip angle scheme would be a CFA of 180°, in terms of SNR, spatial resolution, and off-resonance robustness.

5.6.2 Comparison of VFA Designs

Two VFA designs were developed and applied for HP ^{13}C MRI. The first one using an analytical approach is an extension of previous method in [Worters and Hargreaves, 2010] with target on a predefined signal profile as k-space modulation and making full use of magnetization in transient state. As a result, the image performance can be predicted and controlled, such as for improving spatial resolution and SNR simultaneously. This is an

improvement over a prior method [Paul and Zaitsev, 2009]. A trapezoidal shape was used for VFA design in [Paul and Zaitsev, 2009] and the parameters of VFA were chosen empirically, without explicit specification on k-space modulation function, which resulted in improved SNR but sacrificing spatial resolution.

A similar approach of VFA design has been developed for HP noble gases studies [Deppe and Wild, 2012], however, it differs in that iteration is not needed to optimize the signal level. This is because it solved the VFA design in a specialized scenario, by ignoring the signal at thermal equilibrium and also specifying the final longitudinal magnetization Mz = 0. In that case there is no constraint on the initial Mz. However, when there is non-zero thermal equilibrium signal or non-zero desired residual Mz, such as for a dynamic HP ^{13}C MR study, the initial Mz cannot be arbitrarily scaled and an iteration approach is needed. The method with iterations only takes around 14ms to compute (n=96), which is not a concern.

The second VFA design also targeted a predefined signal profile, but over both time and a range of off-resonance frequencies, to improve B_0 robustness. An optimization approach was successfully developed which balanced the performance between on-resonance spins and off-resonance spins, and resulted in reduced signal oscillations for off-resonance spins. The VFA-opt is similar to the VFA-ana, except that the last several flip angles change more smoothly and maintain a lower value, which leads to a lower peak amplitude and reduced total power. For example, the VFA-opt used in the HP phantom study (Figure 5.1) has total energy of 72.2 % of CFA (40°), and 52.1 % of VFA-ana. The RF peak amplitude of VFA-opt is 175.5% of CFA, and 45.9% of VFA-ana. VFA-opt usually has relatively low flip angles, which is an important feature for peak B_1 and SAR constraints in clinical applications. This could be explained by the concept of effective flip angle with off-resonance, as defined in [Zun and Nayak, 2006], which showed that the steady state signal for off-resonance spins at TE is equivalent to the signal of on-resonance spins with a larger effective flip angle. This concept of effective flip angle can be applied to our study even though we focused on transient state bSSFP with VFA. Also note VFA-opt changes smoothly compared to VFA-ana, which

reduces B_1 sensitivity. However, with larger number of variables of flip angles, such as 3D imaging (n=480), the optimization approach takes long computation time. In that case the analytical approach provides an easy-to-calculate and near-optimal alternative.

A VFA design using optimization methods has been previously developed [Smith *et al.*, 2010], however, our new method differs in several aspects. First, only one single metric was defined as the objective function in [Smith *et al.*, 2010], such as SNR, based on the assumption that all the parameters and experimental conditions can be measured and simulated, such as distribution of T_1, T_2, B_1, and off-resonance frequency. This can be impractical for applications where measuring all of these would be challenging and time consuming. In our approach, we specified the k-space modulation function including B_0 and B_1 robustness, such that the same VFA could be applied under a broader range of conditions. In [Smith *et al.*, 2010], the objective function was optimized with a multistage algorithm based on the piecewise approximation, because optimization with all the flip angles as variables would be prohibitively time consuming for even moderate number of TRs (e.g. n=96). This is partially because only the cost function was evaluated without providing the gradient. In this work, the gradient of the bSSFP signal formulation with respect to flip angle and RF pulse phase was derived, which made the computation much faster and more reliable compared to approximating with finite differences [Nocedal and Wright, 2006]. For the example of our VFA design (n = 192) shown in Figure 5.4, optimization without the derived gradient takes 2.7 fold more time, and was still trapped in a suboptimal point. As most algorithms for nonlinear optimization require knowledge of gradient, the derived gradient can also applied for other bSSFP-based optimization problems.

5.6.3 Preparation Pulse

In the optimization approach, the preparation pulses are automatically designed together with the flip angles for acquisition by including preparation pulses as variables in the op-

timization. The optimal preparation pulses are obtained, which still has an increasing ramp, though with a slightly different shape from [Deshpande *et al.*, 2003; Le Roux, 2003; Paul and Hennig, 2004]. This result demonstrates the previous analytical approach of preparation pulse design is close to optimal, and yields another mathematical point of view to understand the preparation pulse.

5.6.4 Signal Evolution in VFA bSSFP

For conventional bSSFP with CFA, the signal evolution during the transient state has been well studied using linear-systems analysis and eigenvector formalism [Hargreaves *et al.*, 2001; Scheffler, 2003; Ganter, 2004]. However, such methods do not apply for transient state bSSFP with VFA. In this work, we studied the signal evolution qualitatively through Bloch simulations. Interestingly, we found that some desired characteristics of CFA bSSFP such as its refocusing property also hold for VFA bSSFP, so long as flip angles change slowly, which is important to determine readout gradient and improve off-resonance robustness.

5.6.5 Other Applications

The optimization approach of VFA design can also be applied for other applications to optimize bSSFP imaging performance over a range of some parameters such as different T_1 or T_2 values, to either maximize or minimize contrast. Another interesting application would be to optimize SNR with a non-uniform signal profile and non-sequential encoding ordering, with a higher signal level at k-space center.

5.7 Conclusion

A new optimization approach for bSSFP variable flip angle design was developed for HP ^{13}C imaging. In HP ^{13}C-urea experiments we demonstrated improved SNR, reduced image

blurring, and improved off-resonance insensitivity. An analytical approach for variable flip angle design was also developed for HP ^{13}C, extending a previous developed method [Worters and Hargreaves, 2010], that provides an easy-to-calculate and near-optimal alternative to the optimization approach. In HP ^{13}C-lactate 3D bSSFP imaging experiments this analytic approach demonstrated improved detection of small structures.

5.8 Appendix A: Derivation of the gradient of the cost function

The partial derivative of the cost function 5.10 with respect to flip angle, α_i, is derived, while the partial derivative with respect to RF phase, φ_i, can be derived in a similar way, and is not shown here to conserve space.

$$\frac{\partial f(\alpha,\varphi)}{\partial \alpha_i} = p2 \sum_{j=1}^{m} (\sum_{k=1}^{n} (|M_{xyk}| - M_{d,k})^{p1})^{\frac{p2}{p1}-1} \sum_{k=1}^{n} (|M_{xyk}| - M_{d,k})^{p1-1} \frac{\partial |M_{xyk}|}{\partial \alpha_i} \tag{5.11}$$

where

$$\frac{\partial |M_{xy,k}|}{\partial \alpha_i} = \frac{1}{\sqrt{M_{xk}^2 + M_{yk}^2}} (M_{xk} \frac{\partial M_{xk}}{\partial \alpha_i} + M_{yk} \frac{\partial M_{yk}}{\partial \alpha_i}) \tag{5.12}$$

For the partial derivative of M_k with respect to α_i and φ_i,

1. $k < i$, M_k is not a function of α_i and φ_i

$$\frac{\partial M_k}{\partial \alpha_i} = 0 \tag{5.13}$$

2. $k = i$, $M_i = AB(\alpha_i, \varphi_i)AM_{i-1}$. AM_{i-1} and A are not a function of α_i and φ_i.

$$\frac{\partial M_k}{\partial \alpha_i} = A\frac{\partial B(\alpha_i, \varphi_i)}{\partial \alpha_i}AM_{k-1} \tag{5.14}$$

3. $k > i$, $M_k = AB(\alpha_k, \varphi_k)AM_{k-1}$. $AB(\alpha_k, \varphi_k)A$ is not a function of α_i and φ_i, while M_{k-1} is a function of α_i and φ_i.

$$\frac{\partial M_k}{\partial \alpha_i} = AB(\alpha_k, \varphi_k)A\frac{\partial M_{k-1}}{\partial \alpha_i} \tag{5.15}$$

Recall equation 5.3

$$\begin{aligned} B &= R_z(-\varphi)R_x(\alpha)R_z(\varphi) \\ &= \begin{pmatrix} (\cos\varphi)^2 + \cos\alpha(\sin\varphi)^2 & \frac{1}{2}\sin 2\varphi(1-\cos\alpha) & -\sin\varphi\sin\alpha \\ \frac{1}{2}\sin 2\varphi(1-\cos\alpha) & (\sin\varphi)^2 + \cos\alpha(\cos\varphi)^2 & \cos\varphi\sin\alpha \\ \sin\alpha\sin\varphi & -\sin\alpha\cos\varphi & \cos\alpha \end{pmatrix} \end{aligned}$$

$$\frac{\partial B}{\partial \alpha} = \begin{pmatrix} -\sin\alpha(\sin\varphi)^2 & \cos\varphi\sin\varphi\sin\alpha & -\sin\varphi\cos\alpha \\ \cos\varphi\sin\varphi\sin\alpha & -\sin\alpha(\cos\varphi)^2 & \cos\varphi\cos\alpha \\ \cos\alpha\sin\varphi & -\cos\alpha\cos\varphi & -\sin\alpha \end{pmatrix} \tag{5.16}$$

5.9 Appendix B: Determine Hyperparameter in the Optimization

A practical issue is how many frequency samples to be considered in the cost function 5.10, which depends on how fast the signal profile changes as a function of off-resonance frequency. 20 frequency samples were chosen empirically, as higher number of samples did not change the results. Only profiles on one side need to be specified to reduce computation by half,

because the signal profile is symmetric about frequency = 0. RF pulse phase was fixed as alternating between 0 and π, because that is typically close to the optimal results with RF pulse phase as variables. This reduces the variable dimension by half and accelerates the optimization process. This also helps to maintain the internal refocusing capability. The definition of norm in the cost function 5.10 is set to be p1=2, p2=2, which usually outperform the result by other order of norm. The desired signal strength, Md, is set to be the optimal signal strength from the analytical approach.

Chapter 6

Hand-held Electromagnet Carrier for Transfer of Hyperpolarized ^{13}C Samples

6.1 Abstract

Hyperpolarization of ^{13}C nuclei by dissolution Dynamic Nuclear Polarization (DNP) increases SNR by $>$ 10,000 fold for metabolic imaging, but care must be taken when transferring hyperpolarized (HP) samples from polarizer to MR scanner. Some ^{13}C substrates relax rapidly in low ambient magnetic fields. A hand-held electromagnet carrier was designed and constructed to preserve polarization by maintaining a sufficient field during sample transfer. The device was constructed with a solenoidal electromagnet, powered by a non-magnetic battery, holding the HP sample during transfer. A specially designed switch automates deactivation of the field once transfer is complete. Phantom and rat experiments were performed to compare MR signal enhancement with or without the device for HP [^{13}C]urea and [1-^{13}C]pyruvate. The magnetic field generated by this device was tested to be $>$ 50 Gauss over a 6 cm central section. In phantom and rat experiments, [^{13}C]urea transported via the device showed SNR improvement by a factor of 1.8-1.9 over samples transferred through the background field.

6.2 Introduction

Hyperpolarized (HP) Carbon-13 MRI with dissolution Dynamic Nuclear Polarization (DNP) [Ardenkjær-Larsen *et al.*, 2003] has recently been shown to provide biologic information on previously inaccessible aspects of metabolic processes by detecting endogenous, nontoxic ^{13}C-labeled probes to monitor enzymatic conversions through key biochemical pathways [Golman *et al.*, 2003; Golman *et al.*, 2006; Chen *et al.*, 2007]. Since both spatial and chemical information are encoded, this new molecular imaging modality allows simultaneous detection of multiple biologic compounds and metabolic products with sensitivity enhancements of $>$ 10,000 fold [Ardenkjær-Larsen *et al.*, 2003]. The recently completed Phase 1 clinical trial conducted at UCSF demonstrated the safety and feasibility of HP ^{13}C-pyruvate MRI in prostate cancer patients without any dose-limiting or other notable toxicities [Nelson *et al.*, 2013].

Some HP ^{13}C substrates can lose polarization extremely quickly in low magnetic field when they are transferred between the polarizer and the MR scanner, reducing the SNR. For example, scalar coupling between fast-relaxing quadrupolar ^{14}N and ^{13}C results in rapid loss of polarization of [^{13}C]urea [Chiavazza *et al.*, 2013]. Although most in vivo HP ^{13}C MRI studies have focused on probing metabolism using metabolically active substrates [Kurhanewicz *et al.*, 2011], several studies have shown that metabolically inactive agents like [^{13}C]urea can be applied to angiography or perfusion imaging [Johansson *et al.*, 2004; Svensson *et al.*, 2003]. HP [^{13}C]urea for perfusion MRI has advantages over conventional gadolinium (Gd) containing (paramagnetic) contrast agents including direct proportionality of signal to concentration, inherently high contrast-to-noise ratio (CNR) due to the absence of background signal, and an excellent safety profile potentially benefitting studies in patients currently excluded from contrast imaging studies. Also, [^{13}C]urea can be co-polarized with [1-^{13}C]pyruvate for combined perfusion and metabolic imaging [Wilson *et al.*, 2010; von Morze *et al.*, 2012b]. Urea is a safe, endogenous compound with normally high concen-

trations in vivo (typically 1-10 mM, and much higher in the renal medullary interstitium), low toxicity, and neutral pH, as well as the key MR properties of long T_1 relaxation time and high polarization by DNP. Recent studies have also demonstrated the ability of HP [^{13}C]urea to investigate changes in urea transport and concentration in the kidney [von Morze *et al.*, 2012a].

In previous studies, this loss of polarization of [^{13}C]urea during sample transfer has been addressed by carrying a permanent magnet next to the HP sample, or at the molecular level by secondary labeling with ^{15}N [Chiavazza *et al.*, 2013; Reed *et al.*, 2014]. However, the cost of [^{13}C,$^{15}N_2$]urea is about 5 times higher than [^{13}C]urea. Furthermore, J-coupling in [^{13}C,$^{15}N_2$]urea splits the ^{13}C NMR resonance peak into a triplet thus lowering the signal amplitude and potentially confounding quantitation. The permanent magnet method raises safety concerns since it could fly into the scanner causing harm. In addition, permanent magnets provide non-uniform fields and are especially impractical for large samples. To address these limitations, we constructed and tested a new electromagnet carrier device to provide a suitable and relatively uniform magnetic field for the safe transfer of HP samples for ^{13}C MR studies.

6.3 Theory

Spin-lattice relaxation depends on several independent mechanisms, including interactions with paramagnetic centers and scalar coupling between fast-relaxing quadrupolar nuclei, which cause faster relaxation when the magnetic field decreases. Quadrupolar nuclei with spin $> 1/2$ (e.g. ^{14}N) have very short T_1. The scalar coupling of ^{13}C to ^{14}N provides a relaxation mechanism for ^{13}C as ^{14}N is undergoing very rapid T_1 relaxation. The scalar coupling relaxation rate can be calculated by equation 6.1.

$$R_{sc} = \frac{8\pi^2 J^2}{3} I(I+1) \frac{T_1}{1 + (\Delta\omega)^2 T_1^2} \tag{6.1}$$

In equation 6.1, R_{sc} is the scalar coupling relaxation rate, J is the scalar coupling constant in Hz, I is the spin quantum number of the coupled nucleus ($I_{^{14}N} = 1$), T_1 is the spin-lattice relaxation time of the quadrupolar nucleus (^{14}N), $\Delta\omega = \omega_{^{13}C} - \omega_{^{14}N}$ is the difference in Larmor frequencies of coupled nuclei ^{13}C and ^{14}N. For this mechanism to be very effective, the Larmor frequencies of these two nuclei must be very close. This condition is met at low magnetic fields such as during HP sample transfer, although it may also occur at high field, for example for ^{13}C (15.087 MHz) and ^{79}Br (15.023 MHz) at 1.41T [Lyerla Jr *et al.*, 1971]. One approach to reduce the scalar coupling relaxation mechanism is to increase the external magnetic field.

6.4 Methods

6.4.1 Simulation and Background Field Measurements

The ambient magnetic field through which the HP samples were transferred was measured with a three-axis Hall effect magnetometer (model THM 7025, Metrolab Technology SA, Switzerland), as shown in Figure 6.1(A). The distance of 0m corresponds to the location of the DNP polarizer, while the distance of 15.4m corresponds to the center of the MR scanner. R_{sc} can be estimated as a function of magnetic field based on equation 6.1, given parameters measured in [Chiavazza *et al.*, 2013], including $T_1 = 1.0 \pm 0.1ms$, $J = 14.5 \pm 0.1Hz$, as shown in Figure 6.1(B). Assuming a piece-wise constant relaxation rate along the path and constant transfer velocity over a 6s transfer, the signal decay curve can be estimated along this path, as plotted in Figure 6.1(C).

By adding a magnetic field offset of 50 G (along vertical direction) in simulation, this scalar coupling relaxation mechanism can be significantly reduced as shown in Figure 6.1(B), resulting in a 1.83-fold signal improvement at the end of the path, as shown in Figure 6.1(C). This field strength specification was used for the design of this device in order to provide an

adequate magnetic field to maintain a long T_1 for HP samples during transfer.

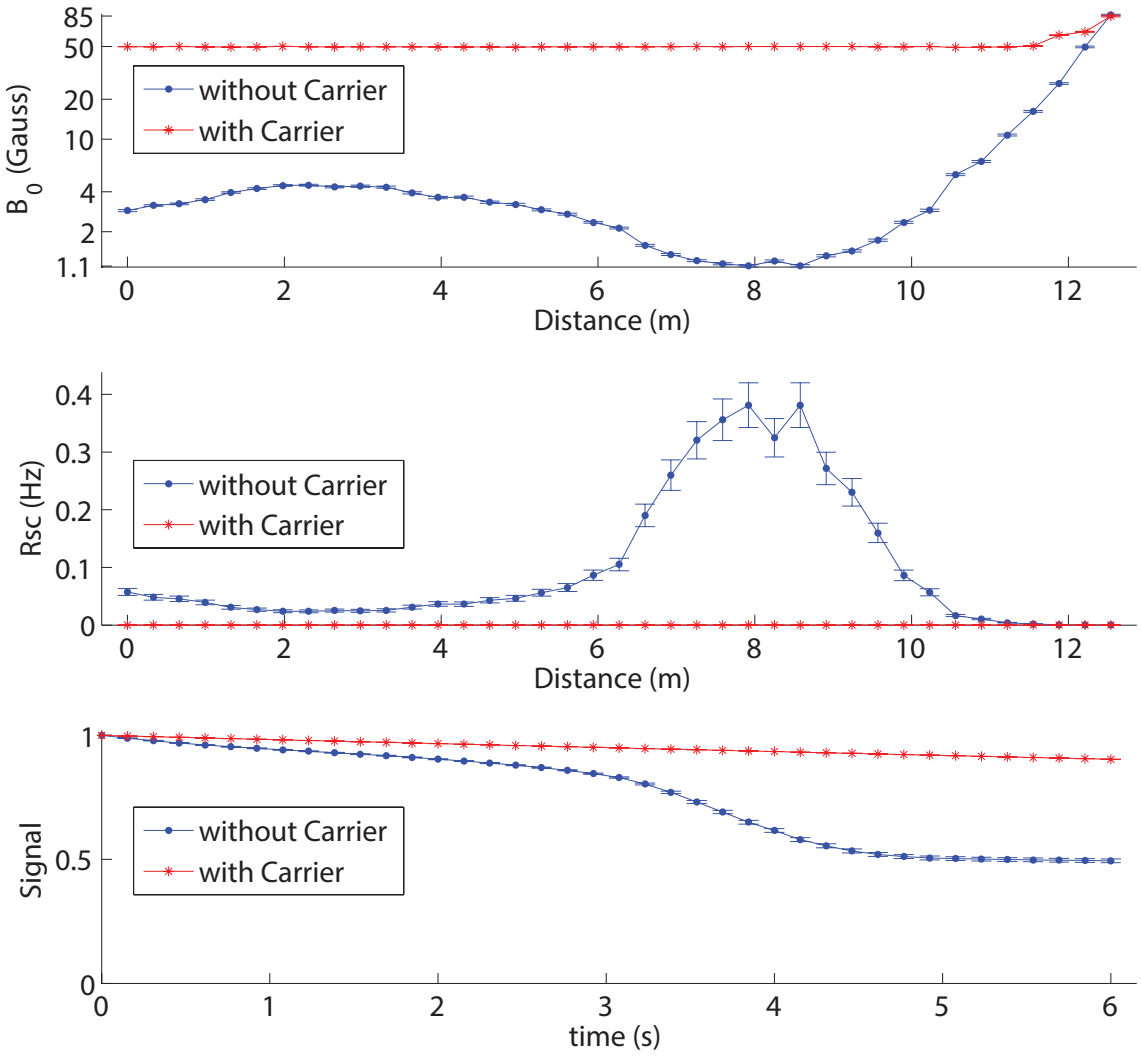

Figure 6.1: Measured ambient magnetic field magnitudes along sample transfer path (without carrier, blue line with dots) and simulated field magnitude with 50G added along vertical direction (with carrier, red line with stars) (A). Y axis (B_0) is displayed with a log scale. The distance of 15.4m corresponds to the center of the MR scanner and 0m corresponds to the location of the DNP polarizer. The range of distance (0 m to 13.4 m) corresponds to the part of sample transfer path where the device was used. Estimated scalar coupling relaxation rate of HP [^{13}C]urea along the path corresponding to the two different fields (B). Estimated signal decay curve along the path assuming piece-wise constant relaxation rate and constant transfer speed within 6s (C).

6.4.2 Hardware

The electromagnet carrier device was designed to provide a suitable magnetic field for the safe transfer of HP samples. The key part of the device is a solenoid with a current of 0.5A powered by a non-magnetic battery to generate a relatively uniform magnetic field of >50 G over a 6 cm longitudinal section. The size of the solenoid was customized for the specific 3mL and 5mL syringes (BD, Franklin Lakes, NJ) commonly used for preclinical HP ^{13}C studies. The inner diameter was designed to be 1.65 cm and the length 7.9cm. The gauge of the wire (22 AWG) and number of layers (6 layers) were chosen based on the desired field of 50 G, resulting in a total of 727 turns.

The circuit is shown in Figure 6.2(A). A single-cell (3.7V) 500mAH lithium-ion polymer (LiPo) battery (E-flite/Horizon Hobby, Champaign, Illinois) composed of non-magnetic materials powered the magnetic field. The device can be safely carried into the 3T MRI scanner room and turned off there. The current was activated by depressing the default-open, pushbutton momentary switch. When the button was released the current was turned off automatically. The design of the switch ensures that the device can be safely operated in the scanner room, covering the entire sample transfer path and thus minimizing the loss of polarization. A LED was installed to indicate when the device is activated. The battery can provide stable current for at least 1 hour of continuous use. The sample transfer duration is $<$ 10s, so one battery charge can last for hundreds of HP experiments.

The device (in Figure 6.2(C)) was constructed using a combination of custom 3D printed parts and commercially available parts meeting the design criteria for performance, non-magnetic materials, and durability. The housing was built with strength to withstand drops to the floor and the shape was designed for ease of carrying and standing upright. The switch was trigger-mounted to enable easy depression, holding and releasing of the button. The battery was attached on the surface of the device in a manner allowing easy replacement or charging. The inner diameter of the solenoid-encompassed sample chamber closely fits the

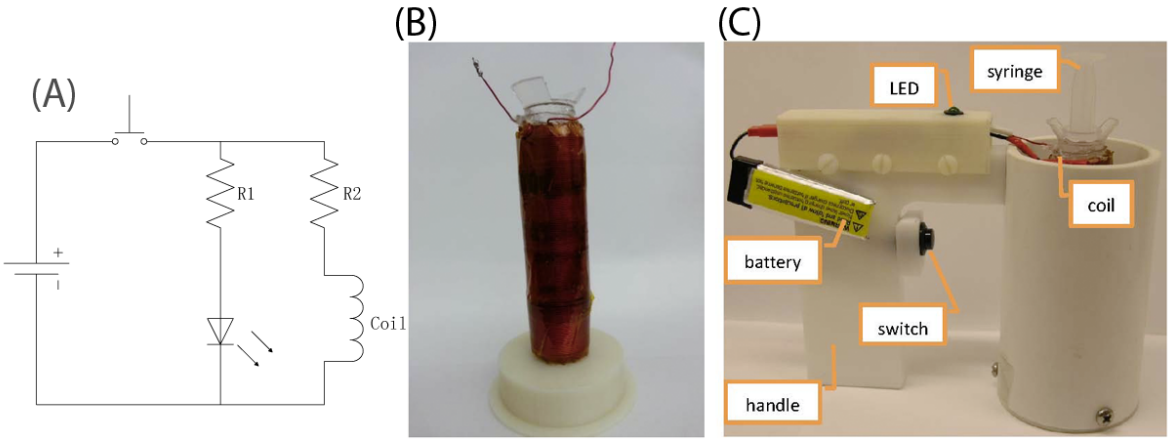

Figure 6.2: Hardware design of electromagnet carrier device. Circuit diagram (A). Resistance of coil = 2.9 Ohm, R1 = 833 Ohm, R2 = 4.4 Ohm. A non-magnetic LiPo 500 mAH battery supplies 3.7V and a current of 0.5A in the coil (current in the LED 2.1mA). The switch is a default-open pushbutton momentary switch. Photo of the solenoid inside (B) and photo of the whole device (C).

syringes, which are quickly guided through a conical opening on top of the coil, as shown in figure 6.2(B).

6.4.3 Magnetic Field Measurements

The strength, stability, and uniformity of the device magnetic field were simulated and measured. The magnetic field strength along the central axis was first simulated based on the Biot-Savart Law. Assuming that the magnetic field in the solenoid is uniform so that the field strength along the central axis approximates the field inside the solenoid. The same magnetometer described above was used to measure the field inside the solenoid. The solenoid for the actual device had a smaller inner diameter, which was customized for the sample size. This smaller size was too narrow for the probe of the magnetometer. Therefore a prototype solenoid with larger size was constructed in order to test the accuracy of the field simulation by comparisons with the measured results.

6.4.4 HP MR Phantom Experiments

Experiments were performed to test the effect of the device on HP [^{13}C]urea and copolarization of [^{13}C]urea and [1-^{13}C]pyruvate. Dissolution DNP was performed with a HyperSense polarizer (Oxford Instruments, Oxford, UK) operating at 1.3 K and 3.35 T, using previously described methods, generating 4.5mL 100mM HP media [von Morze *et al.*, 2012b]. MR experiments were performed on a 3T clinical MRI scanner (GE Healthcare, Waukesha, WI, USA) with a broadband RF amplifier. Custom built, dual-tuned mouse birdcage coils (l=8cm, d=5cm) were used for RF transmission and signal reception. The RF transmit gain was calibrated with a ^{13}C enriched urea phantom with similar size and similar location as HP phantom.

After dissolution, the HP sample was divided into two equally apportioned syringes, and both were carried to the scanner at the same speed along the same path. One was transferred in the ambient field, while the other was transferred with this device. The device was turned on during DNP dissolution and kept activated throughout the transfer from DNP polarizer to MR scanner. It was deactivated at around 2m away from the center of MR scanner where the fringe field is already sufficiently large. The device was held vertically during transfer such that the magnetic field from this device was added to the fringe field instead of potentially cancelling each other. The sample transfer took approximately 6s.

The solutions were then injected into two fixed syringe reservoirs already lying inside the coil, oriented along the longitudinal direction. The signal of these two samples was then acquired together with one pulse sequence and approximately the same local B_0 and B_1 fields. In this manner, the differences in signal between the samples transferred with and without the device were calculated from the same experiment, while controlling for any variations in initial polarization, total amount of sample, and transfer duration. Another control group experiment was done with the same imaging methods, but both samples were transferred without the device. The urea-only experiment and control group experiment were repeated

four times respectively, and the copolarization experiment was repeated five times.

For the urea-only tests, the axial images were acquired with single shot EPI readout, with no localization along the longitudinal direction. The acquisitions used a flip angle=90°, TE=100ms, TR=250ms, matrix size=20x20, FOV=10x10cm^2. For urea and pyruvate copolarization tests, a dynamic 1D MRSI sequence was used with hard pulse excitation (0.5ms duration), double spin echo refocusing and symmetric EPI readout [Cunningham *et al.*, 2007]. Spatial encoding was only applied along the x direction (right/left) with projections along y and z directions. Localization along this direction enabled separation of the samples transferred with and without the device. The readout gradient duration was 100ms giving a spectral resolution of 10Hz, with spectral bandwidth of 543 Hz to include the resonances of both pyruvate and urea. For image reconstruction, the even and odd EPI lobe data were combined by the sum-of-squares method. The data were acquired using a flip angle=10°, TE=140ms, and TR=2s. Although the amounts of HP material in each syringe were approximately equal, the signal at thermal equilibrium was also measured to compensate for any potential residual differences in the amount of HP sample in each syringe.

6.4.5 HP MR in vivo Experiments

HP [^{13}C]urea in vivo rat experiments were performed using a balanced SSFP sequence [Reed *et al.*, 2014] to acquire a coronal image (projection along A/P direction) following an IACUC-approved protocol. The experiments were repeated twice on the same animal, one with HP sample transferred in ambient field, the other transferred with this device, while keeping all the other parameters the same. [^{13}C]urea was polarized for 88±1 min and transferred to the scanner within 7s. 2.5mL 100mM solution was injected into a rat through tail vein catheter over 12s with image acquisition starting at 20s after the beginning of injection. The imaging parameters were: flip angle=60°, TR=15ms, matrix size=140x70, FOV=20x10cm^2, sequential phase encoding.

6.5 Results

6.5.1 Magnetic Field Tests

The simulated and measured magnetic field distributions within the solenoid are shown in Figure 6.3. Figure 6.3(A) corresponds to the larger prototype solenoid, while Figure 6.3(B) corresponds to the actual solenoid used in this device. The measured results were close to the simulated results, but slightly higher in the center, as shown in Figure 6.3(A). Using the same simulation method, we calculated the magnetic field of the device to be $>$ 50G over a 6cm central section, as shown in Figure 6.3(B). Even though the magnetic field drops quickly at both ends, the field is relatively uniform in the 3cm central section where HP media is usually placed. When holding the switch and keeping the electric current on for about 30 seconds (sample transfer usually takes less than 10s), the measured magnetic field remained constant, thereby demonstrating the stability of the device.

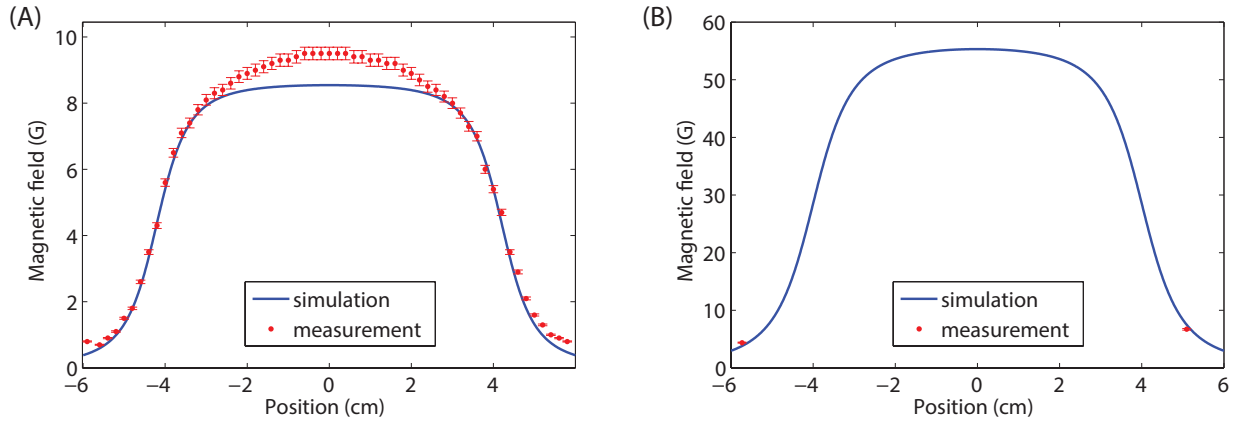

Figure 6.3: Simulated (blue line) and measured (red dots) magnetic field distribution in the prototype solenoid with larger diameter (A) and the solenoid used in the device (B). Error of measurement (shown as red error bars) were determined from the accuracy of the magnetometer. The measured field distribution was not available for the solenoid in the device because its size is smaller than the probe of the magnetometer, but the calculation demonstrated a field of greater than 50G over the central 6 cm.

6.5.2 HP MR Tests

In the HP [^{13}C]urea phantom experiments, the [^{13}C]urea signal in both syringes is shown in one axial image (e.g. Figure 6.4(A)). The SNR increase achieved by using this device was demonstrated by the ratio of image intensity. The results showed a significantly ($p = 0.012$) higher (1.9 ± 0.2) [^{13}C]urea signal using the device. The result of the control group demonstrated a small effect between syringe locations (+4%). However, this effect was much smaller than the experimental signal ratio (≈1.9), and therefore does not alter the conclusion that SNR increased by about 2-fold. Also, this small effect in the control group failed to reach statistical significance ($p = 0.098$).

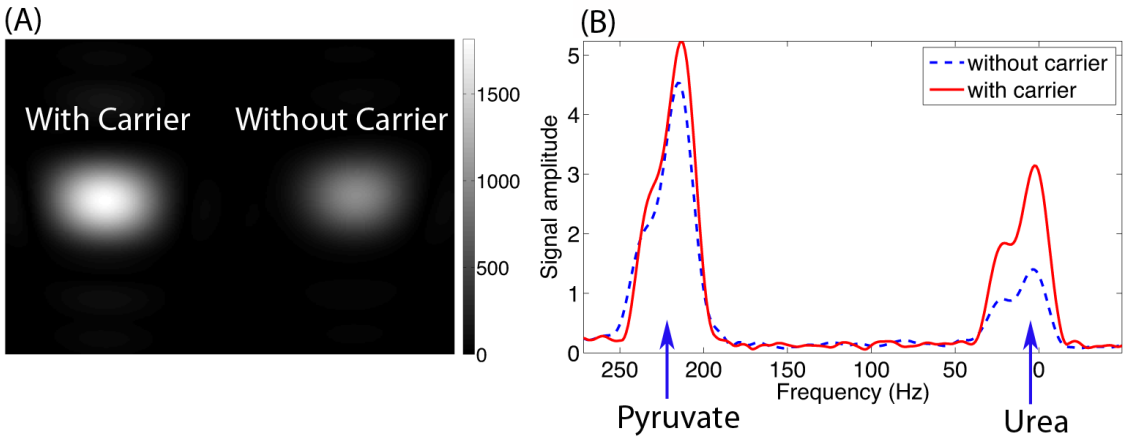

Figure 6.4: Example of experimental comparisons between two HP samples scanned in one acquisition, one sample carried with this device (with Carrier), the other carried in ambient field (without Carrier). The just urea experiment was performed using axial ^{13}C MRI (A), while the copolarization of urea and pyruvate MRSI experiment resulted in two spectral peaks corresponding to the two HP compounds acquired from the samples transported with (solid red line) and without the carrier device (dotted blue line) (B). For copolarization results, the left peak corresponds to pyruvate and the right peak corresponds to urea. The center frequency was set close to the urea frequency.

For the HP copolarization phantom experiments, spectroscopic imaging was acquired to distinguish the different compounds based on frequency, and the different samples transferred

with and without the device based on spatial location. The spectra were analyzed for each resonance and each transfer approach (e.g. Figure 6.4(B)). The data showed a significantly ($p = 0.002$) higher (1.9 ± 0.3) [^{13}C]urea signal intensity in the sample transferred with the device. [1-^{13}C]pyruvate signal intensity is slightly higher (1.1 ± 0.1), however, it failed to reach statistical significance ($p=0.550$).

The results of HP [^{13}C]urea in vivo experiment are shown in Figure 6.5, along with the corresponding image from a 3D balanced SSFP ^{1}H scan. The coronal ^{13}C image with sample transferred with the device has improved SNR. Quantitatively measuring the SNR at the center of right kidney shows a SNR improvement of 1.8-fold with this device.

6.6 Discussion

This device enabled a nearly 1.9-fold SNR improvement of HP urea signal as compared to samples carried in the ambient field, in HP [^{13}C]urea experiments, HP urea and pyruvate copolarization experiments, and one in vivo experiment. The observed 1.8-1.9 fold SNR improvement from experiments is close to the expected 1.83-fold increase predicted by simulation, which indicates that the hypothesis of fast signal decay due to scalar coupling relaxation is correct and the model we use (equation 6.1) is accurate. Therefore this model can be used for further study with other HP molecules. The SNR improvement may be even more significant in cases where the ambient field along transfer path is lower than in our facility.

Although [1-^{13}C]pyruvate is not affected by scalar coupling relaxation, other relaxation mechanisms could affect it at low field, such as relaxation via paramagnetic centers (radical and gadolinium in solution). However, in our copolarization experiments the [1-^{13}C]pyruvate signal was not significantly different with or without the device. Theoretically the effect of relaxation via paramagnetic centers is small due to very low concentration of radical or gadolinium in the liquid state [Caravan *et al.*, 1999; Gordon *et al.*, 2012]. Furthermore, this

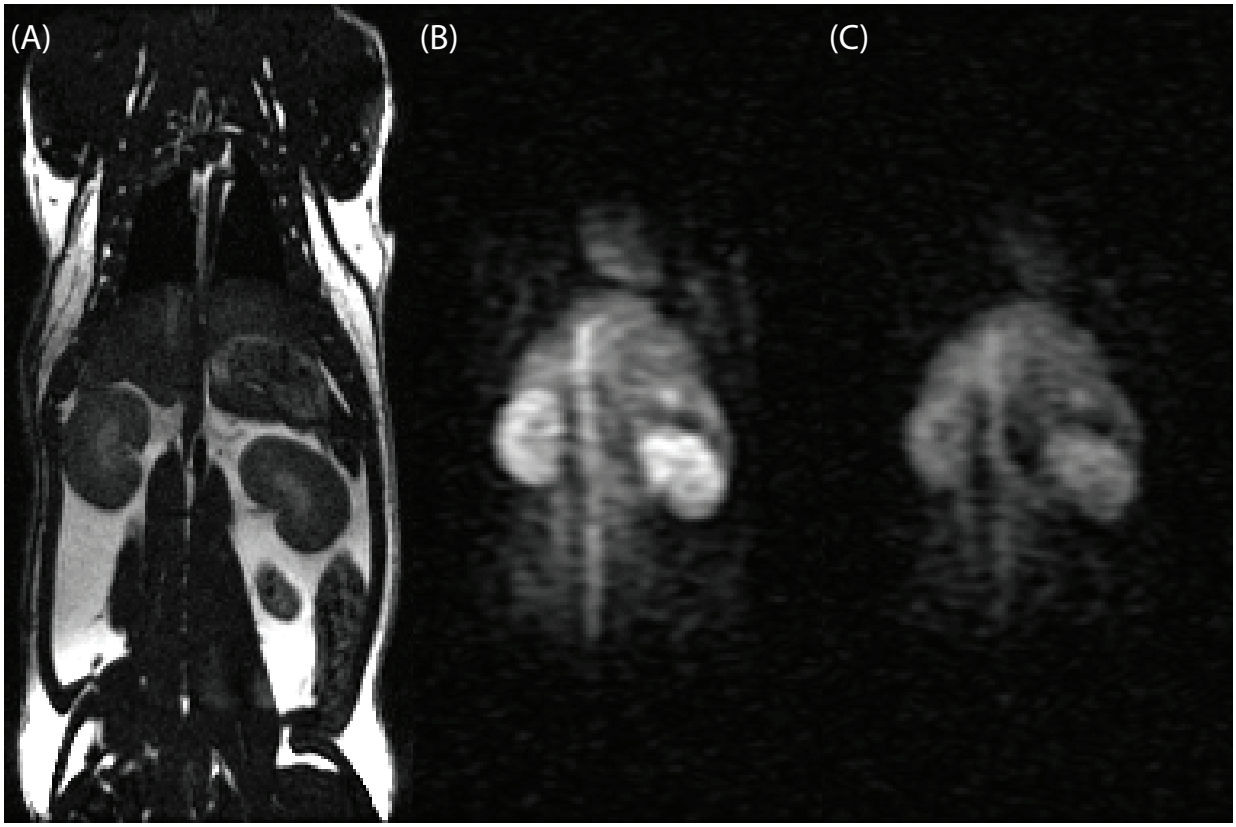

Figure 6.5: In vivo rat experiment results. (A) A coronal slice of a ^{1}H 3D balanced SSFP sequence. (B) HP [^{13}C]urea images using a 2D (coronal) balanced SSFP sequence (projection along A/P direction) with sample transferred with this device. (C) The same acquisition repeated on the same animal and position, but with sample transferred in ambient field. (B) and (C) were acquired with the same image parameters and experimental setup and differed only in the transfer method. (B) and (C) are displayed with the same window. SNR (measured at right kidney center) in (B) was 1.8 times higher using this device than without (C).

possible mechanism would likely have a small effect considering the transfer time is just 6s, as a small fraction of expected T_1 value [Chattergoon *et al.*, 2013]. However, use of this device would prevent pyruvate relaxation effects that could occur at very low fields at some locations.

While the initial testing was focused on HP [^{13}C]urea and [1-^{13}C]pyruvate, it could also benefit other compounds. For example, HP [5-^{13}C]glutamine is being developed as

a noninvasive imaging marker for glutaminolysis, allowing improved diagnosis and monitoring of glutamine-dependent tumors [Gallagher *et al.*, 2008; Keshari and Wilson, 2014; Daye and Wellen, 2012]. Similar to urea, this substrate is also affected by coupling between ^{13}C and ^{14}N.

6.7 Conclusion

A electromagnet carrier device was designed and built to supply a suitable and safe magnetic field (> 50 G) to preserve polarization during HP sample transfer, especially for compounds with scalar coupling between fast-relaxing quadrupolar ^{14}N and ^{13}C, such as in HP [^{13}C]urea. In comparative testing, this device demonstrated SNR improvements of approximately 2-fold for [^{13}C]urea while maintaining the signal of HP [1-^{13}C]pyruvate.

Chapter 7

Conclusion

7.1 Summary of Findings

In Chapter 3, I showed a framework for general RF pulse design using the SLR algorithm and convex optimization. This algorithm can create RF pulses with multiband magnitude profile, arbitrary phase profile, and generalized flip angle. Spectral sparsity was exploited to further improve pulse performance in terms of pulse duration, peak amplitude, total energy, transition width, or profile ripple, with flexible trade-offs. For example designs were presented for shorter duration pulses for a bSSFP ^{13}C sequence at 14T; a dualband saturation pulse with sharper transition widths for ^{1}H MRS at 3T; and a saturation pulse with extremely low stopband ripple for suppression of undesired resonances in HP ^{13}C studies.

In Chapter 4, I developed a spectrally selective 3D dynamic bSSFP sequence for HP ^{13}C metabolite imaging with subsecond acquisition time and 2mm isotropic resolution. High spectral selectivity ($\sim$100:1) of the bSSFP sequence was achieved by using short-duration optimized spectrally selective RF pulses and carefully choosing TR to avoid excitation banding artifacts. This sequence is expected to be useful for preclinical HP ^{13}C studies at high field and holds potential for clinical studies.

In Chapter 5, a new optimization approach for bSSFP variable flip angle design was developed for HP ^{13}C imaging. In HP ^{13}C-urea experiments I demonstrated improved SNR, reduced image blurring, and improved off-resonance insensitivity. An analytical approach

for variable flip angle design was also developed for HP ^{13}C, that provided an easy-to-calculate and near-optimal alternative to the optimization approach. In HP ^{13}C-lactate 3D bSSFP imaging experiments, this analytic approach demonstrated improved detection of small structures.

Finally, in Chapter 6, we described design of an electromagnet carrier device to supply a suitable and safe magnetic field ($>$ 50 G) to preserve polarization during HP sample transfer, especially for compounds with scalar coupling between fast-relaxing quadrupolar ^{14}N and ^{13}C, such as in HP [^{13}C]urea. In comparative testing, this device demonstrated SNR improvements of approximately 2-fold for [^{13}C]urea while maintaining the signal of HP [1-^{13}C]pyruvate.

7.2 Future Directions

The new pulse sequence developed in Chapter 4 could be extended to other field strengths, like HP ^{13}C studies at 3T for potential clinical application. At lower field, the frequency separation between multiple compounds reduces, which will increase the minimal achievable RF pulse duration, and thus minimal achievable TR. In that case undersampling methods including parallel imaging, compressed sensing and partial Fourier acquisition can be applied for improving temporal resolution, spatial resolution or volumetric coverage. Sequential phase encoding is used in the current implementation, and the 3D k-space center is sampled in around 0.5s, which is on the order of T_2 values of ^{13}C compounds and could result in suboptimal SNR. Center out encoding could be used to further improve SNR. A constant flip angle was used for all dynamic time points in this study. A progressively increasing flip angle for subsequent dynamic acquisitions would be likely to extend the imaging window by allocating signal more equally over time. This method can also be applied to water-fat separation in ^{1}H bSSFP. The method of choosing TR developed in this work can be applied to improve stopband suppression and reduce requirements on RF pulse design.

The optimization approach of VFA design described in Chapter 5 can also be applied for other applications to optimize bSSFP imaging performance over a range of some parameters such as different T_1 or T_2 values, to either maximize or minimize contrast. Another interesting application would be to optimize SNR with a non-uniform signal profile and non-sequential encoding ordering, with a higher signal level at k-space center.

The spectrally selective bSSFP sequence in Chapter 4 and the VFA bSSFP sequence in Chapter 5 are implemented separately to improve image performance from two different aspects. A future direction would be to combine these two methods.

Bibliography

[Absil *et al.*, 2006] Julie Absil, Vincent Denolin, and Thierry Metens. Fat attenuation using a dual steady-state balanced-ssfp sequence with periodically variable flip angles. *Magnetic resonance in medicine*, 55(2):343–351, 2006.

[Albers *et al.*, 2008] Mark J Albers, Robert Bok, Albert P Chen, Charles H Cunningham, Matt L Zierhut, Vickie Yi Zhang, Susan J Kohler, James Tropp, Ralph E Hurd, Yi-Fen Yen, et al. Hyperpolarized 13c lactate, pyruvate, and alanine: noninvasive biomarkers for prostate cancer detection and grading. *Cancer research*, 68(20):8607–8615, 2008.

[Ardenkjær-Larsen *et al.*, 2003] Jan H Ardenkjær-Larsen, Björn Fridlund, Andreas Gram, Georg Hansson, Lennart Hansson, Mathilde H Lerche, Rolf Servin, Mikkel Thaning, and Klaes Golman. Increase in signal-to-noise ratio of $>$ 10,000 times in liquid-state NMR. *Proc Natl Acad Sci U S A*, 100(18):10158–63, Sep 2003.

[Aronen *et al.*, 2000] Hannu J Aronen, Francisco S Pardo, David N Kennedy, John W Belliveau, Scott D Packard, Dora W Hsu, Frederick H Hochberg, Alan J Fischman, and Bruce R Rosen. High microvascular blood volume is associated with high glucose uptake and tumor angiogenesis in human gliomas. *Clinical Cancer Research*, 6(6):2189–2200, 2000.

[Bieri and Scheffler, 2009] Oliver Bieri and Klaus Scheffler. Ssfp signal with finite rf pulses. *Magnetic Resonance in Medicine*, 62(5):1232–1241, 2009.

[Bieri and Scheffler, 2013] Oliver Bieri and Klaus Scheffler. Fundamentals of balanced steady state free precession mri. *Journal of Magnetic Resonance Imaging*, 38(1):2–11, 2013.

[Boyd and Vandenberghe, 2004] Stephen Boyd and Lieven Vandenberghe. *Convex optimization*. Cambridge university press, 2004.

[Burrus and UniqU,] C Sidney Burrus and LLC UniqU. Chebyshev or equal ripple error approximation filters.

[Caravan *et al.*, 1999] Peter Caravan, Jeffrey J Ellison, Thomas J McMurry, and Randall B Lauffer. Gadolinium (iii) chelates as mri contrast agents: structure, dynamics, and applications. *Chemical reviews*, 99(9):2293–2352, 1999.

[Chattergoon *et al.*, 2013] N. Chattergoon, F. Martinez-Santiesteban, W. B. Handler, J. H. Ardenkjær-Larsen, and T. J. Scholl. Field dependence of T_1 for hyperpolarized [1-^{13}C]pyruvate. *Contrast Media Mol I*, 8(1):57–62, 2013.

[Chen *et al.*, 2007] Albert P. Chen, M. J. Albers, C. H. Cunningham, Susan J. Kohler, Yi-Fen Yen, Ralph E. Hurd, James Tropp, Robert Bok, John M. Pauly, S. J. Nelson, John Kurhanewicz, and Daniel B. Vigneron. Hyperpolarized C-13 spectroscopic imaging of the TRAMP mouse at 3T-initial experience. *Magn Reson Med*, 58:1099–1106, 2007.

[Chiavazza *et al.*, 2013] Enrico Chiavazza, Eugen Kubala, Concetta V. Gringeri, Stephan Duwel, Markus Durst, Rolf F. Schulte, and Marion I. Menzel. Earth's magnetic field enabled scalar coupling relaxation of ^{13}C nuclei bound to fast-relaxing quadrupolar ^{14}N in amide groups. *J Magn Reson*, 227(0):35 – 38, 2013.

[Çukur, 2015] Tolga Çukur. Spectrally selective imaging with wideband balanced steady-state free precession mri. *Magnetic resonance in medicine*, 2015.

[Cunningham and Wood, 1999] Charles H Cunningham and Michael L Wood. Method for improved multiband excitation profiles using the shinnar–le roux transform. *Magnetic resonance in medicine*, 42(3):577–584, 1999.

[Cunningham *et al.*, 2007] C. H. Cunningham, Albert P. Chen, M. J. Albers, John Kurhanewicz, Yi-Fen Yen, Ralph E. Hurd, John M. Pauly, S. J. Nelson, and Daniel B. Vigneron. Double spin-echo sequence for rapid spectroscopic imaging of hyperpolarized ^{13}C. *J Magn Reson*, 187(2):357–362, 2007.

[Cunningham *et al.*, 2008] Charles H Cunningham, Albert P Chen, Michael Lustig, Brian A Hargreaves, Janine Lupo, Duan Xu, John Kurhanewicz, Ralph E Hurd, John M Pauly, Sarah J Nelson, and Daniel B Vigneron. Pulse sequence for dynamic volumetric imaging of hyperpolarized metabolic products. *J Magn Reson*, 193(1):139–46, Jul 2008.

[Daye and Wellen, 2012] Dania Daye and Kathryn E Wellen. Metabolic reprogramming in cancer: unraveling the role of glutamine in tumorigenesis. In *Seminars in cell & developmental biology*, volume 23, pages 362–369. Elsevier, 2012.

[Deimling and Heid, 1994] M Deimling and O Heid. Magnetization prepared true fisp imaging. In *Proceedings of the 2nd Annual Meeting of ISMRM, San Francisco*, page 495, 1994.

[Deppe and Wild, 2012] Martin H Deppe and Jim M Wild. Variable flip angle schedules in bssfp imaging of hyperpolarized noble gases. *Magnetic Resonance in Medicine*, 67(6):1656–1664, 2012.

[Deshpande *et al.*, 2003] Vibhas S Deshpande, Yiu-Cho Chung, Qiang Zhang, Steven M Shea, and Debiao Li. Reduction of transient signal oscillations in true-fisp using a linear flip angle series magnetization preparation. *Magnetic resonance in medicine*, 49(1):151–157, 2003.

[Freeman and Hill, 1971] Ray Freeman and HDW Hill. Phase and intensity anomalies in fourier transform nmr. *Journal of Magnetic Resonance (1969)*, 4(3):366–383, 1971.

[Gallagher *et al.*, 2008] Ferdia A Gallagher, Mikko I Kettunen, Sam E Day, Mathilde Lerche, and Kevin M Brindle. 13c mr spectroscopy measurements of glutaminase activity in human hepatocellular carcinoma cells using hyperpolarized 13c-labeled glutamine. *Magnetic Resonance in Medicine*, 60(2):253–257, 2008.

[Ganter, 2004] Carl Ganter. Off-resonance effects in the transient response of ssfp sequences. *Magnetic resonance in medicine*, 52(2):368–375, 2004.

[Golman *et al.*, 2003] Klaes Golman, Jan H. Ardenkjær-Larsen, J. Stefan Petersson, Sven Mansson, and Ib Leunbach. Molecular imaging with endogenous substances. *Proc Natl Acad Sci U S A*, 100(18):10435–10439, 2003.

[Golman *et al.*, 2006] Klaes Golman, René Zandt, and Mikkel Thaning. Real-time metabolic imaging. *Proc Natl Acad Sci U S A*, 103(30):11270–11275, 2006.

[Gordon *et al.*, 2012] Jeremy W Gordon, Sean B Fain, and Ian J Rowland. Effect of lanthanide ions on dynamic nuclear polarization enhancement and liquid-state t1 relaxation. *Magnetic resonance in medicine*, 68(6):1949–1954, 2012.

[Grant *et al.*, 2008] Michael Grant, Stephen Boyd, and Yinyu Ye. Cvx: Matlab software for disciplined convex programming, 2008.

[Hargreaves *et al.*, 2001] Brian A Hargreaves, Shreyas S Vasanawala, John M Pauly, and Dwight G Nishimura. Characterization and reduction of the transient response in steady-state mr imaging. *Magnetic resonance in medicine*, 46(1):149–158, 2001.

[Hargreaves *et al.*, 2003] Brian A Hargreaves, Shreyas S Vasanawala, Krishna S Nayak, Bob S Hu, and Dwight G Nishimura. Fat-suppressed steady-state free precession imaging using phase detection. *Magnetic resonance in medicine*, 50(1):210–213, 2003.

[Janich *et al.*, 2011] Martin A Janich, Rolf F Schulte, Markus Schwaiger, and Steffen J Glaser. Robust slice-selective broadband refocusing pulses. *Journal of Magnetic Resonance*, 213(1):126–135, 2011.

[Jaynes, 1955] ET Jaynes. Matrix treatment of nuclear induction. *Physical Review*, 98(4):1099, 1955.

[Jenkinson *et al.*, 2012] Mark Jenkinson, Christian F Beckmann, Timothy EJ Behrens, Mark W Woolrich, and Stephen M Smith. Fsl. *Neuroimage*, 62(2):782–790, 2012.

[Johansson *et al.*, 2004] E. Johansson, S. Mansson, R. Wirestam, J. Svensson, J.S. Petersson, K. Golman, and F. Stahlberg. Cerebral perfusion assessment by bolus tracking using hyperpolarized ^{13}C. *Magn Reson Med*, 51(3):464–472, 2004.

[Jou *et al.*, 2015] Tiffany Jou, Steve Patterson, John M Pauly, and Chris V Bowen. Fat-suppressed alternating-ssfp for whole-brain fmri using breath-hold and visual stimulus paradigms. *Magnetic resonance in medicine*, 2015.

[Kerr *et al.*, 2008] A. B. Kerr, P. E. Larson, M. Lustig, C. H. Cunningham, A. P. Chen, D. B. Vigneron, and J. M. Pauly. Multiband spectral-spatial design for high-field and hyperpolarized C-13 applications. In *Proceedings of the 16th Annual Meeting of ISMRM*, page 226, Toronto, 2008.

[Keshari and Wilson, 2014] Kayvan R Keshari and David M Wilson. Chemistry and biochemistry of 13 c hyperpolarized magnetic resonance using dynamic nuclear polarization. *Chemical Society Reviews*, 43(5):1627–1659, 2014.

[Koelsch *et al.*, 2014] Bertram L Koelsch, Galen D Reed, Kayvan R Keshari, Myriam M Chaumeil, Robert Bok, Sabrina M Ronen, Daniel B Vigneron, John Kurhanewicz, and Peder EZ Larson. Rapid in vivo apparent diffusion coefficient mapping of hyperpolarized 13c metabolites. *Magnetic Resonance in Medicine*, 2014.

[Komar *et al.*, 2009] Gaber Komar, Saila Kauhanen, Kaisa Liukko, Marko Seppänen, Sami Kajander, Jari Ovaska, Pirjo Nuutila, and Heikki Minn. Decreased blood flow with increased metabolic activity: a novel sign of pancreatic tumor aggressiveness. *Clinical Cancer Research*, 15(17):5511–5517, 2009.

[Kurhanewicz *et al.*, 2011] John Kurhanewicz, Daniel B Vigneron, Kevin Brindle, Eduard Y Chekmenev, Arnaud Comment, Charles H Cunningham, Ralph J Deberardinis, Gary G Green, Martin O Leach, Sunder S Rajan, Rahim R Rizi, Brian D Ross, Warren S Warren, and Craig R Malloy. Analysis of cancer metabolism by imaging hyperpolarized nuclei: prospects for translation to clinical research. *Neoplasia*, 13(2):81–97, Feb 2011.

[Larson *et al.*, 2008] Peder E Z Larson, Adam B Kerr, Albert P Chen, Michael S Lustig, Matthew L Zierhut, Simon Hu, Charles H Cunningham, John M Pauly, John Kurhanewicz, and Daniel B Vigneron. Multiband excitation pulses for hyperpolarized ^{13}C dynamic chemical-shift imaging. *J Magn Reson*, 194(1):121–7, Sep 2008.

[Larson *et al.*, 2011] Peder E Z Larson, Simon Hu, Michael Lustig, Adam B Kerr, Sarah J Nelson, John Kurhanewicz, John M Pauly, and Daniel B Vigneron. Fast dynamic 3D

MR spectroscopic imaging with compressed sensing and multiband excitation pulses for hyperpolarized ^{13}C studies. *Magn Reson Med*, 65(3):610–9, 2011.

[Lau *et al.*, 2010] A. Z. Lau, A. P. Chen, N. R. Ghugre, V. Ramanan, W. W. Lam, K. A. Connelly, G. A. Wright, and C. H. Cunningham. Rapid multislice imaging of hyperpolarized ^{13}C pyruvate and bicarbonate in the heart. *Magn Reson Med*, 64(5):1323–31, 2010.

[Le Roux *et al.*, 1998] Patrick Le Roux, Raymond J Gilles, Graeme C McKinnon, and Pierre G Carlier. Optimized outer volume suppression for single-shot fast spin-echo cardiac imaging. *Journal of Magnetic Resonance Imaging*, 8(5):1022–1032, 1998.

[Le Roux, 2003] Patrick Le Roux. Simplified model and stabilization of ssfp sequences. *Journal of Magnetic Resonance*, 163(1):23–37, 2003.

[Lee, 2007] Kuan J Lee. General parameter relations for the shinnar-le roux pulse design algorithm. *Journal of Magnetic Resonance*, 186(2):252–258, 2007.

[Leupold *et al.*, 2006] J Leupold, J Hennig, and Klaus Scheffler. Alternating repetition time balanced steady state free precession. *Magnetic resonance in medicine*, 55(3):557–565, 2006.

[Leupold *et al.*, 2009] Jochen Leupold, Sven Månsson, J Stefan Petersson, Jürgen Hennig, and Oliver Wieben. Fast multiecho balanced ssfp metabolite mapping of 1h and hyperpolarized 13c compounds. *Magnetic Resonance Materials in Physics, Biology and Medicine*, 22(4):251–256, 2009.

[Lustig *et al.*, 2006] Michael Lustig, Charles H Cunningham, and JM Pauly. A montecarlo algorithm for designing ultrahigh timebandwidth, minimum peak— b1—, selective saturation and inversion rfpulses. *Proceedings of the ENC, Pacific Grove, California, USA*, 2006.

[Lyerla Jr *et al.*, 1971] James R Lyerla Jr, David M Grant, and Richard D Bertrand. Field-dependent contributions to carbon-13 nuclear relaxation. *The Journal of Physical Chemistry*, 75(26):3967–3971, 1971.

[Mankoff *et al.*, 2002] David A Mankoff, Lisa K Dunnwald, Julie R Gralow, Georgiana K Ellis, Aaron Charlop, Thomas J Lawton, Erin K Schubert, Jeffrey Tseng, and Robert B Livingston. Blood flow and metabolism in locally advanced breast cancer: relationship to response to therapy. *Journal of Nuclear Medicine*, 43(4):500–509, 2002.

[Månsson *et al.*, 2012] Sven Månsson, J Stefan Petersson, and Klaus Scheffler. Fast metabolite mapping in the pig heart after injection of hyperpolarized 13c-pyruvate with low-flip

angle balanced steady-state free precession imaging. *Magnetic resonance in medicine*, 68(6):1894–1899, 2012.

[Mayer *et al.*, 2009] Dirk Mayer, Yi-Fen Yen, James Tropp, Adolf Pfefferbaum, Ralph E Hurd, and Daniel M Spielman. Application of subsecond spiral chemical shift imaging to real-time multislice metabolic imaging of the rat in vivo after injection of hyperpolarized 13c1-pyruvate. *Magnetic resonance in medicine*, 62(3):557–564, 2009.

[Miller *et al.*, 2015] Jack J Miller, Angus Z Lau, Irvin Teh, Jürgen E Schneider, Paul Kinchesh, Sean Smart, Vicky Ball, Nicola R Sibson, and Damian J Tyler. Robust and high resolution hyperpolarized metabolic imaging of the rat heart at 7 t with 3d spectral-spatial epi. *Magnetic resonance in medicine*, 2015.

[Milshteyn *et al.*, 2015] Eugene Milshteyn, Cornelius von Morze, Galen Reed, Hong Shang, Peter Shin, Zihan Zhu, John Kurhanewicz, Robert Bok, and Daniel B Vigneron. Development of high resolution 3d hyperpolarized 13c imaging techniques. In *Proc 23rd Annual Meeting ISMRM, Toronto*, page 4599, 2015.

[Morze *et al.*, 2014] Cornelius Morze, Robert A Bok, Galen D Reed, Jan Henrik Ardenkjaer-Larsen, John Kurhanewicz, and Daniel B Vigneron. Simultaneous multiagent hyperpolarized 13c perfusion imaging. *Magnetic resonance in medicine*, 72(6):1599–1609, 2014.

[Nelson *et al.*, 2013] Sarah J. Nelson, John Kurhanewicz, Daniel B. Vigneron, Peder E. Z. Larson, Andrea L. Harzstark, Marcus Ferrone, Mark van Criekinge, Jose W. Chang, Robert Bok, Ilwoo Park, Galen Reed, Lucas Carvajal, Eric J. Small, Pamela Munster, Vivian K. Weinberg, Jan Henrik Ardenkjaer-Larsen, Albert P. Chen, Ralph E. Hurd, Liv-Ingrid Odegardstuen, Fraser J. Robb, James Tropp, and Jonathan A. Murray. Metabolic imaging of patients with prostate cancer using hyperpolarized [1-^{13}C]pyruvate. *Sci Transl Med*, 5(198):198ra108, 2013.

[Nocedal and Wright, 2006] Jorge Nocedal and Stephen Wright. *Numerical optimization*. Springer Science & Business Media, 2006.

[Oppelt *et al.*, 1986] A Oppelt, R Graumann, H Barfuss, H Fischer, W Hartl, W Schajor, et al. Fispa new fast mri sequence. *Electromedica*, 54(1):15–18, 1986.

[Overall *et al.*, 2003] William R Overall, Dwight G Nishimura, and Bob S Hu. Steady-state sequence synthesis and its application to efficient fat-suppressed imaging. *Magnetic resonance in medicine*, 50(3):550–559, 2003.

[Paul and Hennig, 2004] D Paul and J Hennig. Comparison of different flip angle variation functions for improved signal behavior in ssfp sequences. In *Proceedings of the 12th Annual Meeting of ISMRM, Kyoto, Japan*, page 2663, 2004.

[Paul and Zaitsev, 2009] Dominik Paul and Maxim Zaitsev. Improved snr in linear reordered 2d bssfp imaging using variable flip angles. *Magnetic resonance imaging*, 27(7):933–941, 2009.

[Pauly *et al.*, 1991] J. Pauly, P. Le Roux, D. Nishimura, and A. Macovski. Parameter relations for the Shinnar-Le Roux selective excitation pulse design algorithm. *IEEE T Med Imaging*, 10(1):53–65, 1991.

[Pickup and Ding, 1995] Stephen Pickup and Xiaoning Ding. Pulses with fixed magnitude and variable phase response profiles. *Magnetic resonance in medicine*, 33(5):648–655, 1995.

[Raddi and Klose, 1998] A Raddi and U Klose. A generalized estimate of the slrbpolynomial ripples for rf pulse generation. *Journal of Magnetic Resonance*, 132(2):260–265, 1998.

[Reed *et al.*, 2014] Galen D Reed, Cornelius von Morze, Robert Bok, Bertram L Koelsch, Mark Van Criekinge, Kenneth J Smith, Hong Shang, Peder EZ Larson, John Kurhanewicz, and Daniel B Vigneron. High resolution c mri with hyperpolarized urea: In vivo mapping and n labeling effects. *Medical Imaging, IEEE Transactions on*, 33(2):362–371, 2014.

[Reed *et al.*, 2015] Galen D Reed, Cornelius von Morze, Alan S Verkman, Bertram L Koelsch, Myriam M Chaumeil, Michael Lustig, Sabrina M Ronen, Jeff M Sands, Peder EZ Larson, Zhen J Wang, et al. Imaging renal urea handling in rats at millimeter resolution using hyperpolarized magnetic resonance relaxometry. *arXiv preprint arXiv:1511.00200*, 2015.

[Reeder *et al.*, 2007] Scott B. Reeder, Jean H. Brittain, Thomas M. Grist, and Yi-Fen Yen. Least-squares chemical shift separation for ^{13}C metabolic imaging. *J Magn Reson Imaging*, 26(4):1145–1152, 2007.

[Ribot *et al.*, 2015] Emeline J Ribot, Didier Wecker, Aurélien J Trotier, Benjamin Dallaudière, William Lefrançois, Eric Thiaudière, Jean-Michel Franconi, and Sylvain Miraux. Water selective imaging and bssfp banding artifact correction in humans and small animals at 3t and 7t, respectively. *PloS one*, 10(10):e0139249, 2015.

[Scheffler and Hennig, 2003] Klaus Scheffler and Jürgen Hennig. Is truefisp a gradient-echo or a spin-echo sequence? *Magnetic resonance in medicine*, 49(2):395–397, 2003.

[Scheffler and Lehnhardt, 2003] Klaus Scheffler and Stefan Lehnhardt. Principles and applications of balanced ssfp techniques. *European radiology*, 13(11):2409–2418, 2003.

[Scheffler *et al.*, 2001] Klaus Scheffler, Oliver Heid, and Jürgen Hennig. Magnetization preparation during the steady state: Fat-saturated 3d truefisp. *Magnetic resonance in medicine*, 45(6):1075–1080, 2001.

[Scheffler, 2003] Klaus Scheffler. On the transient phase of balanced ssfp sequences. *Magnetic resonance in medicine*, 49(4):781–783, 2003.

[Schricker *et al.*, 2001] Amir A. Schricker, John M. Pauly, John Kurhanewicz, Mark G. Swanson, and Daniel B. Vigneron. Dualband spectral-spatial RF pulses for prostate MR spectroscopic imaging. *Magn Reson Med*, 46(6):1079–1087, 2001.

[Schulte *et al.*, 2004] Rolf F Schulte, Jeffrey Tsao, Peter Boesiger, and Klaas P Pruessmann. Equi-ripple design of quadratic-phase rf pulses. *Journal of Magnetic Resonance*, 166(1):111–122, 2004.

[Schulte *et al.*, 2013] Rolf F. Schulte, Jonathan I. Sperl, Eliane Weidl, Marion I. Menzel, Martin A. Janich, Oleksandr Khegai, Markus Durst, Jan Henrik Ardenkjaer-Larsen, Steffen J. Glaser, Axel Haase, Markus Schwaiger, and Florian Wiesinger. Saturation-recovery metabolic-exchange rate imaging with hyperpolarized [1-^{13}C] pyruvate using spectral-spatial excitation. *Magn Reson Med*, 69(5):1209–1216, 2013.

[Shang *et al.*, 2015] Hong Shang, Timothy Skloss, Cornelius von Morze, Lucas Carvajal, Mark Van Criekinge, Eugene Milshteyn, Peder EZ Larson, Ralph E Hurd, and Daniel B Vigneron. Handheld electromagnet carrier for transfer of hyperpolarized carbon-13 samples. *Magnetic Resonance in Medicine*, 2015.

[Shang *et al.*, 2016] Hong Shang, Peder EZ Larson, Adam Kerr, Galen Reed, Subramaniam Sukumar, Adam Elkhaled, Jeremy W Gordon, Michael A Ohliger, John M Pauly, Michael Lustig, et al. Multiband rf pulses with improved performance via convex optimization. *Journal of Magnetic Resonance*, 262:81–90, 2016.

[Sitton *et al.*, 2003] Gary A Sitton, C Sidney Burrus, James W Fox, and Sven Treitel. Factoring very-high-degree polynomials. *Signal Processing Magazine, IEEE*, 20(6):27–42, 2003.

[Smith *et al.*, 2010] Travis Smith, Zungho Zun, Eric C Wong, and Krishna S Nayak. Design and use of variable flip angle schedules in transient balanced ssfp subtractive imaging. *Magnetic Resonance in Medicine*, 63(2):537–542, 2010.

[Stikov *et al.*, 2007] Nikola Stikov, A Mutapcic, and JM Pauly. Optimized design of single-sided quadratic phase outer volume suppression pulses for magnetic resonance imaging. In *11th Mediterranean Conference on Medical and Biomedical Engineering and Computing 2007*, pages 423–425. Springer, 2007.

[Svensson *et al.*, 2003] Jonas Svensson, Sven Månsson, Edvin Johansson, J Stefan Petersson, and Lars E Olsson. Hyperpolarized 13c mr angiography using truefisp. *Magnetic resonance in medicine*, 50(2):256–262, 2003.

[Tran *et al.*, 2000] Tuan-Khanh C Tran, Daniel B Vigneron, Napapon Sailasuta, James Tropp, Patrick Le Roux, John Kurhanewicz, Sarah Nelson, and Ralph Hurd. Very selective suppression pulses for clinical mrsi studies of brain and prostate cancer. *Magnetic resonance in medicine*, 43(1):23–33, 2000.

[Varma *et al.*, 2015] Gopal Varma, Xiaoen Wang, Elena Vinogradov, Rupal S Bhatt, Vikas P Sukhatme, Pankaj Seth, Robert E Lenkinski, David C Alsop, and Aaron K Grant. Selective spectroscopic imaging of hyperpolarized pyruvate and its metabolites using a single-echo variable phase advance method in balanced ssfp. *Magnetic resonance in medicine*, 2015.

[Vasanawala *et al.*, 1999] Shreyas S Vasanawala, John M Pauly, and Dwight G Nishimura. Fluctuating equilibrium mri. *Magnetic resonance in medicine*, 42(5):876–883, 1999.

[Vasanawala *et al.*, 2000] Shreyas S Vasanawala, John M Pauly, and Dwight G Nishimura. Linear combination steady-state free precession mri. *Magnetic resonance in medicine*, 43(1):82–90, 2000.

[von Morze *et al.*, 2011a] Cornelius von Morze, Peder E Z Larson, Simon Hu, Kayvan Keshari, David M Wilson, Jan Henrik Ardenkjær-Larsen, Andrei Goga, Robert Bok, John Kurhanewicz, and Daniel B Vigneron. Imaging of blood flow using hyperpolarized [^{13}C]urea in preclinical cancer models. *J Magn Reson Imaging*, 33(3):692–7, Mar 2011.

[von Morze *et al.*, 2011b] Cornelius von Morze, Galen Reed, Peter Shin, Peder EZ Larson, Simon Hu, Robert Bok, and Daniel B Vigneron. Multi-band frequency encoding method for metabolic imaging with hyperpolarized [1-13 c] pyruvate. *Journal of magnetic resonance*, 211(2):109–113, 2011.

[von Morze *et al.*, 2012a] Cornelius von Morze, Robert A. Bok, Jeff M. Sands, John Kurhanewicz, and Daniel B. Vigneron. Monitoring urea transport in rat kidney in vivo using hyperpolarized ^{13}C magnetic resonance imaging. *Am J Physiol-Renal*, 302(12):F1658–F1662, 2012.

[von Morze *et al.*, 2012b] Cornelius von Morze, Peder EZ Larson, Simon Hu, Hikari AI Yoshihara, Robert A Bok, Andrei Goga, Jan Henrik Ardenkjaer-Larsen, and Daniel B Vigneron. Investigating tumor perfusion and metabolism using multiple hyperpolarized 13 c compounds: Hp001, pyruvate and urea. *Magnetic resonance imaging*, 30(3):305–311, 2012.

[von Morze *et al.*, 2013] Cornelius von Morze, Subramaniam Sukumar, Galen D Reed, Peder EZ Larson, Robert A Bok, John Kurhanewicz, and Daniel B Vigneron. Frequency-specific ssfp for hyperpolarized 13 c metabolic imaging at 14.1 t. *Magnetic resonance imaging*, 31(2):163–170, 2013.

[von Morze *et al.*, 2014] Cornelius von Morze, Peder EZ Larson, Hong Shang, and Daniel B Vigneron. Suppression of unwanted resonances in hyperpolarized mr studies with neat [1-13c]lactic acid. In *Proc 22nd Annual Meeting ISMRM, Milan*, page 2792, 2014.

[von Morze *et al.*, 2016] Cornelius von Morze, Gene-Yuan Chang, Peder EZ Larson, Hong Shang, Prasanna KR Allu, Robert A Bok, Jason C Crane, Marram P Olson, Chou T Tan, Irene Marco-Rius, et al. Detection of localized changes in the metabolism of hyperpolarized gluconeogenic precursors 13c-lactate and 13c-pyruvate in kidney and liver. *Magnetic resonance in medicine*, 2016.

[Wilson *et al.*, 2010] David M Wilson, Kayvan R Keshari, Peder EZ Larson, Albert P Chen, Simon Hu, Mark Van Criekinge, Robert Bok, Sarah J Nelson, Jeffrey M Macdonald, Daniel B Vigneron, et al. Multi-compound polarization by dnp allows simultaneous assessment of multiple enzymatic activities in vivo. *Journal of magnetic resonance*, 205(1):141–147, 2010.

[Worters and Hargreaves, 2010] Pauline W Worters and Brian A Hargreaves. Balanced ssfp transient imaging using variable flip angles for a predefined signal profile. *Magnetic Resonance in Medicine*, 64(5):1404–1412, 2010.

[Wu *et al.*, 1996] Shao-Po Wu, Stephen Boyd, and Lieven Vandenberghe. Fir filter design via semidefinite programming and spectral factorization. In *Decision and Control, 1996., Proceedings of the 35th IEEE Conference on*, volume 1, pages 271–276. IEEE, 1996.

[Xing *et al.*, 2013] Yan Xing, Galen D Reed, John M Pauly, Adam B Kerr, and Peder EZ Larson. Optimal variable flip angle schemes for dynamic acquisition of exchanging hyperpolarized substrates. *Journal of Magnetic Resonance*, 234:75–81, 2013.

[Yen *et al.*, 2010] Yi-Fen Yen, Patrick Le Roux, Dirk Mayer, Randy King, Daniel Spielman, James Tropp, Kim Butts Pauly, Adolf Pfefferbaum, Shreyas Vasanawala, and Ralph Hurd. T2 relaxation times of 13c metabolites in a rat hepatocellular carcinoma model measured in vivo using 13c-mrs of hyperpolarized [1-13c] pyruvate. *NMR in biomedicine*, 23(4):414–423, 2010.

[Yuan *et al.*, 2011] Jing Yuan, Bruno Madore, and Lawrence P Panych. Fat–water selective excitation in balanced steady-state free precession using short spatial–spectral rf pulses. *Journal of Magnetic Resonance*, 208(2):219–224, 2011.

[Zhao *et al.*, 1996] L. Zhao, R.V. Mulkern, C.H. Tseng, D. Williamson, S. Patz, R. Kraft, R.L. Walsworth, F.A. Jolesz, and M.S. Albert. Gradient-echo imaging considerations for hyperpolarized ^{129}Xe MR. *J Magn Reson B*, 113(2):179–183, 1996.

[Zun and Nayak, 2006] Z Zun and KS Nayak. Graphical derivation of the steady-state magnetization in balanced ssfp mri. In *Proc 14th Annual Meeting ISMRM, Seattle*, page 2410, 2006.

Publishing Agreement

It is the policy of the University to encourage the distribution of all theses, dissertations, and manuscripts. Copies of all UCSF theses, dissertations, and manuscripts will be routed to the library via the Graduate Division. The library will make all theses, dissertations, and manuscripts accessible to the public and will preserve these to the best of their abilities, in perpetuity.

Please sign the following statement:

I hereby grant permission to the Graduate Division of the University of California, San Francisco to release copies of my thesis, dissertation, or manuscript to the Campus Library to provide access and preservation, in whole or in part, in perpetuity.

Hong Shang
Author Signature

06/08/2016
Date